JSPS-CAS Core University Program Seminar
Proceedings of Japan-China Joint Seminar on
Laser Plasma and High Energy Density Physics
October 14-16, 2010, Shanghai, China

Edited by
H. Sakagami and Z. M. Sheng

Abstract

The JSPS-CAS Core University program seminar on "Laser Plasma and High Energy Density Physics" was held in Xuhui Campus of Shanghai Jiao Tong University on October 14-16, 2010. 10 Japanese invited talks were presented while the total of 18 invited talks were given. This seminar was combined with 2nd China National Symposium on High Energy Density Physics, and another 27 oral talks and 26 posters were presented for this symposium. Totally over 90 participants including many young graduate students also attended the seminar.

This workshop planned as a final in this ten years' collaboration between China and Japan. The workshop was originally planned to promote communications with young Chinese scientists and graduate students and Japanese scientists as well as Chinese scientists. Many cutting edge physics were presented from both countries and the collaboration through the JSPS-CAS Core University program was summarized by Prof. K. A. Tanaka and Prof. S. Zhu.

Keywords:
laser plasma, high energy density, laser astrophysics, inertial fusion energy, fast ignition, laser acceleration, laser driven X-ray source, warm dense matter, diagnostic

Preface

This seminar planned on as the summary seminar at the end of CUP final year 2010. Originally this seminar was tried to be held in Japan, but was recommended strongly at the CUP key person meeting at the spring in Atami, 2010 that the seminar should be held in China in order to promote the HEDS to the young graduate students and scientists in China.

This high density plasma 15 A and 15 B categories in the CUP program have been very much in success in this ten years. Key person in 15A (high density plasmas) has been Kazuo A Tanaka. Key persons in15 B have been Prof. Kunioki Mima and Hideaki Takabe. The promotion of high energy density science (HEDP) through this CUP program has been notable. Scientific papers have been published in such as in Physical Review Letters, Physical Review E, and Physics of Plasmas as results of CUP collaborations. Invited talks were also given at various outstanding conferences such as DPP-APS (Div. Plasma Physics, American Physical Society) and JPFR (Japan Society of Plasma Science and Fusion Research). Among the many subjects we have covered the following subjects for collaboration: relativistic laser plasma interaction, fast ignition basic physics, super-nova explosion physics, nano structure formation with ultra-intense laser beam, astrophysics and extreme science such as positron-electron pair production, which were also discussed at the seminar in Shanghai Jiao Tong University. The participated universities and institutes from Japan include Osaka University, Kyoto University, Tohoku University, University of Electro Communications, National Institute for Fusion Science, Institute for Laser Technology and Advanced Photon Research Center, JAEA. The participants in China come from Shanghai Jiao Tong University, Shanghai Institute of Optics and Fine Mechanics, Shanghai Institute of Laser Plasma, University of Science and Technology of China, National University of Defense Technology, East China Normal University, China University of Mining and Technology, Laser Fusion Research Center/CAEP, Peking University, Institute of Applied Physics and Computational Mathematics, Institute of Physics/CAS in Beijing and more.

We hope that the collaboration grown under this CUP program will continue and more frequent exchange of scholars and students is encouraged in the future.

Best Regards,
Kazuo A. Tanaka and Shaoping Zhu


第二届全国高能量密度物理会议暨中日CUP激光等离子体物理研讨会
上海交通大学 2010.10.13
Shanghai Advanced Institute of Finance
上海高级

Contents

CUP Summary

Hideaki Takabe
ILE, Osaka University
takabe(at)ile.osaka-u.ac.jp

It is my honor to gave a brief talk on the summary of the ten-year project of Japan-China collaboration Program supported by Japan side JSPS (Japan Society for Promotion of Science) and China side NNSF (National Natural Science Foundation).

One of the great benefits though the program is the construction of human relation between the two countries and the fact that we have obtained the trustworthy friends in each countries is especially the most important products.

One of the pioneers of Chinese large scale laser program, Prof. Deng Xing-ming, told in front of Japanese in our institute almost 30 years ago that “On the long way to go, we appreciate the power of a horse. Through a long time to go, we understand the mind of the horse”.

Official collaboration between Japan and China has lasted for more than 1,500 years. Without a relatively short time, we have kept a good relation. I hope Japan and China will encourage each other and show a leadership so that they will construct the new era of East-Asia Union, and Asia-Union, and so on in the near future. It is a time of globalization. Good example is EU. EU is going to try to construct the grate EU with a lot of investment with the money from rich west countries to the poor-infrastructure east Europe countries.

The enrichment of the science and technology by CUP program should be distributed the other Asian counties in the coming years.

Experimental progress on laser-driven fusion and radiation-related studies in RCLF

Jiamin Yang[*1], Li Shanwei[1], Huang Tianxuan[1], Miao Wenyong[1], Zhang Jiyan[1], Yi Rongqing[1], Cheng Jiabin[1], Liu Shenye[1], Jiang Shaoen[1], Jin Fen[1], Zhang Lin[1],Yongkun Ding [1]
Jinhong Li [2], Pei Wenbing[2], Gu Peijun[2], Gao Yaomin[2], Xu Yan[2]

[1] *Research Center of Laser Fusion, Mianyang 621900, China*
[2] *Beijing Institute of Applied Physics and Computational Mathematics, Beijing 100088, China*

[*] E-mail: yjm70018@my-public.sc.cninfo.net

Abstract: Laser-driven fusion is one of possible approaches to generate clean energy in future and a lot of world-wide efforts have been devoted to develop inertial confinement fusion (ICF) in recent years [1-3]. In this report the laser facilities used for ICF studies in China are briefed at first. Then the experimental progresses are present on laser-hohlraum coupling, radiation-driven RT instability and implosion in Research Center of Laser Fusion (RCLF) [4]. As the high power laser can create matters in extreme states and generate strong radiation as driving or backlight sources, the radiation-related experiments have also been carried out in RCLF [5-11]. The experimental progresses on opacity, radiation transport and x-ray spectra from laser-produced plasmas are also reviewed in the report.

Key words: Laser-driven fusion; radiation-related experiment; experimental progress.

[1] Lindl,J. D., ***Phys. Plasmas*** 2, 3933(1995)
[2] Lindl, J.D., Amendt P., Berger, R.L. et al, ***Phys. Plasmas*** 11(2), 339(2004)
[3] Azechi H. And FIREX Project, ***JoP: CS*** 112,012002 (2008)
[4] Jiang S.E., Ding Y.K., Miao W.Y., et al, ***Science in China G*** 39(11), 1571(2009) (in Chinese)
[5] Xu Y., Zhang J.Y., Yang J.M., et al, ***Phys. Plasmas*** 14, 052701 (2007);
[6] Zhang J.Y., Yang J.M., Xu Y., et al, ***ACTA PHYSICA SINICA*** 57(2), 985(2008) (in Chinese)
[7] Zhang J.Y., Yang J.M., Xu Y., et al., ***Phys. Rev E*** 79,016401(2008)
[8] Zhao Y., Yang J.M., Zhang J.Y. et al., ***Rev. Sci. Instrum.*** 80, 043505(2009)
[9] Yang J.M., Zhang J. Y., Xu Y. Et al, ***JoP: CS*** 163, 012098 (2009)
[10] Yang J.M., Hu Z.M., Zhang J.Y. et al, ***Phys. Plasmas*** 15 , 112704(2008)
[11] Pu Y.D., Jin F.T., Yang J.M., et al, ***ACTA PHYSICA SINCA***, to be published(2010) (in Chinese)

*Full paper was not submitted by authors.

Review of Relativistic Energetic Electrons and Laser Light Relevant to Fast Ignition

Kazuo A. Tanaka

Graduate School of Engineering, Osaka Univeristy, AR_304, Yamada-oka 2-1, Suita, Osaka 565-0871 Japan
E-mail: katanaka@eei.eng.osaka-u.ac.jp

Research in inertial fusion energy approaches important era as the ignition is about to be achieved at the National Ignition Facility at Lawrence Livermore National Laboratory, U.S.A. While this ignition will be achieved with the central ignition scheme in x-ray hohlraum cavity, there have been intensive studies on fast ignition which should enable the ignition about 10 times smaller laser energy. We have studied this fast ignition scheme for more than a decade and have focused on "Super-penetration" laser focusing in order to carry the fast heating laser pulse to the vicinity of the highly compressed core. It is also of critical importance to learn and to understand the characteristic of Energetic electrons created with an ultra-intense laser which will be used to ignite the core.

I. INTRODUCTION

Ultraintense laser propagation in plasmas has been explored extensively[1-11]. When the laser power exceeds the critical value P_{cr}=17n_c /n_e GW, where n_e and n_c are the plasma and critical densities, respectively, it can undergo relativistic self-focusing (RSF)[1]. The laser pulse can propagate in the overdense plasma because of relativistic induced transparency (RIT)[2] and laser hole boring (LHB)[3].. RIT allows the laser to propagate in a plasma with density less than n_c, where $\gamma = (1+[I\lambda^2/(2.74\text{x}10^{18})])^{1/2}$ is the Lorenz factor, I is the laser intensity in W/cm−2, and λ is the laser wavelength in microns. RIT with RSF can induce self-guiding of the ultraintense laser in high-density plasmas. We [4,5] observed a propagation mode (the superpenetration mode) involving RSF, RIT, and LHB. When a subpicosecond 100 TW laser is injected into a preformed plasma, strong x-ray emission around the solid-target surface was observed, indicating that the laser pulse can propagate 100 μm in the inhomogeneous overdense plasma with densities up to that of solid.

It is also essential to characterize the Energetic electron energy distribution as a function of irradiance on target. If the average Energetic electron is too high, then their range is too large in the compressed plasma and more energy is needed to heat the compressed Energetic spark region[6]. If the energy of the electrons is too low, then the electrons may not reach the spark region in the compressed matter, as they prone to large angle scattering when they have to traverse dense gold in cone-guided geometries.

II. SUPER-PENETRATION EXPERIMENTAL SETUP

The experiments on ultra-intense laser self-focusing "Super-Penetration" were conducted with the 100 TW "GEKKO PW" [7] short pulse laser systems coupled by a long pulse laser. The GEKKO PW can deliver 100–250 J with 0.6 ps duration at 1 μm wavelength. The focus spot size was about 70 μm, with intensity 0.65–1.1x10^{19} W/cm^2. The preformed plasmas were created with thin deuterated carbon (CD) foils with Al coating on the front surface by focusing a beam of the long pulse 0.53 μm GEKKO XII laser. The plasma density profiles were controlled by changing the time delay between the GEKKO PW and GEKKO XII lasers. Typically, the peak density of the preformed plasma is around or higher than 10 n_c.

II.A. Plasma channel formation

In FI, the ultraintense laser energy must be transmitted into the core plasma through the thick coronal plasma which contains large underdense and overdense regions. For example, a CD shell target of 500 μm diameter and 8 μm shell thickness imploded by a 2 kJ 0.53 μm 1 ns laser has a length over 500 μm at a density 0.1–1 n_c, and 200 μm at 1 n_c to 10 n_c. In the context of FI, one important question is whether an ultraintense laser with an intensity
10^{19} W/cm^2 can penetrate the thick coronal plasma with entire beam self-focused. In an earlier experiment, We observed strong x-ray emission around the solid-target surface, which might indicate that the intense laser could propagate 100 μm in inhomogeneous overdense plasmas into near solid regions. However, this x-ray emission can also be caused by the local heating of the solid surface by the Energetic electrons generated in the ultraintense laser propagation. These electrons may be generated far from the solid surface and they transport to the surface and heat it, causing x-ray emission. It is desirable for FI to study the details of RSF behaviors in a preformed plasma with a large overdense region. We have studied laser light behaviors in the preformed plasma which has a 80 μm

overdense region and is created on a plane solid CD target. The experiments were carried out with the 100 TW GEKKO PW laser synchronized with the GEKKO XII laser system within a time jitter of less than 10 ps.[8] Preformed plasmas were created by one beam of the 1–1.3 ns long pulse GEKKO XII laser with 1 μm thick CD foils with 0.1 μm Al coating on the front surface. The preformed plasma density is calculated using a one-dimensional (1D) hydrocode code ILESTA 1D.[9] The ILESTA 1D has been benchmarked by x-ray, ultraviolet, and optical laser probe diagnostics[10,11] as well as used to characterize the plasma density profile. The typical plasma density profile at the time of the GEKKO PW laser injection has a length of 500 μm at density of 0.1 to 1 n_c, with an 80 μm overdense region at a peak density of 10 n_c. The uncertainty in the peak plasma density may come from the timing jitter between the GEKKO PW and GEKKO XII lasers. In the experiment, the GEKKO PW laser was optically synchronized to the GEKKO XII and the jitter was less than 10 ps. Within 10 ps, the hydrodynamic motion of the preformed plasma can be neglected. Figure 1 shows the time-integrated x-ray images of the self-emission in front of the target at a view angle of 21° from the GEKKO PW laser axis.

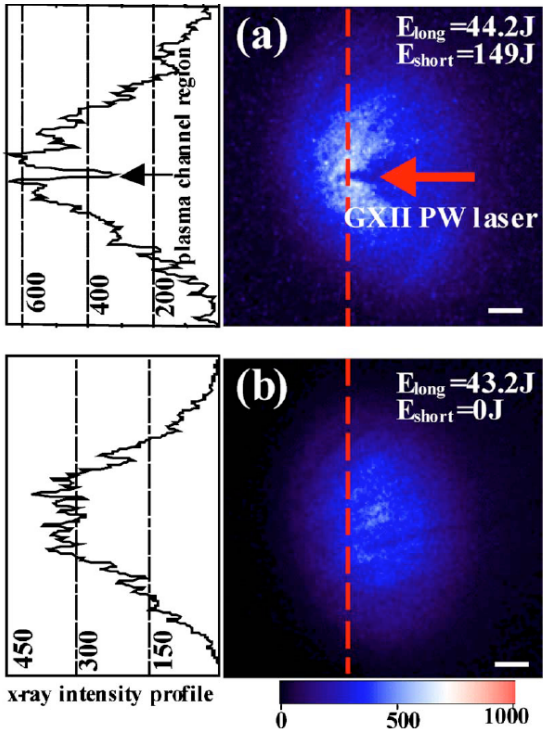

FIG. 1. Time-integrated x-ray pinhole camera images from the preformed plasmas taken (a) with, and (b) without the GEKKO PW laser interactions. The x-ray intensity profiles along the vertical dashed lines in the images are at the left of the images. E_{long} and E_{short} denote the energies of the long pulse GEKKO XII laser and the short pulse GEKKO PW laser. The white scale bars correspond to 100 μm.

Figures 1(a) and 1(b) correspond to the preformed plasma with and without the GEKKO PW laser interactions, respectively. The large 500 μm emission areas shown as an ellipse in Figs. 1(a) and 1(b) are due to the long pulse GEKKO XII laser irradiation on the planar target. There is a distinct difference between Figs. 1(a) and 1(b). In Fig. 1(a), one sees an elongated cone-shaped region at the center of the ellipse. The x-ray emission from this region is considerably weaker than that from the surrounding region. The cone is along the GEKKO PW laser axis, indicating that it is created by the interaction of the GEKKO PW laser with the preformed plasma. The strong ponderomotive force drives the electrons and subsequently also the ions out of the target, leading to depletion of plasma particles and formation of a channel. After passage of the GEKKO PW laser and channel formation, the long pulse GEKKO XII laser still irradiates the entire preformed plasma for several 100 ps. The plasma channel with depleted electrons and ions emits less x-ray than the rest of the plasma. The cone structure in the x-ray image is reproducible in the experiments and can be reconstructed with analytical estimates based on inverse bremsstrahlung x-ray emission and absorption with given plasma parameters. We have simultaneously measured the GEKKO PW laser transmission through the preformed plasma, which was approximately 4% of the laser energy. Therefore the x-ray picture shown in Fig. 1(a) and the laser light transmission measurements indicate that the GEKKO PW laser penetrates through the entire preformed plasma having large underdense and overdense regions along the laser axis. Estimation of the GEKKO PW laser transmission taking into account RIT and LHB (Ref. 3) suggests that the GEKKO PW laser was self-focused down from 70 μm to at least 20 μm to penetrate through the preformed plasma in order to produce the observed light transmission.

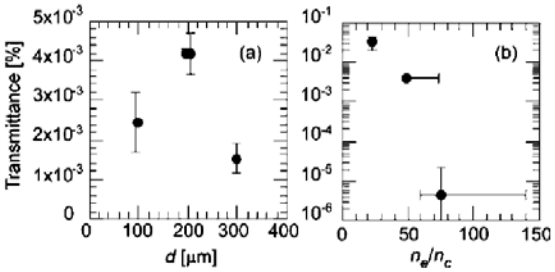

FIG. 2. Ultraintense laser transmission through the overdense plasmas as a function of (a) focal position at peak plasma density of 50 n_c and of (b) the peak density in the preformed.

II.B. Energetic electron generation

In FI, the core plasma is heated by the Energetic electrons generated during the ultraintense laser propagation in the
large scale plasma. The heating efficiency depends on many factors, such as the energy and spatial distribution of the Energetic electrons. A collimated Energetic electron beam with appropriate energy range is essential for the efficient heating. Generation of Energetic electrons was investigated using 100 TW GEKKO PW laser[12].

II. B. Energetic Electron Characteristics

The electron energy spectra were obtained using an electron spectrometer from 21° to the laser axis. The electron angular distribution is obtained with a detector stack consisting of imaging plate [13] placed 34 mm behind the target. Preformed plasmas were created by one beam of the 1–1.3 ns long pulse GEKKO XII laser and 1 μm thick CD foils with 0.1 μm Al coating on the front surface. The plasma density profiles were controlled by the time delay between the short pulse GEKKO PW and the long pulse GEKKO XII lasers. That is, the GEKKO PW laser was injected into the preformed plasmas with either large or small underdense and overdense regions. The plasma scale length was only 3 μm for the small plasma and 136 μm for the large plasma.

The electron energy spectra fitted with a relativistic Maxwellian distribution showed that the electron temperatures were 0.98 and 1.53 MeV for the small and large plasmas at a laser intensity of $4x10^{18}$ W/cm^2. The higher temperature of the Energetic electrons from the large scale preformed plasma indicates that the laser may have undergone self-focusing.

The angular distributions of Energetic electrons from the small and large scale preformed plasmas are rather different when measured with IP plates behind the targets. The Energetic electrons from the small preformed plasma show that the electron emission peaks between the laser axis and the target rear normal, with a beam divergence of 70° (FWHM). This divergence angle is comparable to that from a solid target. For the large scale preformed plasma, the Energetic electron emission peaks along the laser axis and has a beam divergence of 30° (FWHM), which is comparable to the hard x-ray emission from ultraintense laser interaction with an imploded shell plasma. The on-axis electron emission indicates that the laser propagation in the large scale plasma is along its axis. This on-axis behavior of Energetic electrons is also different from that of ultra-intense laser interaction with preplasmas created by a laser prepulse or pedestal, where the Energetic electron beam direction is neither stable nor along the laser axis [14,15] Highly directional and collimated Energetic electron beam in dense plasmas is essential for efficient heating of the compressed tiny core plasma and is of much recent interest.

III. ENERGETIC ELECTRON TEMPERATURE SCALING

III.A. Energetic Electron Temperature Measurement

The experiments were performed using both the VULCAN petawatt (VULCAN PW) [16] and GEKKO XII petawatt (GXII PW) laser systems[17]. The VULCAN PW has a measured intensity contrast ratio of $4x10^{-8}$ and delivered pulses in the range 500 fs–5 ps. Laser pulses with up to 300 J were delivered on target. The wavelength was 1.054 μm. The laser was focused onto target using an f/3 parabola and the spot size was 7 μm full width at half maximum (FWHM). 20% of the laser energy was contained within that focal region. The laser intensity is changed from 1018 to 1021 W cm−2 by varying the energy delivered and the pulse duration. The laser was incident at both normal (0°) and p-polarized 40°. The GXII PW has a measured intensity contrast ratio of $1.5x10^{-8}$. The pulse duration was between from 0.6 to 0.7 ps. Up to 100 J was delivered on target. The wavelength is 1.053 μm. The laser was focused onto target using an f/ 7.6 parabola and the spot size was 15 μm FWHM. The laser intensity was from 10^{18} to 10^{19} W /cm^2. The laser was incident at an angle of 26° to the target normal. These experiments used a variety of target materials in both single and multilayer structures. The interaction surfaces of target were Cu, Au, Al, and Ti and the target thickness ranged from 5 to 100 μm. Two different electron spectrometers (ESMs_ were used for the Energetic electron spectrum characterization. Both have been extensively tested and calibrated on other laser-plasma interaction experiments. The ESM was placed behind the target and measured the Energetic electron energy spectra. Fujifilm imaging plates were used as the detectors. In spite of such broad range of conditions, only the laser intensity shows a clear dependence.

III.B. Energetic Electron Spectra

Energetic electron spectra measured along the laser axis are shown in Figs. 3(a) and 3(b). In Fig. 3(a) the GXII PW was used at an intensity at 6 x 10^{18} W/cm^2 on 100 μm thick Al. In Fig. 3(b) the VULCAN PW was used at an intensity of 3 10^{20} /cm^2 on 25 μm thick Cu. The longitudinal axes are the electron numbers and the horizontal axes are the electron energy. The dots represent the experimental results. The measured energy spectra were fitted with an approximation of relativistic Maxwellian distribution with the electron temperature T of the form[18]

$$N(E) = N_0 E^2 \exp(-E/T). \quad (1)$$

Here N_0, E, and T are the electron number, the electron energy, and the electron temperature, respectively. The

Energetic electron spectra indicate good agreements with these relativistic Maxwellian distributions. A wide energy range of Energetic electrons may be generated at the irradiation spot while those electrons are subject to the static potential formation especially of low energy less than 1 MeV. A warmer component is seen in Fig. 3(a).

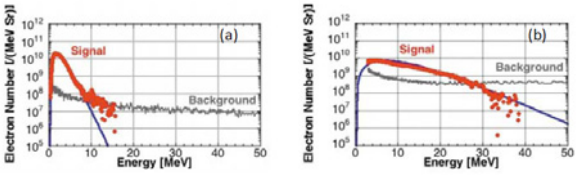

FIG. 3. Typical calibrated electron spectra measured at two different institutes. Signals are indicated as dots. Line embedded in the signals indicates fitting with a relativistic Maxwellian equation (1). The background noise level is also indicated.

However, based on our data reduction the figure has the line of background noise level as shown in the figure. This curve may cover the warmer population appearing at above 10 MeV in Fig. 3(a) and the data above 30 MeV in Fig. 3(b). These components may not be suitable for the discussion. We have estimated the values taking account of the solid angle and angular divergence of Energetic electrons. The Vulcan case corresponds to 0.018% and the Osaka case 0.008% of conversion efficiency compared to the incident laser energy assuming an average divergence angle of 40°. Only small fraction of electrons can escape from the targets due to the static potential and Alfven limit. The measured Energetic electron slope temperature was compared with the Wilks' ponderomotive scaling of the form[3]

$$T\,(\mathrm{MeV}) = 0.511[(1+I_{18}\lambda^2_{\mu m}/1.37)^{1/2}-1] \qquad (2)$$

where T, I_{18}, and $\lambda_{\mu m}$ are the electron temperature, the laser intensity in units of 10^{18} W/cm^2, and the wavelength in microns, respectively. Those plots are shown in Fig. 4. The dotted line is the calculation of the electron temperature from this ponderomotive scaling. In Fig. 4 the data show a clear departure from the Wilks' scaling and a good consistency with that Chen's observation of a reduction in the Energetic electron temperature compared with the ponderomotive potential energy is robust under a range of different irradiation conditions. In a most recent study of Energetic electrons measured both within targets and at ESMs show that the spectra are very much alike.

It is of great importance to point out here that this scaling is in favor for fast ignition upcoming integral experiments; rather high irradiation laser intensity can be used to generate Energetic electrons within a modest slope temperature. Those experiments will use 1–10 ps ultraintense laser pulse to fast heat a highly compressed fuel to achieve several keV core temperature[19].

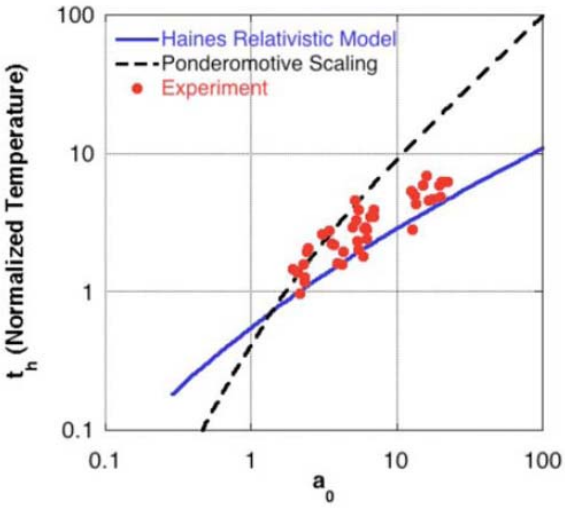

FIG. 5. Plot of the experimental Energetic electron temperature (normalized to m_ec^2 vs a_0 shown as dots. Also shown is the ponderomotive potential energy as dotted line (Ref. 3) and Haines' relativistic model as line [21].

A novel explanation for the $I^{1/3}$ intensity scaling in Fig. 4, one that reproduces previous results up to 10^{19} W /cm^2 [29] as well as more recent bremsstrahlung radiation measurements of electron entering the target up to 10^{21} W/cm^2, is briefly reviewed. The laser-plasma interaction region is treated as a one-dimensional "black box," the thickness of which is a few collision less skin depths. Relativistic conservation equations are then applied to this region, rather in the same way as in a shock transition. This very simple model leads to $t_h=(1+2^{1/2}a_0)^{1/2}-1$ (Haines relativistic model), where t_h is the normalized electron temperature, a_0 is the dimensionless magnetic vector potential associated with the laser electric field amplitude E_0 which has an angular laser frequency ω, $a_0 = eE_0 / \omega m_e c$. This model is discussed in detail in Ref. 21. The scaling based on the relativistic model shows very good consistency with the experiment within the laser intensity range between a_0=1 and a_0=30 (see Fig. 4 and caption).

IV. SUMMARY

We have investigated the propagation of intense laser, namely, a 100 TW 0.6 ps laser at several 10^{18} W/cm^2 in large scale plasmas. In the 100 TW experiments, plasma channel formation along the laser axis was observed in a preformed plasma with 100 μm density scale length and peak density 10 n_c. Over 1 MeV Energetic electrons with a beam divergence of about 30° were emitted along the laser axis.

The electron temperature of Energetic electron escaping to an electron spectrometer located on the target chamber wall was measured for a variety of different laser conditions using two different petawatt laser facilities. These new results are consistent with both bremsstrahlung radiation measurements generated from electrons enteringthe overdense plasma as well as analytic models that include both energy and momentum conservation. It has been found that the departure from the ponderomotive scaling of the Energetic electron temperature as a function of intensity on target is robust and occurs under a range of different irradiation conditions. The obtained scaling gives a wider range of laser intensity window for modest temperature of Energetic electrons that could be utilized for designing upcoming integral fast ignition experiments compared to the one based on the ponderomotive scaling.

ACKNOWLEDGMENTS

The valuable contributions are appreciated from profs. Anle Lei, T. Tanimoto, H. Azechi, F. Beg, R. Kodama, K. Kondo, H. Habara, K. Lancaster, K. Lancaster, K. Mima, T. Nakamura, T. Notimatsu, P Norreys, A Pukhov, Y. Sentoku, R. Stephens, and T. Yabuuchi. This work was partially supported by the JSPS-CAS Core-University Program in the field of Laser Plasma and High Energy Density Physics.

REFERENCES

[1] A. B. Borisov, V. Borovskiy, V. V. Korobkin, A. M. Prokhorov, O. B. Shiryaev, X. M. Shi, T. S. Luk, A. McPherson, J. C. Solem, K. Boyer, and C. K. Rhodes, Phys. Rev. Lett. **68**, 2309 (1992).
[2] V. A. Vshivkov, N. M. Naumova, F. Pegoraro, and S. V. Bulanov, Phys. Plasmas **5**, 2727 (1998).
[3] S. C. Wilks, W. L. Kruer, M. Tabak, and A. B. Langdon, Phys. Rev. Lett. **69**, 1383 (1992).
[4] K. A. Tanaka, R. Kodama, H. Fujima, M. Heya, N. Izumi, Y. Kato, Y. Kitagawa, K. Mima, N. Miyanaga, T. Norimatsu, A. Pukhov, A. Sunahara, K. Takahashi, M. Allen, H. Habara, T. Habara, T. Iwatani, T. Matusita, T. Miyakosi, M. Mori, H. Setoguchi, T. Sonomoto, K. Suzuki, H. Yoshida, T. Yamanaka, Y. Sentoku, F. Weber, T. W. Barbee, Jr., and L. Da Silva, Phys. Plasmas **7**, 2014 (2000).
[5] R. Kodama, K. Mima, K. A. Tanaka, Y. Kitagawa, H. Fujita, K. Takahashi, A. Sunahara, K. Fujita, H. Habara, T. Jitsuno, Y. Sentoku, T. Matsushita, T. Miyakoshi, N. Miyanaga, T. Norimatsu, H. Setoguchi, T. Sonomoto, M. Tanpo, Y. Toyama, and T. Yamanaka, Phys. Plasmas **8**, 2268 (2001).
[6] S. Atzeni, A. Schiavi, J. J. Honrubia, X. Ribeyre, G. Schurtz, Ph. Nicolai, M. Olazabal-Loume, C. Bellei, R. G. Evans, and J. R. Davies, Phys. Plasmas **15**, 056311 (2008).
[7] K. A. Tanaka, R. Kodama, H. Fujima, M. Heya, N. Izumi, Y. Kato, Y. Kitagawa, K. Mima, N. Miyanaga, T. Norimatsu, A. Pukhov, A. Sunahara, K. Takahashi, M. Allen, H. Habara, T. Habara, T. Iwatani, T. Matusita, T. Miyakosi, M. Mori, H. Setoguchi, T. Sonomoto, K. Suzuki, H. Yoshida, T. Yamanaka, Y. Sentoku, F. Weber, T. W. Barbee, Jr., and L. Da Silva, Phys. Plasmas **7**, 2014 (2000).
[8] R. Kodama, K. Mima, K. A. Tanaka, Y. Kitagawa, H. Fujita, K. Takahashi, A. Sunahara, K. Fujita, H. Habara, T. Jitsuno, Y. Sentoku, T. Matsushita, T. Miyakoshi, N. Miyanaga, T. Norimatsu, H. Setoguchi, T. Sonomoto, M. Tanpo, Y. Toyama, and T. Yamanaka, Phys. Plasmas **8**, 2268 (2001).
[9] Y. Kitagawa, H. Fujita, R. Kodama, H. Yoshida, S. Matsuo, T. Jitsuno, T. Kawasaki, H. Kitamura, T. Kanabe, S. Sakabe, K. Shigemori, N.Miyanaga, and Y. Izawa, IEEE J. Quantum Electron. **40**, 281 (2004).
[10] Y. Kitagawa, R. Kodama, K. Takahashi, M. Mori, M. Iwata, S. Tuji, K. Suzuki, K. Sawai, K. Hamada, K. Tanaka, H. Fujita, T. Kanabe, H. Takabe, H. Habara, Y. Kato, and K. Mima, Fusion Eng. Des. **44**, 261 (1999).
[11] A. L. Lei, A. Pukhov, R. Kodama, T. Yabuuchi, K. Adumi, K. Endo, R. R. Freeman, H. Habara, Y. Kitagawa, K. Kondo, G. R. Kumar, T. Matsuoka, K. Mima, H. Nagatomo, T. Norimatsu, O. Shorokhov, R. Snavely, X. Q. Yang, J. Zheng, and K. A. Tanaka, Phys. Rev. E **76**, 066403 (2007).
[12] T. Tanimoto, A. L. Lei, T. Yabuuchi, H. Habara, K. Kondo, R. Kodama, K. Mima, and K. A. Tanaka, J. Phys.: Conf. Ser. **112**, 022095 (2008).
[13] A. L. Lei, K. A. Tanaka, R. Kodama, G. R. Kumar, K. Nagai, T. Norimatsu, T. Yabuuchi, and K. Mima, Phys. Rev. Lett. **96**, 255006(2006).
[14] M. H. Key, M. D. Cable, T. E. Cowan, K. G. Estabrook, B. A. Hammel, S. P. Hatchett, E. A. Henry, D. E. Hinkel, J. D. Kilkenny, J. A. Koch, W. L. Kruer, A. B. Langdon, B. F. Lasinski, R. W. Lee, B. J. MacGowan, A. MacKinnon, J. D. Moody, M. J. Moran, A. A. Offenberger, D. M. Pennington, M. D. Perry, T. J. Phillips, T. C. Sangster, M. S. Singh, M. A. Stoyer, M. Tabak, G. L. Tietbohl, M. Tsukamoto, K. Wharton, and S. C. Wilks, Phys. Plasmas **5**, 1966 (1998).
[15] M. I. K. Santala, M. Zepf, I. Watts, F. N. Beg, E. Clark, M. Tatarakis, K. Krushelnick, A. E. Dangor, T. McCanny, I. Spencer, R. P. Singhal, K. W. D. Ledingham, S. C. Wilks, A. C. Machacek, J. S. Wark, R. Allott, R. J. Clarke, and P. A. Norreys, Phys. Rev. Lett. **84**, 1459 (2000).
[16] C. N. Danson, P. A. Brummitt, R. J. Clarke, J. L. Collier, B. Fell, A. J. Frackiewicz, S. Hancock, S. Hawkes, C. Hernandez-Gomez, P. Holligan, M. H. R. Hutchinson, A. Kidd, W. J. Lester, I. O. Musgrave, D. Neely, D. R. Neville, P. A. Norreys, D. A. Pepler, C. J. Reason, W. Shaikh, T. B. Winstone, R. W. W. Wyatt, and B. E. Wyborn, Nucl. Fusion **44**, S239 (2004).

[17] Y. Kitagawa, H. Fujita, R. Kodama, H. Yoshida, S. Matsuo, T. Jitsuno, T. Kawasaki, H. Kitamura, T. Kanabe, S. Sakabe, K. Shigemori, N. Miyanaga, and Y. Izawa, IEEE J. Quantum Electron. **40**, 281 (2004).
[18]T. Yabuuchi, K. Adumi, H. Habara, R. Kodama, K. Kondo, T. Tanimoto, K. A. Tanaka, Y. Sentoku, T. Matsuoka, Z. L. Chen, M. Tampo, A. L. Lei, and K. Mima, Phys. Plasmas **14**, 040706 (2007).
[19] K. Mima, K. A. Tanaka, R. Kodama, T. Johzaki, H. Nagatomo, H. Shiraga, N. Miyanaga, M. Murakami, H. Azechi, M. Nakai, T. Norimatu, K. Nagai, T. Taguchi, and H. Sakagami, Eur. Phys. J. D **44**, 259 (2007); D. N. Maywar, J. H. Kelly, L. J. Waxer, S. F. B. Morse, I. A. Begishev, J. Bromage, C. Dorrer, J. L. Edwards, L. Folnsbee, M. J. Guardalben, S. D. Jacobs, R. Jungquist, T. J. Kessler, R. W. Kidder, B. E. Kruschwitz, S. J. Loucks, J. R. Marciante, R. L. McCrory, D. D. Meyerhofer, A. V. Okishev, J. B. Oliver, G. Pien, J. Qiao, J. Puth, A. L. Rigatti, A. W. Schmid, M. J. ShoupIII, C. Stoeckl, K. A. Thorp, and J. D. Zuegel, J. Phys.: Conf. Ser. **112**, 032007 (2007).
[20]F. N. Beg, A. R. Bell, A. E. Dangor, C. N. Danson, A. P. Fews, M. E. Glinsky, B. A. Hammel, Glinsky, B. A. Hammel, P. Lee, P. A. Norreys, and M. Tatarakis, Phys. Plasmas **4**, 447 (1997).
[21]M. G. Haines, M. S. Wei, F. N. Beg, and R. B. Stephens, Phys. Rev. Lett. **102**, 045008 (2009).

Collimation of fast electrons by spontaneous magnetic fields in interactions of ultraintense laser pulses with solid targets

Reporter: Hong-bo Cai, and C. T. Zhou
(Institute of Applied Physics and Computational Mathematics, Beijing, China)
Host: CUP 2010, Shanghai, China

Recent status for high energy density physics studies in IAPCM has been introduced. In particular, the collimation of fast electrons in overdense plasma has been studied in detail. As is well known, fast ignition relies on efficient energy coupling of a petawatt-picosecond laser to heat the hot-spot region in the dense deuterium-tritium fuel to temperatures ~10keV. The laser energy firstly deposited into hot electrons in the interaction region, which is usually 50 to 100 microns away from the dense core, and the resulting energy flux transports into the dense core. Therefore, the propagation and collimation of hot electron beam in overdense plasmas are of particular importance since it will affect the laser coupling efficiency. In the present presentation, guided transport of a relativistic electron beam in overdense plasma is achieved by exploiting the strong magnetic fields created at the interface of two plasmas with different densities or electrical resistivities. It is found that the sandwich target, whose density (or resistivity) of the central target is higher, can generate a magnetic field by resistivity gradients, then acts to collimate electrons. It is consistent with Vlasov-Fokker-Planck hybrid simulation results by A. P. L. Robinson's [Phys. Plasmas 14, 083105 (2007)] as well as the experiments by S. Kar et al. [S. Kar et al., Phys. Rev. Lett. 102, 055001 (2009)]. However, the collisionless PIC simulations showed contrary results: the sandwich target whose density of the central target is lower is better to collimate electrons. In this presentation, electron collimation by different sandwich targets is studied via a collisional PIC code. The discrepancies between these conflicting results are elucidated.

II. Recent Status of high energy density studies in IAPCM

The numerical simulation plays an important role in estimating the feasibility and performance of fast ignition. There are three key issues in numerical analysis for the fast ignition: the implosion compression of the feul target, the generation of fast electrons by Petawatt-picosecond laser pulse, the transport and deposition of fast electrons in the compressed core. From initial laser irradiation to final fusion burning, all the physics are coupling strongly in any phase, and they must be solved consistently in computational simulation. Therefore, we developed integrated code for these issues. The implosion compression is studied by the radiation hydrodynamic code LARED-S; the laser plasma interaction and the generation of fast electrons are studied by PIC code ASCENT; the transport and deposition of fast electrons are studied by the hybrid code HFPIC.

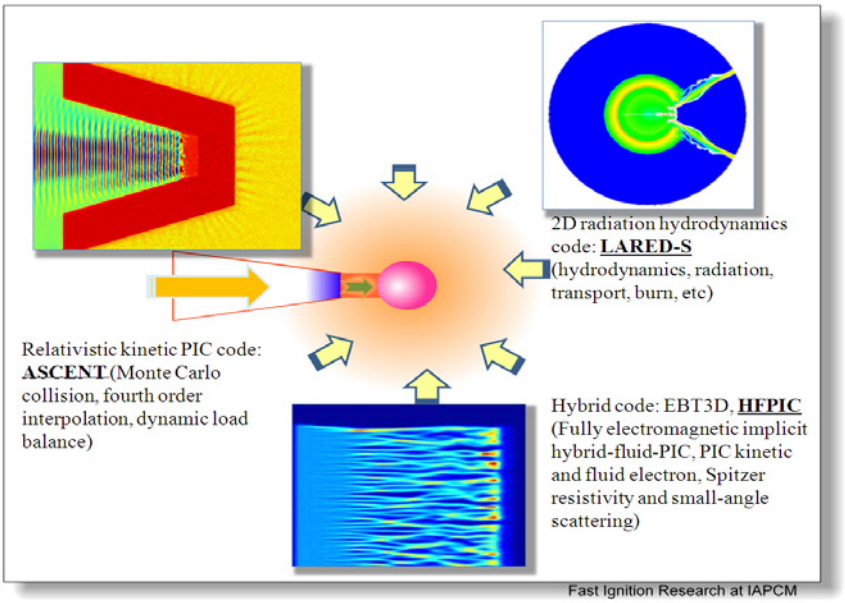

Fig. 1 Integrated code for fast ignition in IAPCM

III. Collimation of fast electrons in overdense plasmas

In order to describe the collisional effect on the generation of magnetic fields, firstly we study two different sandwish targets with 2.5D collisional particle-in-cell (PIC) simulation code ASCENT [H. B. Cai et al., Phys. Rev. Lett. 102, 245001 (2009)]: (1) Higher central density case and (2) Lower central density case. Figure 1 is a sketch of the geometry of the simulations. In the higher central density case, the middle target (Target 2) is fully ionized carbon (charge state Zi=6) with mi/meZi =1836*12/6. Target 1 and Target 3 are hydrogen plasma. The widths of three targets are: $6\lambda_0$, $6\lambda_0$, $6\lambda_0$, respectively. The densities of three targets are: $50n_c$, $200n_c$, $50n_c$, respectively. In the lower central density case, the middle target(Target 2) is hydrogen plasma while Target 1 and Target 3 are fully ionized carbon plasmas. The p-polarized laser pulse at $\lambda_0 = 1.06\mu m$ wavelength and $2\times10^{19} W/cm^2$ intensity irradiates the target from the left boundary. The intensity profile is Gaussian in the y direction with a spot size of $5.0\mu m$ (FWHM). The laser rises in $15T_0$, where T_0 is the laser period, after which the laser amplitude is kept constant.

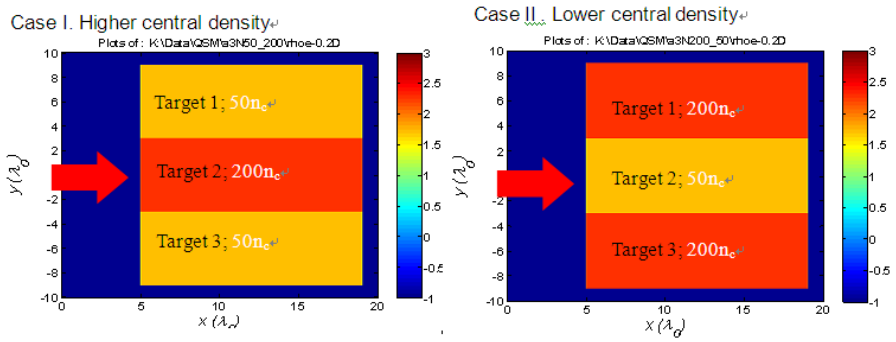

FIG. 2. Initial density profile of the sandwish target.

Here, we use a grid size of $\Delta x = \Delta y = \lambda_0 / 128$ with 2560×2560 grid cells. The time step used is $T_0 / 256$. 98 particles are used in one mesh, and the total number of particles is about 3.35×10^8. Both the field and particle boundary conditions are absorbing boundary conditions, either in the x or the y direction. In order to reduce the restrictions on the grid size compared with the Debye length, we used a fourth-order interpolation scheme to evaluate fields and currents.

In our code ASCENT, the binary collision module is based on Takizuka and Abe's model, and is extended to treat collisions between wighted macroparticles and among different species of macroparticles relativistically.

IV. Excitation of quasi-static magnetic fields at the density/resistivity jump

The crucial issue for the fast ignitor is the generation and transport of enormous numbers of high-energy charge particles to the compressed core. In recent experiments at Rutherford Appleton Laboratory employing VULCAN petawatt laser system, sandwish targets [a thin slab of tin (Sn) with aluminum (Al) either side] are expected to take advantages in collimating fast electrons. The mechanism proposed to transversely confine the fast electrons relies on the fact that in the sandwish target, strong resistivity gradient along the Al/Sn boundary will lead to rapid magnetic field growth and consequently guiding of the fast electrons. The most familiar example of this effect is introduced by Robinson and Sherlock [A. P. L. Robinson and M. Sherlock, Phys. Plasmas 14, 083105 (2007)], who proposed a radically different route to artificially forcing collimated beam transport to occur. In his study, a structured target in which the resistivity varies in the direction transverse to the electron beam propagation. The resistivity jump then leads to the growth of the magnetic field. Furthermore, PIC simulations [S. Z. Wu et al, Phys. Plasmas 17, 063103 (2010)] showed the density jump in a structured two-layer target also can collimate electrons. However, in this model, the density of the middle layer is much lower than the density of the side layer.

The preceding geometry is very close to the simulations that were performed in Ref. [Wu], but our work was performed with several differences: (1) binary Monte-Carlo collision is included, (2) two materials with different Z are considered, and (3) the density is much higher. These three points enable us to study the magnetic fields caused by the resistivity jump since the Spitzer resistivity (ideal gas specific heat capacity) relies only on the charge state Z and temperature[A. P. L. Robinson et al., Phys. Plasmas 14, 083105 (2007)], $\eta = 10^{-4} Z \ln\Lambda / T_c^{3/2}$.

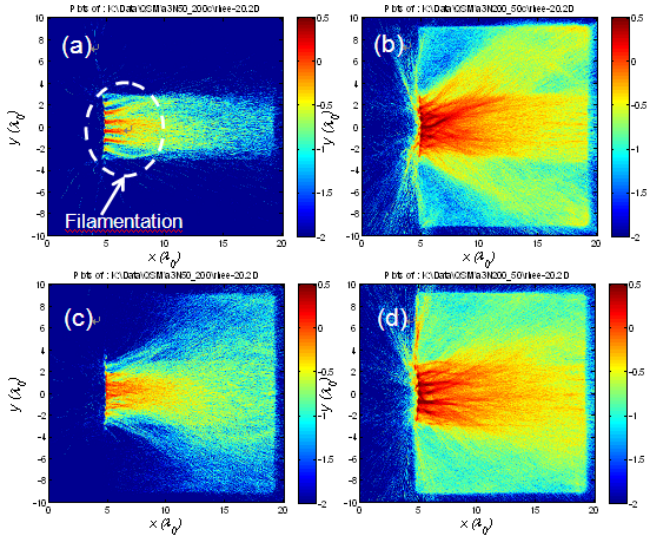

Fig. 3. The natural logarithm of the electron energy density at t=80T0 for (a)(c) higher central density target and (b)(d) lower central density target. (a)(b) with collision, (c)(d) without collision.

To determine the collisional effect on the generation of magnetic field and the collimation of fast electron, we studied both the cases with and without collision for the higher central density target and lower central density target. Fig. 3 shows the natural logarithm of the electron energy density at t=80T0. It is clearly seen that the fast electrons are only collimated for the case of higher central density target with collision. In the case of higher central density target without collision, the fast electrons have a very large divergence angle (~40 degree). It means that for the collisionless case the collimation effect is weak. While in the lower central density target case, fast electrons are scattered at the interface, especially for the case with collision.

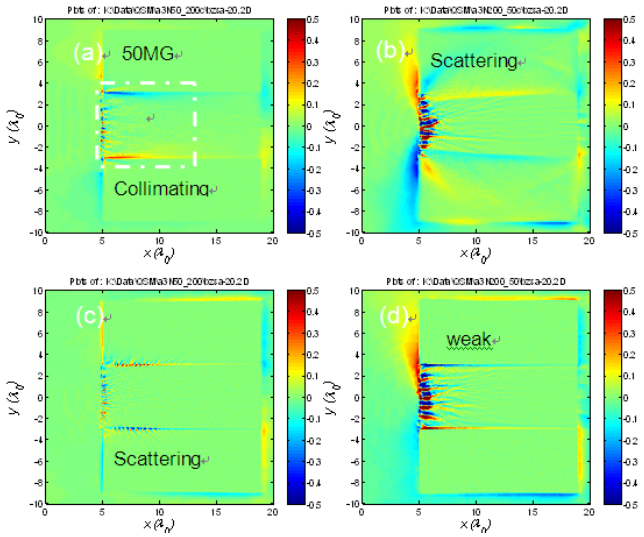

Fig. 4. The quasi-static magnetic fields at time t=80T0 for (a)(c) higher central density target and (b)(d) lower central density target. (a)(b) with collision, (c)(d) without collision. Here, the magnetic fields are averaged over one laser period. The unit of the magnetic field is $m_e\omega_0 c/e$ (1 unit = 100MG) .

The generation of magnetic fields during the propagation of fast electrons through a solid target can be described by combining a simple Ohm's law ($\mathbf{E}=-\eta\mathbf{j}_f$) with Faraday's law to yield[A. R. Bell, J. R. Davies, S. M. Guerin, Phys. Rev. E 58, 2471 (1998)]

$$\partial_t\mathbf{B}=\eta\nabla\times\mathbf{j}_f+\nabla\eta\times\mathbf{j}_f$$

Where η is the resistivity, and $\mathbf{j}_f$ is the fast electron current density. In solid density case, the generation of the collimating magnetic field is mainly due to the interplay of two effects. It has been explained by Davies[J. R. Davies, Phys. Rev. E 68, 056404 (2003)]. The first term on the right-hand side generates a magnetic field that pushes fast electrons towards regions of higher fast electron current density, while the second term pushes fast electrons towards regions of higher resistivity. Fig. 4 shows the quasi-static magnetic fields at time t=80T0 for (a)(c) higher central density target and (b)(d) lower central density target. Clearly, only the case of higher central density target with collision generates a magnetic field at the interface, which can collimate the fast electrons. In this case, the resistivity jump, which is due to the difference of the charge state, dominates the generation of the magnetic fields, which can be as high as 50MG. While in the lower central density target case, the generated magnetic field plays a role in scattering the fast electrons. Note that for the collisionless cases, the magnetic field can not be generated from the resistivity jump since the resistivity keeps zero.

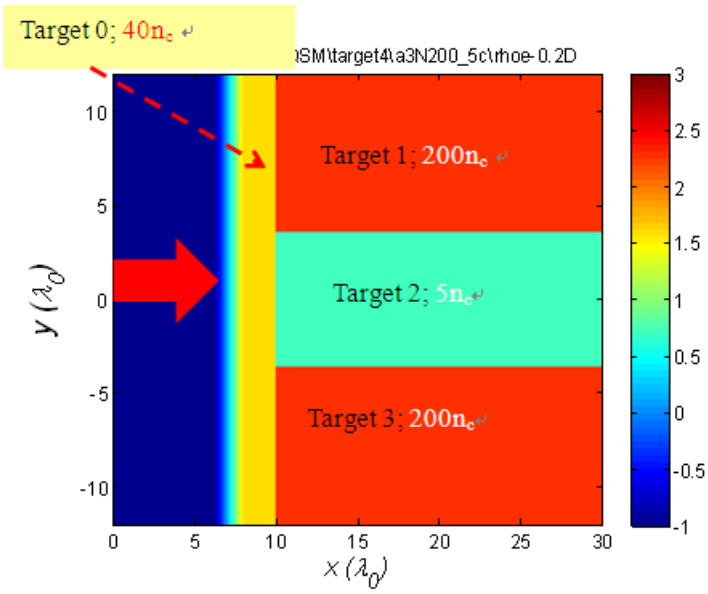

FIG. 5. Initial density profile of the third sandwish target case.

V. The reason for the discrepancy between Fokker-Planck simulation and PIC simulation

We reproduced the generation of magnetic field by the resistivity jump, which has been shown by 2D hybrid-Vlasov-Fokker-Planck code. However, we still need to answer the following question—what is the reason for the discrepancy between Fokker-Planck simulation and PIC simulation? Now, we studied a third sandwich target case. In this case, the middle target has been replaced by the low density carbon foam, whose density is only 5nc. In order to avoid the ruin of the carbon foam by the laser pressure, we placed another high density target (40nc) in front of the sandwich target, as shown in Fig. 5.

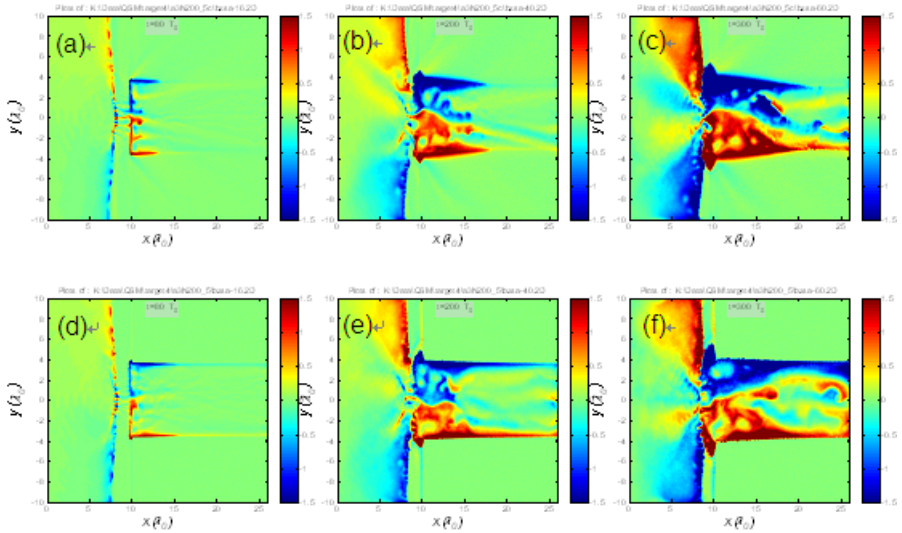

Fig. 6. The quasi-static magnetic fields at different times (a)(d) t=80T0, (b)(e) t=200T0, and (c)(f) for (a)(c) t=300T0. (a)(b)(c) are for the case with collision and

(d)(e)(f) for the case without collision.

Figure 6 shows the quasi-static magnetic fields at three different times: (a)(d) t=80T0, (b)(e) t=200T0, and (c)(f) for (a)(c) t=300T0. It has been found that both the collisional and collisionless cases can generate a magnetic field at the interface of the plasma jump. The magnetic fields at the interface first appear at the region close to the laser plasma interaction region. As time goes on, the magnetic fields grow to the rear side of the target because of the transport of fast electrons. Note that the magnetic fields can reach as high as 150MG, which is much higher than that in Case I and Case II.

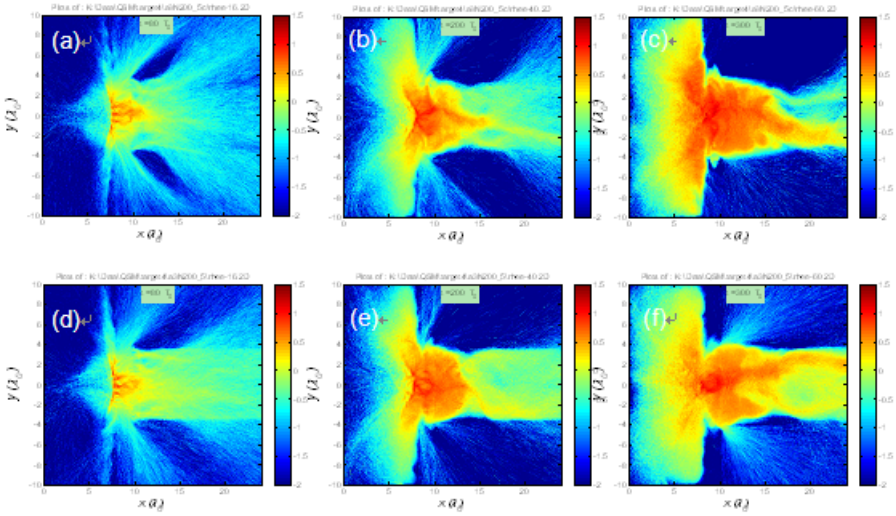

Fig. 7. The natural logarithm of the electron energy density at different times (a)(d) t=80T0, (b)(e) t=200T0, and (c)(f) for (a)(c) t=300T0. (a)(b)(c) are for the case with collision and (d)(e)(f) for the case without collision.

In Fig. 7 the natural logarithm of the electron energy with energy between $0.5 \le E[MeV] \le 2.0$ are plotted. It is clearly seen that the high-energy electrons are collimated well at later time for both cases. In the collisional case, initially the electrons have a larger divergence angle than the collisionless case, but they are also collimated by the magnetic fields at later time. In comparison, in the collisionless case, the electron collimation effect develops faster and better.

In the collisionless case, the resistivity jump is zero while the magnetic fields can still be as high as 150MG. Therefore, there should have some other mechanisms for the generation of the magnetic fields. It is found a very large surface current has been formed at the surface, which was caused by the return electrons, as shown in Fig. 8. This current is the main reason for the generation of the magnetic fields. Now, we have shown that the lower central density target whose density of the middle target is quite low can collimate electrons. It is quite different from Fokker-Planck's simulation result. What is the reason for this discrepancy between Fokker-Planck's simulation and PIC simulation here? Let's firstly check back on Fokker-Planck model. The electromagnetic fields are obtained from Ohm's law and Faraday's law. However, there are several conditions to be satisfied for using Ohm's law: the number density of the fast electrons is very much less than that of the background electrons and the

current neutralization can be fulfilled. These conditions are clearly fulfilled by high-intensity laser generated fast electrons propagating in solids. However, in moderately overdense plasma, these conditions are hardly satisfied. That is to say, Fokker-planck simulation can not handle the present moderately overdense plasma described in case III. This is the reason why Fokker-planck simulation did not find the collimation effect of case III. In comparison, the PIC simulation can still handle it.

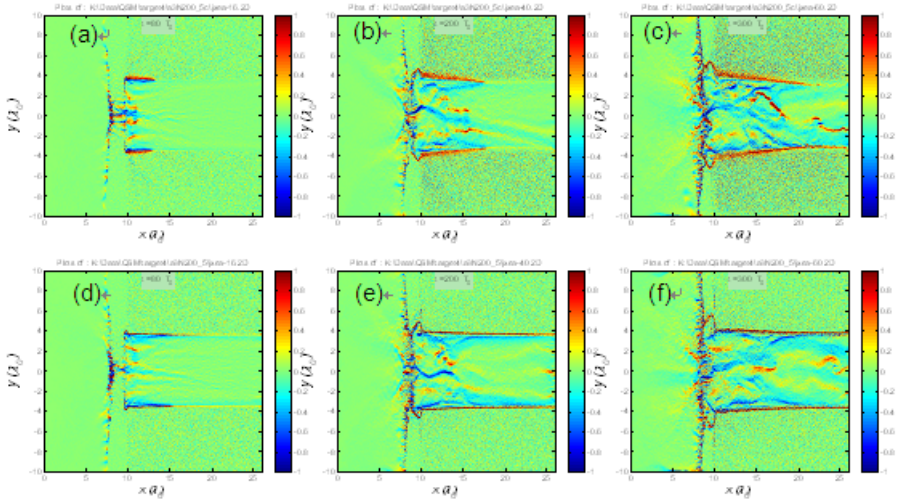

Fig. 8. The averaged electron current at different times (a)(d) t=80T0, (b)(e) t=200T0, and (c)(f) for (a)(c) t=300T0. (a)(b)(c) are for the case with collision and (d)(e)(f) for the case without collision. The current is averaged over one laser period.

VI Summary

In summary, we performed 2.5D PIC simulations to study the collimation of fast electrons in different sandwich targets. Our simulation results indicate that the fast electrons can be collimated by the case of higher central density target with collision, which is consistent with the simulation results of Fokker-Planck code. It is also found that for a lower central density target whose density of the middle target is much smaller than the density for current neutralization can collimate fast electrons well.

Acknowledgements

I would like to acknowledge the JSPS-China core-university program's support. I also would like to thank the collaboration of some Japanese researchers, Prof K. Mima, Prof. H. Nagatomo, Prof. H. Sagakami and other colleagues.

References

[1] A. P. L. Robinson et al., Phys. Plasmas 14, 083105 (2007).
[2] S. Kar et al., Phys. Rev. Lett. 102, 055001 (2009).
[3] S. Z. Wu et al, Phys. Plasmas 17, 063103 (2010).
[4] C. T. Zhou et al., Applied Phys. Lett., 92, 151502 (2008).
[5] A. R. Bell, J. R. Davies, S. M. Guerin, Phys. Rev. E 58, 2471 (1998).

[6] J. R. Davies, Phys. Rev. E 68, 056404 (2003).
[7] A. P. L. Robinson, M. Sherlock, and P. A. Norreys, Phys. Rev. Lett. 100, 025002 (2008).

Grand Challenge Laser Astrophysics on Weibel Instability, meta- and micro-scale Magnetic Turbulence Resulting Nonlinear Structure Formation of High-Mach Collisionless Shock and Stochastic Cosmic Ray Acceleration

Hideaki Takabe
ILE, Osaka University
takabe(at)ile.osaka-u.ac.jp

The origin of ultra-high-energy cosmic rays is still open question. It is said that the cosmic-ray particle of proton whose energy is less that 10^{15}eV is accelerated in our Galaxy and they are mainly accelerated by the supernova remnants(SNRs).

The standard model is the stochastic diffusive acceleration around the shock surface of SNR. It is, however, still open question why shock waves are generated and how the electro-magnetic turbulence is generated and dissipated following the shock front.

We have proposed a new physics for the generation of the collisonless shock formation through Weibel instability [1]. We can reproduce the physics in PIC simulations; however, it is necessary to proof experimentally in order to persuade the most of opinion makers in Astrophysics, who are now skeptical about the simulation after many experience that simulation can reproduce observation data but it has many of adjustable parameters.

I would like to explain the physics scenario and also pointed out that magnetic reconnection should also couples with this phenomenon when currents filaments coalescence in the nonlinear stage of the Weibel instability. We also plan to carry out a model experiment regarding the magnetic reconnection phenomena to investigate what kind of waves, shocks, and/or jets are generated in the reconnection.

Finally, I would like to explain whole scenario to clarify the physics of cosmic ray acceleration to be confirmed with big laser facilities.

[1] H. Takabe, Plasma Physics and Controlled Fusion **50**, 124057 (2008).

*Full paper was not submitted by authors.

Laser driven particle accelerator based on nanometer-scale targets

X. Q. Yan

State Key Lab. of Nuclear Physics & Technology at Peking University, Beijing 100871, China

Abstract:

Ultrahigh-intensity lasers can produce accelerating fields of 10 TV/m, surpassing those in conventional accelerators for ions by six orders of magnitude. Remarkable progress has been made in producing laser-driven ultra-bright MeV proton and ion beams in a very compact fashion compared to conventional RF accelerators. These beams have been produced up to several MeV per nucleon with outstanding properties in terms of transverse emittance and current, but typically suffer from exponential energy distributions. Recently, radiation pressure acceleration (RPA) has been proposed and extensively studied, which shows circularly polarized (CP) laser pulses can accelerate mono-energetic ion bunches in a phase-stable-acceleration (PSA) way from ultrathin foils. However, acceleration normally terminates due to multi-dimensional effects such as transverse expansion of the accelerated ion bunch and transverse instabilities. In particular, instabilities grow in the wings of the indented foil, where light is obliquely incident and strong electron heating sets in. For appropriate parameters, CP pulses may accelerate foils as a whole with most of the transferred energy carried by ions like in 1D case. It is found that self-organizing proton beam can be stably accelerated to GeV in the interaction of a CP laser with a planar target at ~$10^{22} W/cm^2$.

TEXT:

State-of-the-art lasers can deliver ultraintense, ultrashort laser pulses with very high contrast ratios. These systems can avoid the formation of plasma by the prepulse, thus opening the way to laser-solid interactions with ultra-thin solid targets. Solid targets irradiated by a short pulse laser can be an efficient and flexible source of MeV protons. They are already applied to produce high-energy density matter or to radiograph transient processes, and for applications such as tumor therapy, isotope generation for positron emission tomography, and fast ignition of fusion cores.

In the intense-laser interaction with solid foils, usually there are three groups of accelerated ions. The first two occur at the front surface, moving backward and forward, respectively, and the third one is sheath acceleration (TNSA) that occurs at the rear surface. As these output beams are accelerated only by electrostatic fields and have no longitudinal bunching in (x, p_x) plane, their distribution profiles used to be exponential nearly with 100% energy spread. Although some techniques can be used to decreasing the energy spread, however, they rely on relatively complicated target fabrication.

In these surface acceleration mechanisms, the linear polarized (LP) laser pulse is used and the J $\times$B heating [13] is efficient to generate the hot electrons. For a circularly polarized (CP) laser pulse with the electrical field $E_L = E(x)(\sin(\omega_L t)\hat{y} + \cos(\omega_L t)\hat{z})$, however, the ponderomotive force is $\vec{f}_p = -\frac{m_e c^2}{4}\frac{\partial}{\partial x} a_L^2(x)\hat{x}$ and its oscillating part vanishes. Here $a_L(x) = eE/m_e\omega_L c$ is the normalized laser amplitude, and m_e, ω_L and e are the electron mass, laser frequency and charge,

respectively. When a CP laser is normally incident on a thin foil, the electrons are pushed forward steadily by the ponderomotive force. By use of this feature, Shen et al. [14] had proposed to utilize two CP laser pulses to compress deuterium plasma for ICF studies; Macchi et al. found that high current proton beams are also generated by a CP laser, whereas the ions bunching and acceleration were not noticed in these studies. In this letter, we propose that there is a regime of proton acceleration in the interaction of a CP laser with a thin foil in a certain parameter range, where the proton beam is synchronously accelerated and bunched like in a conventional RF linac. The acceleration mechanism is thus named as Phase Stable Acceleration (PSA). An analytic model is presented to show the acceleration and bunching processes duration the laser interaction.

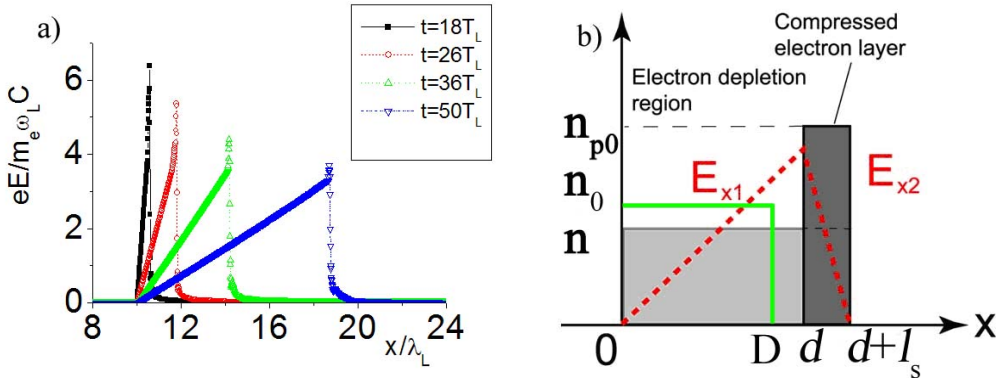

Fig. 1 (color online) (a) Snapshots of the spatial distributions of the electrostatic fields at different time, where the initial plasma density $n_0/n_c=10$ and thickness $D=0.2\lambda_L$, normalized laser peak-amplitude $a_L=5$ and pulse duration τ=100T_L; (b) Schematic of the equilibrium density profiles for ions (n) and electrons (n_{p0}). The x position at $x=d$ indicates the electron front, where the laser evanescence starts and it vanishes at x=d+ l_s, where l_s is the plasma skin depth. The initial plasma density n_0 and target thickness D are also plotted.

In our simulation a laser pulse with a peak amplitude $a_L=5$ and the duration 100 T_L is normally incident on a plasma slab, where T_L is a laser period. To simplify the model, a low density purely hydrogen plasma with a step density profile is used (the initial normalized density $n_0/n_c=10$ and thickness $D=0.2\lambda_L$). The target boundary is located at $x=10\lambda_L$ and the laser front impinges on it at $t=10T_L$. We take 100~500 particles per cell per species and the cell size of $\lambda_L/100$.

Figure 1(a) shows the snapshots of the electrostatic field profile. Due to the ponderomotive push, the electrons are quickly piled up in the front of the CP laser pulse and an electron depletion region is left behind. The depletion region increases with time, then the ion density is decreased in the debunching process. In the compressed electron layer, it is found that the width of the layer remains to be equal to the skin depth ($l_s\cong\lambda_L/20$). The charge separation field in this layer nearly keeps the same steep linear profile. Therefore a simple 1D model can be used [see Fig. 1(b)]. The induced electrostatic fields have linear profiles both in the depletion region ($E_{x1}=E_0x/d$ for $0<x<d$) and in the compression layer ($E_{x2}=E_0[1-(x-d)/l_s]$ for $d<x<d+l_s$). The parameters E_0,

n_{p0} and l_s are related by equations $E_0 = 4\pi end$ and $n_{p0} l_s = nd \approx n_0 D$. When the light pressure exerted on the electrons $(1+\eta) I_L / c$ (with η is the reflecting efficiency) is assumed to be balanced by $E_0 e n_{p0} l_s / 2$, the electrostatic pressure from depletion region. Usually one has $D \geq l_s$, therefore the balance condition can be expressed as

$$a_L (1+\eta)^{1/2} \sim (n_0 / n_c)(D / \lambda_L) . \tag{1}$$

To obtain this expression, we have taken $I_L \lambda_L^2 = \pi P_0 a_L^2 = [2.74 \times 10^{18} W / cm^2 \mu m^2] a_L^2$ with $P_0 = m_e^2 c^5 / e^2 = 8.67 GW$. If the laser field E_L is larger than maximum charge separation field $E_{//}$, all electrons will be displaced, then no balance exists. So we find the second conditions for PSA $E_{//} = 4\pi e n_0 D > (v_e \times B_L / c) \sim E_L$ or

$$a_L < (n_0 / n_c)(2\pi D / \lambda_L) . \tag{2}$$

The steep profile of the electrostatic field Ex_2 is kept until the laser pulse is over [see Fig. 1(a)], which always provides a longitudinal restoring force for the ions in the compressed electron layer. Just like the phase-stable acceleration in the conventional RF Linac, when a proper synchronous phase is chosen the early ions experience a smaller field, and the late ions a larger field than the synchronous particle, which is kept in synchronization with the accelerating field. As the ions execute longitudinal oscillations under the restoring force Ex_2, a reference particle is similarly introduced to explain the phase motion. The reference particle is assumed to remain in synchronization with the compressed electron layer, which moves at a high speed under the ponderomotive force.

In order to describe the interaction between ions and the electron layer, we derive dynamic equations for ions in the following. Denote $\xi = (x_i - x_r)$ with $-l_s/2 \leq \xi \leq l_s/2$, where $x_r = d + l_s/2$ represents the position for the reference particle and x_i the position for a test ion located inside the electron layer. The force acting on the test ion is given by $F_i = q_i E_0 [1 - (x_i - d)/l_s]$. Thus, the equation motion for the ion is $\frac{d(m_i \gamma_i \dot{x}_i)}{dt} = q_i E_0 \left[1 - (x_i - d)/l\right]$ or $\frac{d^2 x_i}{dt^2} = \frac{q_i E_0}{m_i \gamma_i^3} \left[1 - (x_i - d)/l_s\right]$, where γ_i is the relativistic factor for the reference particle. The phase motion (ξ, t) around the reference particle can be written approximately as:

$$\ddot{\xi} = -\Omega^2 \xi, \qquad \Omega^2 = \frac{q_i E_0}{m_i l_s \gamma_i^3} \quad , \tag{3}$$

where it is assumed that $\gamma_i \approx \gamma_r$. Furthermore if both γ_i and E_0 vary slowly in a time scale of $1/\Omega$, then the longitudinal phase motion (ξ, t) is a harmonic oscillation $\xi = \xi_0 \sin(\Omega t)$. The beam energy spread can be estimated from the harmonic oscillation: $\dot{\xi} = \xi_0 \Omega \cos(\Omega t)$ and $\Delta w / w_r \cong 2\Delta p / p_r \cong 2\xi_0 \Omega / p_r$, where w_r and p_r are the kinetic energy and momentum of the

reference particle, respectively, and ξ_0 is the oscillating amplitude. The ion located in $\xi < -l_s/2$ will be debunched and lost in the acceleration process. Some ions maybe were rapidly accelerated by the electrostatic shock and had overran the electron layer, whereas they will get no more energy until coming back into the electron layer. So the particle displacement in the oscillation is $\xi_{\max} \le l_s/2$ and maximum energy spread of the accelerated beam is determined by $\Delta w/w_r \cong l_s\Omega/p_r$. The harmonic oscillation frequency Ω decreases with the increase of particle energy. For the simulation parameters as given in Fig. 1(a) with $a_L=5$, $n_0/n_c=10$, and $\gamma=1$ for protons at the beginning, the first period of phase oscillation is about $8T_L$ and the period will lengthen as long as E_0 and $1/\gamma$ are decreased. If the final energy of the reference particle w_r = 300 MeV, the estimated energy spread $\Delta w/w_r$ will be less than 5%. These are well-verified in our PIC simulations.

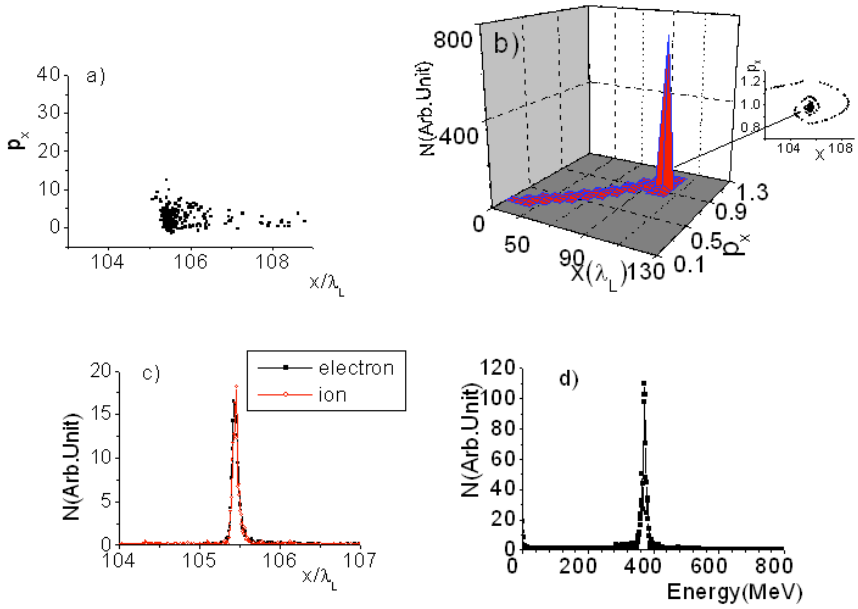

Fig. 2 (color online) (a) Phase space distribution of electrons; (b) Phase space distribution of protons; (c) Electrons and protons density profiles; (d) Energy spectrum of protons. The results are found at t=200 T_L when the laser interaction is almost terminated. The laser and plasma parameters are the same as in Fig. 1.

The snapshots of phase-space distributions of electrons and ions at t=200 T_L are plotted in Fig. 2(a) and Fig. 2(b). It shows a bunched proton beam with a very high density is formed in the phase space (x,p_x), because protons inside the compressed electron layer always execute periodical oscillations as described by Eq. (3). The protons in the electron depletion region (between x=0 and 100) are debunched and form a long tail in the phase space, however, its density is two-orders lower than in the compressed electron layer. As a result, the debunched protons look disappearing in the proton spatial distribution and the proton energy spectrum, which are shown in Fig. 2(c) and Fig. 2(d), respectively. Fig. 2(c) implies both particles have the same density profiles and a

quasi-neutral beam is therefore obtained. In this case, the space charge fields are weak and the proton beam can propagate over a long distance without explosion, which is advantageous to transport the high current ion beams in applications. The energetic proton beam has a low FWHM energy spread (< 4%) and high peak current as shown in Fig. 2(d). The energy spread is completely in agreement with our earlier estimation based upon Eq. (3). Note that the proton bunch has an ultrashort length about the skin depth l_s or about 250 attoseconds in time (λ_L=800 nm). The number of accelerated protons in the bunch is about $n_0 l_s \sigma$, where σ is the focused beam spot area. This gives about 5×10^{12} quasi-monoenergetic protons for a focused beam diameter of 40μm in the present simulation.

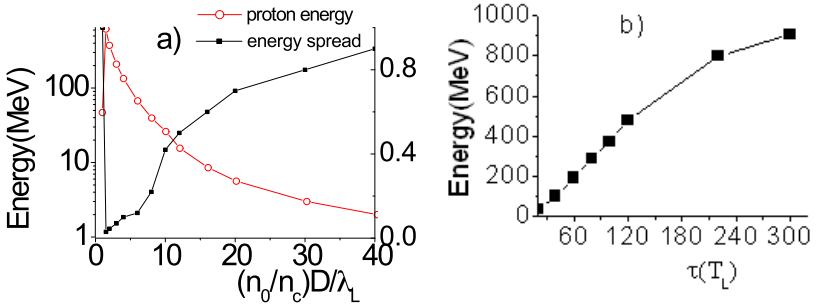

Fig. 3 (a) Proton energy of the mono-energetic peak versus target thickness and density for a_L=5 and laser pulse duration τ=100 T_L; (b) Proton energy of the mono-energetic peak versus laser pulse duration for a_L=5, $n_0/n_c=10$, and D=0.2λ_L.

In 1D simulations it is found that the proton energy depends on the product of target density and thickness. The proton energy and the energy spread are plotted versus the electron area density in Fig. 3(a). It shows that the energy spread can be optimized near the condition $a_L \sim (n_0/n_c)D/\lambda_L$. Figure 3(b) suggests that the proton energy increases almost linearly with the laser pulse duration at first, Later it turns to be saturated because the protons become relativistic.

For appropriate parameters, CP pulses may accelerate foils as a whole with most of the transferred energy carried by ions. The basic dynamics are well described by a one-dimensional (1D) PSA model. Acceleration terminates due to multi-dimensional effects such as transverse expansion of the accelerated ion bunch and transverse instabilities. In particular, instabilities grow in the wings of the indented foil, where light is obliquely incident and strong electron heating sets in. Eventually, this part of the foil is diluted and becomes transparent to the driving laser light**.** The central new observation in the present paper is that this process of foil dispersion may stop before reaching the centre of the focal spot and that a relatively stable ion clump forms near the laser axis which is efficiently accelerated. The dense clump is about 1 - 2 laser wavelengths in diameter. The stabilization is related to the driving laser pulse that has passed the dispersed foil in the transparent wing region and starts to encompass the opaque clump, keeping it together. Acceleration is then similar to that studied for so-called *reduced mass targets*, where small droplets or clusters are used as targets.

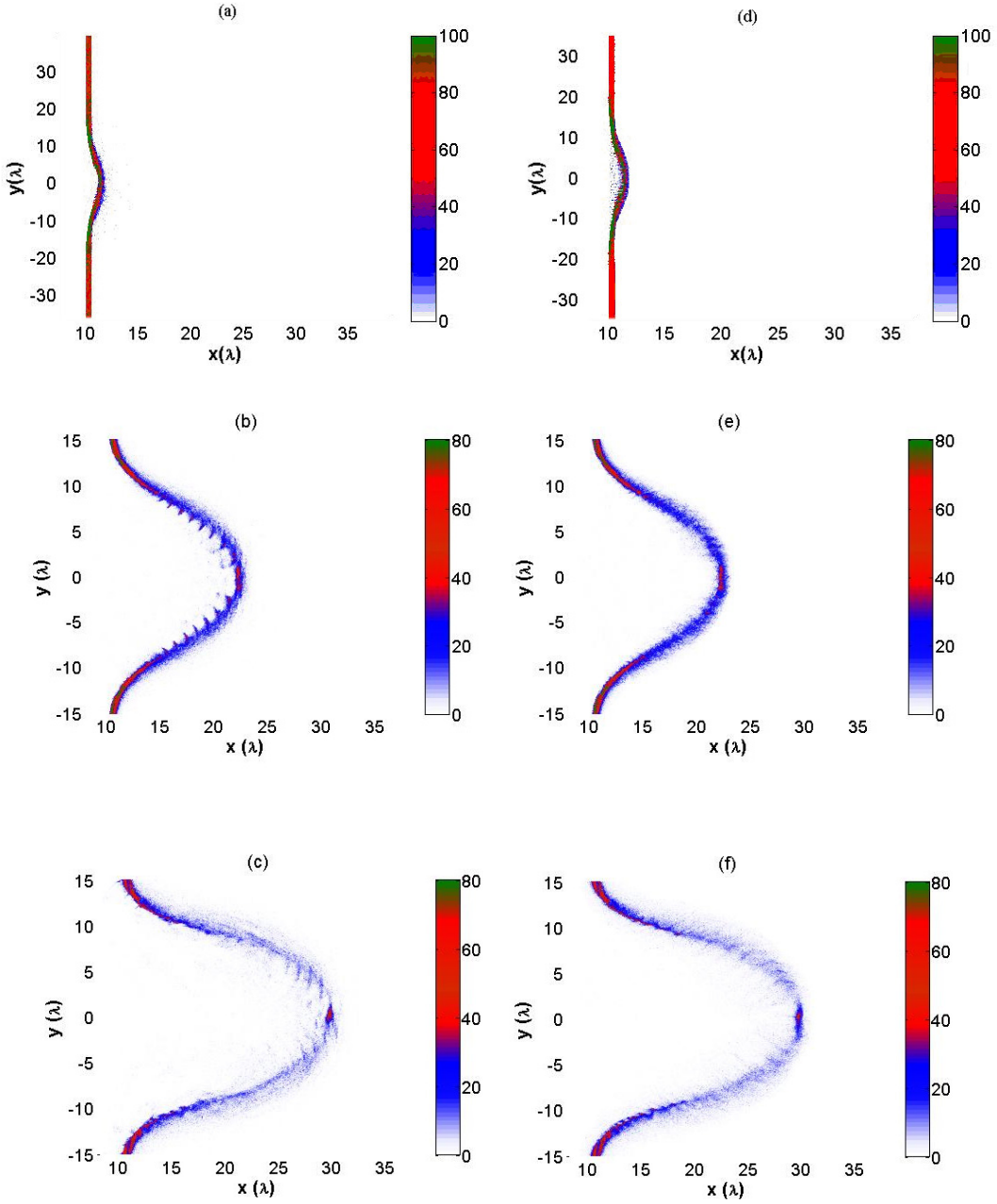

Fig. 4 (color online): Foil density evolution. Left: electrons, right: ions, at times (a,d) $t = 16$, (b,e) $t = 36$, (c,f) $t = 46$, in units of laser period. The laser pulse is incident from the left and hits the plasma at $t = 10$. Only half the transverse size of the simulation box is plotted in frames b, c, e, f for better resolution of fine structures.

In what is described below, the new configuration is self-organizing with small pieces of matter punched out of a plane foil. Here we exhibit this new regime in terms of two-dimensional particle-in-cell (2D-PIC) simulations.

In the simulations, we have taken a CP laser pulse with wavelength $\lambda = 1\mu\text{m}$ and maximum normalized vector potential $a = eA/mc^2 = 50$, corresponding to an intensity of

$I = 1.37 \times 10^{18}$ W/cm$^2 \cdot 2a^2/\lambda^2$. The pulse has a Gaussian radial profile with $2\sigma = 20\lambda$ full width at half maximum and a trapezoidal shape longitudinally with 20λ flat top and 1λ ramps on both sides. It is normally incident from the left on a uniform, fully ionized hydrogen foil of thickness $D = 0.5\lambda$ and normalized density $N = n_e / n_{crit} = 80$, where the electron density n_e is given in units of the critical density $n_{crit} = \pi m_e c^2 / \lambda^2$ and c is the velocity of light. Proton to electron mass ratio is $m_p / m_e = 1836$. The size of the simulation box is $50\lambda \times 80\lambda$ in (x,y) directions, respectively. A wide transverse margin (>3.5 σ) has been chosen to eliminate boundary effects. We take 100 particles per cell per species and a cell size of $\lambda/80$. The flat plasma foil is located at $x = 10\lambda$ initially. Periodic boundary conditions are used for particle and fields in transverse direction, and fields are absorbed at the boundaries in longitudinal direction.

The temporal evolution of the foil is shown in Fig. 1, separately for electron and ion density. One observes that electrons and ions move closely together. At $t = 16$ (in units of laser period), about 6 laser cycles after the pulse front has reached the plasma, the foil is slightly curved, following the transverse Gaussian profile of the laser pulse. At $t = 36$, a periodic structure having approximately 1 λ scale is seen, very prominently in the electron distribution, but also already imprinted in the ion distribution. Such surface rippling has been identified before in a number of numerical studies and has been described as a Rayleigh-Taylor-type instability (RTI) occurring in thin foils when driven by strong radiation pressure. Here we depict it when the foil is already strongly deformed. At this time, the laser light is reflected from the indented walls and creates an intense standing-wave pattern at the bottom of the crater (see Fig. 2a).

We attribute the foil rippling to this λ-period seed pattern, at least in part. A second source is a fast current instability, setting in at early times when the foil is still plane. It has been described in. Inspecting the longitudinal j_x current at time $t = 36$ in Fig. 2c, a periodic structure of current cells can be recognized, also with λ period. It indicates a pattern of forward and backward currents typical for Weibel instability, which is known to grow fast on the time-scale of the inverse plasma frequency ω_p^{-1}, which is shorter than the light period for solid density. These current patterns contribute to the unstable foil dynamics in the wing region.

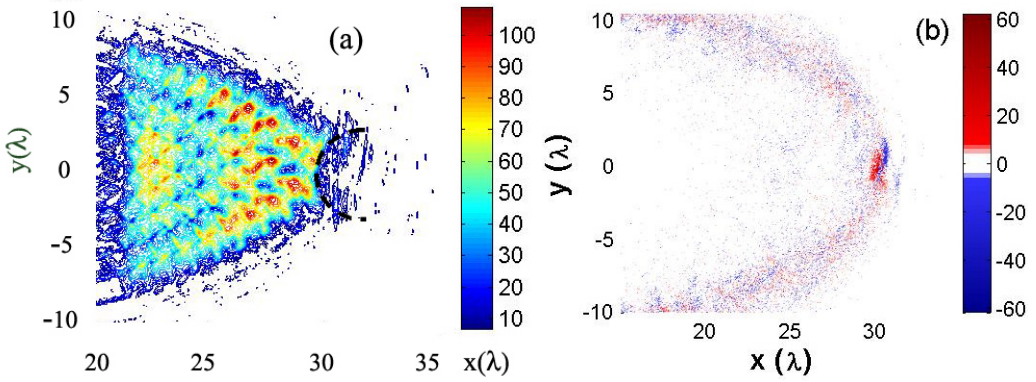

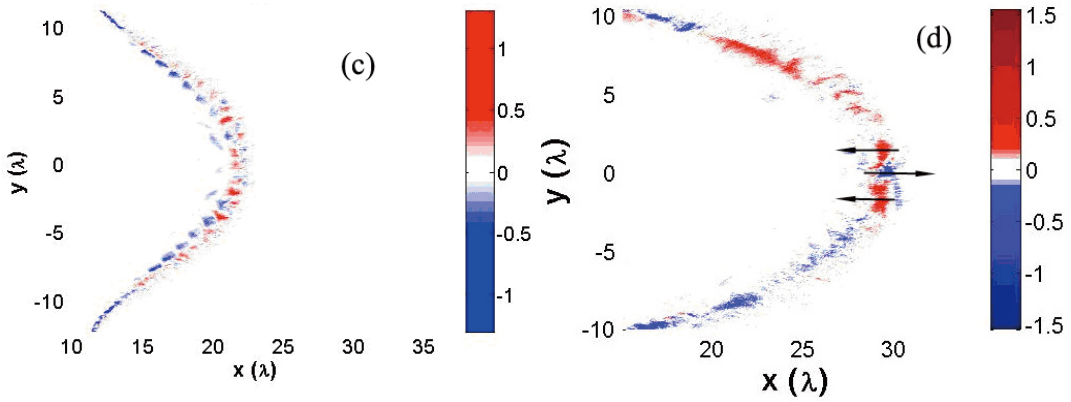

Fig.5 (color online) (a) laser field $\sqrt{E_y^2 + E_z^2}$ at $t = 46$, the dashed line marks the concave pulse front pushing the ion clump; (b) charge density distribution $(n_i - n_e)$ at $t = 46$; (c) current density at $t = 36$ (normalized by $en_e c$); (d) current density at $t = 46$. The black arrows in the clump region indicate the direction of electron motion.

Another important aspect is that the foil is strongly accelerated as a whole, and RTI depending on ion motion will add to perforate and break the foil. This is clearly seen in Figs. 1c and 1f, both for electrons and ions. Using the RTI growth rates derived in, we find e-folding within 6 laser cycles for the wing region which is consistent with the present simulation. The actual dynamics are very complicated, combining RTI and Weibel instabilities in the phase of nonlinear evolution. This is not yet understood in detail and needs separate investigation. As a result, the foil becomes transparent in the wing region, where then light starts to pass the foil and to overtake the dense clump located near the laser axis (see Fig. 2a).

Let us now describe the evolution of the central clump in more detail. From Figs. 1c and 1f we see that the transverse extension of the clump is about 2λ at $t = 46$. On these small scales, only a microscopic treatment as in a PIC simulation can describe the dynamics adequately. In Fig. 2a it indicates that the laser pulse enfolds the clump and tends to keep it together. Plotting charge density $(n_i - n_e)$ in Fig. 2b, one recognizes how electrons (blue) are running ahead dragging ions (red). Here the deviation from axial symmetry reflects the fact that the laser electric field is not axially symmetric, but rotates with the laser frequency. S. Rykovanov has documented the corresponding spiralling electron motion in movies.

The current cells, seen with λ-period at time $t = 36$ in Fig.5c, have almost been dissolved at time $t = 46$ in Fig.5d, except for the central cell on the laser axis which is stabilised by the local laser field. The black arrows in Fig.5d indicate the electron motion around the clump. Electrons move in laser direction on the axis and return on the side of the clump. The central plasma current generates at $|y| = \lambda$ a magnetic field of more than a MegaGauss that is able to stabilize the clump by magnetic compression. Unfortunately, we did not succeed to resolve this B-field separately because of the strong laser field superimposed.

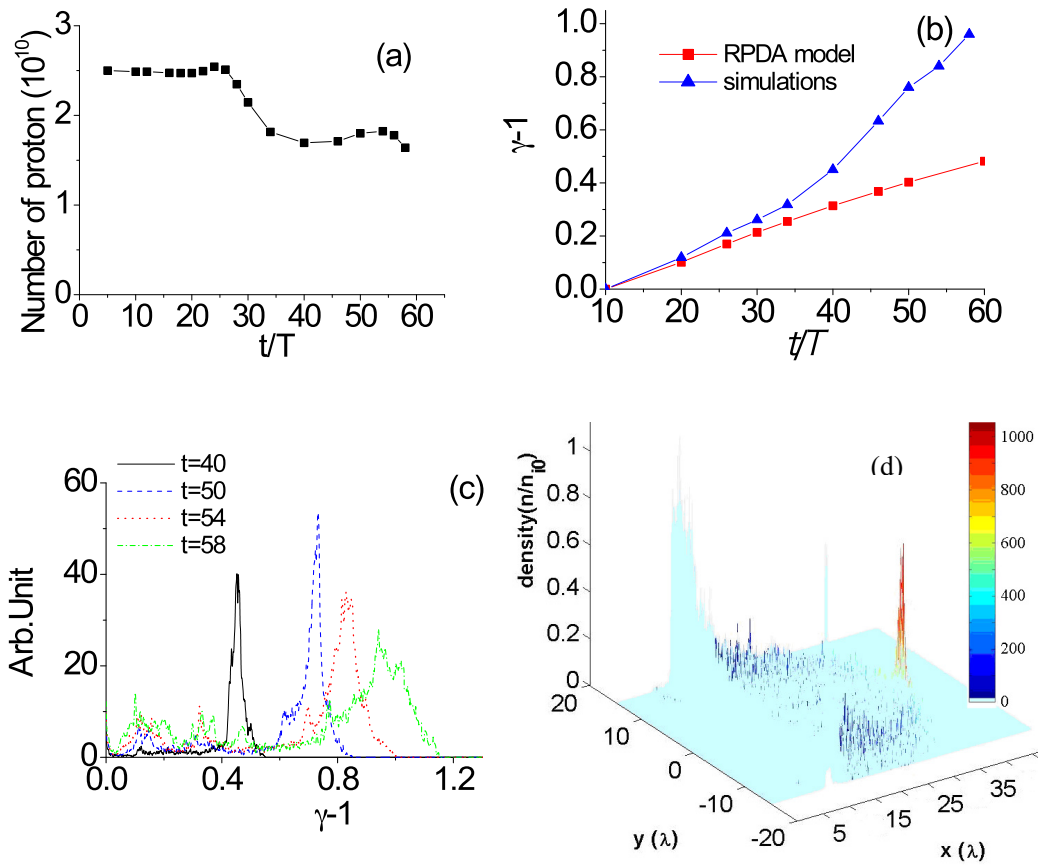

Fig.6 (color online) (a) Number of protons in the center of the foil ($r \le \lambda$) versus time in units of laser cycles; (b) proton energy; (c) evolution of energy spectrum for beam ions located inside the central clump ($r \le \lambda$); (d) density and energy distributions of protons at $t = 58$ (the colour bar gives ion energy in MeV).

Figure 6 highlights the central results concerning clump evolution. The total number of protons, located within a λ distance from the laser axis, is shown in Fig. 6a. Due to transverse expansion, it drops from an initial value of 2.5×10^{10} after time $t = 26$, but this trend is interrupted at about $t = 35$, when the foil becomes transparent in the wing region and the new regime of quasi-stable acceleration sets in. In the present 2D-PIC simulation, about 1.7×10^{10} protons (1 nano-Coulomb) are trapped in the central clump and are accelerated to an ion energy of approximately 1 GeV, as it is seen in Fig. 3a. An enhanced acceleration mode sets in at t=35 after clump formation. Corresponding proton energies shown in Fig. 6b exceed the predictions of the Radiation Pressure Driven Acceleration (RPDA) by a factor 2. At the same time, the ion energy spectra start to exhibit sharp peaks, as it is seen in Fig. 6c. The perspective view in Fig. 3d then shows ion density in the (x, y) plane with colour marking ion energy. One observes the high-density region of the unperturbed foil at the boundaries, the low-density plasma remains of the foil in the wing region (dark blue), and the accelerated ion clump sticking out as a conspicuous red spike in the centre.

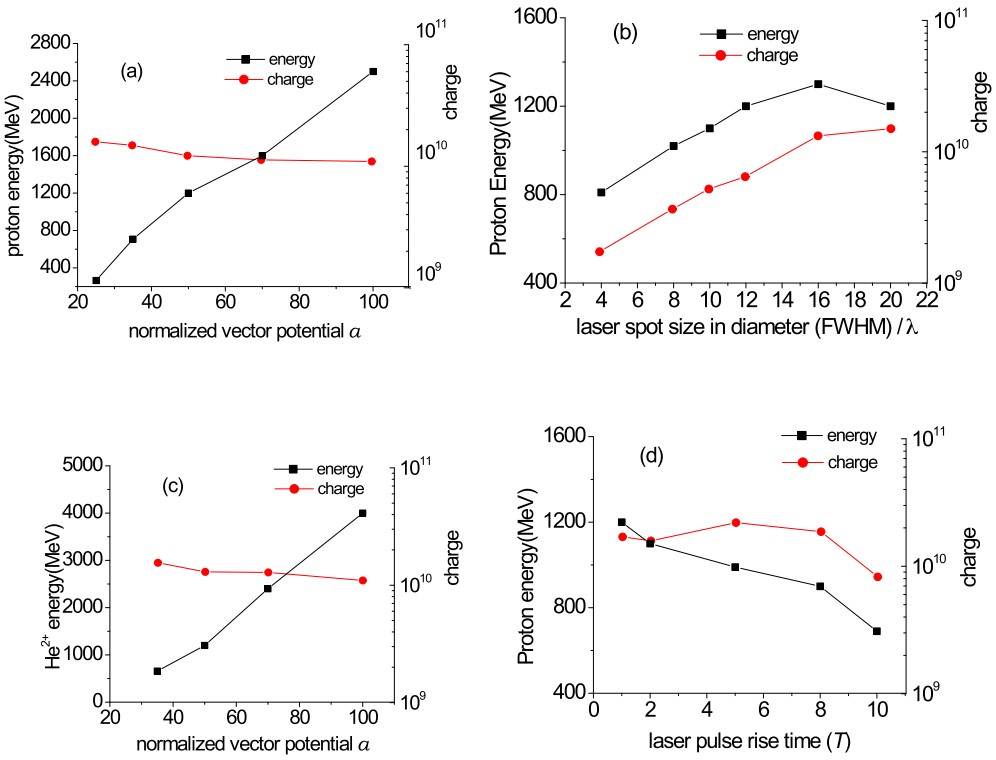

Fig.7 Scaling studies (scan a parameter and all other parameters are fixed) (a) scaling the proton energy/charge with the normalized vector potential *a*; (b) Proton energy/charge with the laser spot size; (c) scaling the helium energy/charge with *a*; (d) Proton energy/charge with the rise time in unit of laser cycles.

We have varied single parameters, keeping the others constant, to check the robustness of the present results. In Fig. 7a one observes that proton energy is rising almost linearly with laser amplitude a, while charge remains nearly constant. In Fig. 7c the same plot is shown for He^{2+} ions instead of protons. Fig. 7b exhibits energy and charge as a function of laser spot size. Most important is Fig. 7d showing the dependence on rise time of the laser pulse. Increasing the front ramp from 1 to 10 laser cycles leaves the beam charge almost invariant while proton energy falls from 1.2 GeV to 0.7 GeV. Though high contrast over 10 laser cycles is very challenging, it may be possible to be achieved. Much progress has been made recently in generating laser pulses with ultra-high contrast.

The RPA is promising for laser driven ion acceleration. When the PSA condition $a_L \sim (n_0 / n_c) D / \lambda_L$ is satisfied, the protons are synchronously accelerated and bunched like that in a radio frequency accelerator, therefore high current and mono-energetic proton beams can be generated with a high energy conversion efficiency of laser-to-ions, alike conventional accelerators. With state of art laser technology, the optimum target for ion acceleration is about nanometer thick (5nm~100nm). In multi-dimensional case, ion acceleration terminates due to transverse expansion of the accelerated ion bunch and transverse instabilities. In particular, instabilities grow in the wings of the indented foil, where light is obliquely incident and strong electron heating sets in. Eventually, this part of the foil is diluted and becomes transparent to the driving laser light**.** The central new observation in the present paper is that this process of foil

dispersion may stop before reaching the centre of the focal spot and that a relatively stable ion clump forms near the laser axis which is efficiently accelerated. The stabilization is related to the driving laser pulse that has passed the dispersed foil in the transparent wing region and starts to encompass the opaque clump, keeping it together. This leads to sharply peaked proton spectra with energies of 1 GeV and more. The scaling studies demonstrate that the self-focusing mechanism is robust not only for hydrogen plasma, but also for heavier ion species. These findings, obtained on the basis of multi-dimensional PIC simulations, go beyond results on phase stable acceleration published so far. An important point is that the nonlinear physics itself selects the amount of accelerated ions (about 1 nano-Coulomb of protons in the present simulations), rather than relying on complicated target structures. This opens an option to use simple targets adequate for high-repetition rates by means of plane foils. This is attractive for applications.

Laser-driven proton generation with a thin-foil target

A. Sagisaka[1], A. S. Pirozhkov[1], M. Mori[1], A. Yogo[1], K. Ogura[1], S. Orimo[1], M. Nishiuchi[1], J. Ma[1], H. Kiriyama[1], S. Kanazawa[1], S. Kondo[1], Y. Nakai[1], T. Shimomura[1], M. Tanoue[1], A. Akutsu[1], H. Okada[1], T. Motomura[1], H. Daido[1], K. Kondo[1], S. V. Bulanov[1,2], T. Zh. Esirkepov[1], H. Nagatomo[3], Y. Oishi[4], K. Nemoto[4], I. W. Choi[5], S. K. Lee[5], and J. Lee[5]

[1] *Advanced Photon Research Center and Photo-Medical Research Center, Japan Atomic Energy Agency, 8-1-7 Umemidai, Kizugawa-city, Kyoto 619-0215, Japan*
[2] *A. M. Prokhorov Institute of General Physics of the Russian Academy of Sciences, 38 Vavilov Street, 119991 Moscow, Russia*
[3] *Institute of Laser Engineering, Osaka University, 2-6 Yamadaoka Suita, Osaka 565-0871, Japan*
[4] *Central Research Institute of Electric Power Industry, 2-6-1 Nagasaka, Yokosuka, Kanagawa 240-0196, Japan*
[5] *Advanced Photonics Research Institute, GIST, 261 Cheomdan-gwagiro, Buk-gu, Gwangju 500-712, Republic of Korea*

Abstract

We observe proton signals in the laser-plasma interaction by using a thin-foil target. To get higher energy protons the size of the preformed plasma is reduced by changing the laser contrast level. In the high-contrast laser pulse case the maximum energy of the protons generated at rear side of the target increases.

1. Introduction

High-intensity laser and plasma interactions produce intense high-energy particles, hard x-ray, and terahertz (THz) radiation [1-6]. High-energy protons have been observed at the rear side of the thin-foil target [2]. A preformed plasma made by a prepulse is one of the important parameters in optimizing the generation of high-energy protons [7-10]. Kaluza et al. have reported that the optimal parameters of proton acceleration depend on the preformed plasma condition [9]. Neely et al. have observed high energy protons [11] with thin-foil targets with thickness of << 1 μm. They have used a plasma mirror to reduce the preformed plasma.

In this experiment, we observed the high-energy proton by using a thin-foil target. The size of preformed plasma is reduced by changing the laser contrast level to get higher energy proton. In the high-contrast laser pulse case the maximum energy of proton generated at rear side of the target along the target normal direction increased.

2. Experimental setup

We use a Ti:sapphire laser system (J-KAREN) at JAEA [12,13]. The laser pulse duration is ~30 fs [full width at half maximum (FWHM)]. The ASE level is greatly suppressed by using an OPCPA preamplifier in a double CPA Ti:sapphire laser system [13]. The contrast level of ASE is controlled by inserting a saturable absorber (SA) in the laser system [13,14]. Figure 1 shows the schematic view of the experimental setup. A p-polarized

laser beam is focused by an off-axis parabolic mirror with a focal length of f = 152.4 mm and an incidence angle of 45˚. The spot size of the focused laser beam is 4 μm (FWHM) x 3 μm (FWHM). It contains the ~64 % of energy within $1/e^2$ from the profile of the focusing pattern. The estimated peak intensity is up to 10^{20} W/cm^2. A tape target driver provides a fresh surface of the thin foil target. The probe beam passes through the optical delay line. A linear translation stage is used to vary the delay between the pump and probe beams. The plasma image is magnified by a factor of ~10 and detected by the CCD camera. The intensity of the probe beam is attenuated by neutral density filters so as to fall within the dynamic range of the camera. A narrow-band interference filter is placed in front of the CCD cameras to reject unwanted emission from the plasma. The interferogram is obtained from a Fresnel biprism using a hundred femtosecond probe pulse at the time of ~50 ps before the pump beam [15]. The protons are observed with a time-of-flight (TOF) ion energy analyzer [16,17]. The protons produced by the intense laser are measured in the direction normal to the target. The TOF proton measurement gives an information of proton energy distribution.

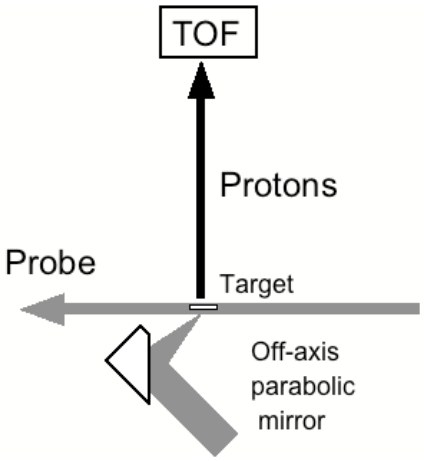

Fig.1 Experimental setup

3. Experimental results

Figure 2 shows the proton energy distributions obtained by TOF. The solid line shows the case of low contrast level. The contrast level of ASE is less than 10^{-6} (without SA). The ASE duration is ~1.2 ns before the main pulse by controlling a fast pockels cell timing in the laser system [18]. In this condition the preformed plasma at the front side is generated with the 7.5 μm thick polyimide target. To get the higher protons, we change the contrast level of ASE. The SA inserted in the laser system efficiently reduces the ASE. In the case of high contrast, the ASE level is less than 10^{-10}. In this case, the fast pockels cell is turned off. The preformed plasma is not detectable. This means it is smaller than approximately ~30 μm. The higher laser pulse contrast is confirmed with the on-target contrast diagnostic [19] based on the target reflectivity measurement. The dotted line in Fig. 2 shows the proton spectra at the target normal direction. The maximum proton energy increases. High-contrast laser pulse is attractive to irradiate very thin target (<1 μm) to achieve higher proton energy and useful for the transport and focus the proton beam [20].

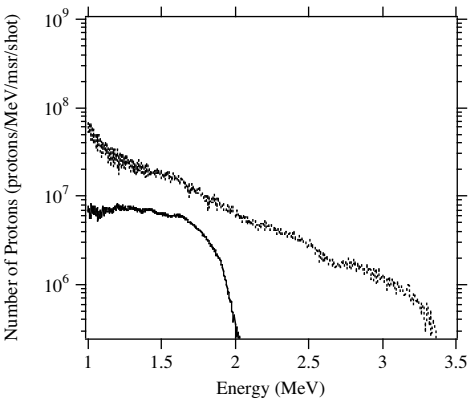

Fig.2 Energy distribution of protons

4. Summary

The high-energy protons are observed by using a thin-foil target. To get higher energy protons the size of the preformed plasma is reduced by changing the laser contrast level. In the high-contrast case the maximum energy of proton generated at rear side of the target by

reducing the size of preformed plasma. The high-contrast laser pulse is attractive to irradiate very thin target to achieve higher proton energy.

Acknowledgments

We would like to thank Dr. S. Kawanishi, for his support, suggestions, and useful discussions. This work is partly supported by the Special Coordination Fund (SCF) for Promoting Science and Technology commissioned by the Ministry of Education, Culture, Sports, Science and Technology (MEXT) of Japan. This work was partly performed under the joint project between ILE, Osaka Univ. and Advanced Photon Research Center, JAEA on "Mono-energetic quantum beam science with PW lasers" commissioned by MEXT (Japan Ministry of Education, Culture, Sports, Science, and Technology). This work was partially supported by the JSPS-CAS Core-University Program in the field of Laser Plasma and High Energy Density Physics.

References

[1] H. Daido, A. Sagisaka, K. Ogura, S. Orimo, M. Nishiuchi, A. Yogo, M. Mori, Z. Li, H. Kiriyama, S. Kanazawa, A. Akutsu, Y. Nakai, A. Piroshkov, S. Bulanov, T. Esirkepov, T. Kimura, T. Tajima, K. Nemoto, Y. Oishi, T. Nayuki, T. Fujii, A. Zhidkov, A. Noda, S. Nakamura, I. W. Choi, T. J. Yu, J. H. Sung, H. T. Kim, T. M. Jeong, K. -H. Hong, J. -H. Kim, Y. -C. Noh, D. -K. Ko, J. Lee, S. Nashima, K. Shimizu, and M. Hosoda, X-ray lasers 2006, Springer, **115**, 595 (2007).

[2] M. Borghesi, J. Fuchs, S. V. Bulanov, A. J. Mackinnon, P. K. Patel, and M. Roth, Fusion Sci. Technol. **49**, 412 (2006).

[3] M. I. K. Santala, M. Zepf, I. Watts, F. N. Beg, E. Clark, M. Tatarakis, K. krushelnick, A. E. Dangor, T. McCanny, I. Spencer, R. P. Singhal, K. W. D. Ledingham, S. C. Wilks, A. C. Machacek, J. S. Wark, R. Allott, R. J. Clarke, and P. A. Norreys, Phys. Rev. Lett. **84**, 1459 (2000).

[4] S. Bastiani, A. Rousse, J. P. Geindre, P. Audebert, C. Quoix, G. Hamoniaux, A. Antonetti, and J. -C. Gauthier, Phys. Rev. E **56**, 7179 (1997).

[5] H. Hamster, A. Sullivan, S. Gordon, W. White, and R. W. Falcone, Phys. Rev. Lett. **71**, 2725 (1993).

[6] H. Hamster, A. Sullivan, S. Gordon, and R. W. Falcone, Phys. Rev. E **49**, 671 (1994).

[7] A. J. Mackinnon, M. Borghesi, S. Hatchett, M. H. Key, P. K. Patel, H. Campbell, A. Schiavi, R. Snavely, S. C. Wilks, and O. Willi, Phys. Rev. Lett. **86**, 1769 (2001).

[8] M. Roth, A. Blazevic, M. Geissel, T. Schlegel, T. E. Cowan, M. Allen, J. -C. Gauthier, P. Audebert, J. Fuchs, J. Meyer-ter-Vehn, M. Hegelich, S. Karsch, and A. Pukhov, Phys. Rev. ST Accel. Beams **5**, 061301 (2002).

[9] M. Kaluza, J. Schreiber, M. I. K. Santala, G. D. Tsakiris, K. Eidmann, J. Meyer-ter-Vehn, and K. J. Witte, Phys. Rev. Lett. **93**, 045003 (2004).

[10] F. Lindau, O. Lundh, A. Persson, P. McKenna, K. Osvay, D. Batani, and C. -G. Wahlström, Phys. Rev. Lett. **95**, 175002 (2005).

[11] D. Neely, P. Foster, A. Robinson, F. Lindau, O. Lundh, A. Persson, C. -G. Wahlstrom, and P. McKenna, Appl. Phys. Lett. **89**, 021502 (2006).

[12] H. Kiriyama, M. Mori, Y. Nakai, T. Shimomura, M. Tanoue, A. Akutsu, S. Kondo, S. Kanazawa, H. Okada, T. Motomura, H. Daido, T. Kimura, and T. Tajima, Opt. Lett. **33**, 645 (2008).

[13] H. Kiriyama, M. Mori, Y. Nakai, T. Shimomura, M. Tanoue, A. Akutsu, H. Okada, T. Motomura, S. Kondo, S. Kanazawa, A. Sagisaka, J. Ma, I. Daito, H. Kotaki, H. Daido, S. Bulanov, T. Kimura, and T. Tajima, Opt. Commun. **282**, 625 (2009).

[14] A. S. Pirozhkov, M. Mori, A. Yogo, H. Kiriyama, K. Ogura, A. Sagisaka, J.-L. Ma, S. Orimo, M. Nishiuchi, and H. Sugiyama, Proc. SPIE **7354**, 735414 (2009).
[15] A. Sagisaka, A. S. Pirozhkov, H. Daido, A. Fukumi, Z. Li, K. Ogura, A. Yogo, Y. Oishi, T. Nayuki, T. Fujii, K. Nemoto, S. Orimo, M. Nishiuchi, Y. Hayashi, M. Mori, M. Kado, S. Nakamura, A. Noda, I. W. Choi, J. H. Sung, D.-K. Ko, and J. Lee, Appl. Phys. B **84**, 415 (2006).
[16] S. Nakamura, Y. Iwashita, A. Noda, T. Shirai, H. Tongu, A. Fukumi, M. Kado, A. Yogo, M. Mori, S. Orimo, K. Ogura, A. Sagisaka, M. Nishiuchi, Y. Hayashi, Z. Li, H. Daido, and Y. Wada, Jpn. J. Appl. Phys. **45**, L913 (2006).
[17] A. Yogo, H. Daido, A. Fukumi, Z. Li, K. Ogura, A. Sagisaka, A. S. Pirozhkov, S. Nakamura, Y. Iwashita, T. Shirai, A. Noda, Y. Oishi, T. Nayuki, T. Fujii, K. Nemoto, I. W. Choi, J. H. Sung, D.-K. Ko, J. Lee, M. Kaneda, and A. Itoh, Phys. Plasmas **14**, 043104 (2007).
[18] M. Mori, A. Yogo, H. Kiriyama, M. Nishiuchi, K. Ogura, S. Orimo, J. Ma, A. Sagisaka, S. Kanazawa, S. Kondo, Y. Nakai, Y. Akutsu, Y. Yamamoto, T. Shimomura, M. Tanoue, S. Nakamura, T. Shirai, Y. Iwashita, A. Noda, Y. Oishi, T. Nayuki, T. Fujii, K. Nemoto, I. W. Choi, T. J. Yu, D. -K. Ko, J. Lee, H. Daido, T. Zh. Esirkepov, S. V. Bulanov, P. R. Bolton, and T. Kimura, IEEE trans. plasma sci. **36**, 1872 (2008).
[19] A. S. Pirozhkov, I. W. Choi, J. H. Sung, S. K. Lee, T. J. Yu, T. M. Jeong, I J. Kim, N. Hafz, C. M. Kim, K. H. Pae, Y.-C. Noh, D.-K. Ko, J. Lee, A. P. L. Robinson, P. Foster, S. Hawkes, M. Streeter, C. Spindloe, P. McKenna, D. C. Carroll, C.-G. Wahlström, M. Zepf, D. Adams, B. Dromey, K. Markey, S. Kar, Y. T. Li, M. H. Xu, H. Nagatomo, M. Mori, A. Yogo, H. Kiriyama, K. Ogura, A. Sagisaka, S. Orimo, M. Nishiuchi, H. Sugiyama, T. Zh. Esirkepov, H. Okada, S. Kondo, S. Kanazawa, Y. Nakai, A. Akutsu, T. Motomura, M. Tanoue, T. Shimomura, M. Ikegami, I. Daito, M. Kando, T. Kameshima, P. Bolton, S. V. Bulanov, H. Daido, and D. Neely, Appl. Phys. Lett. **94**, 241102 (2009).
[20] M. Nishiuchi, I. Daito, M. Ikegami, H. Daido, M. Mori, S. Orimo, K. Ogura, A. Sagisaka, A. Yogo, A. S. Pirozhkov, H. Sugiyama, H. Kiriyama, H. Okada, S. Kanazawa, S. Kondo, T. Shimomura, M. Tanoue, Y. Nakai, H. Sasao, D. Wakai, H. Sakaki, P. Bolton, I. W. Choi, J. H. Sung, J. Lee, Y. Oishi, T. Fujii, K. Nemoto, H. Souda, A. Noda, Y. Iseki, and T. Yoshiyuki, Appl. Phys. Lett. **94**, 061107 (2009).

Pre-plasma formation and its reduction

Atsushi Sunahara
(Institute for Laser Technology)
2-6 Yamadaoka Suita Osaka Japan 565-0871

T. Johzaki, H. Nagatomo, and K. Mima
(Institute of Laser Engineering, Osaka University)
2-6 Yamadaoka Suita Osaka Japan 565-0871

Abstract:
In order to achieve high energy coupling between ultra-intense laser to the imploded core plasma in the fast-ignition scheme, effects of pre-formed plasma on it has been investigated by 1D and 2D radiation hydrodynamic simulations. In the 2009 FIREX experiment, the energy of the pre-pulse was estimated to be 130mJ, which is large enough to significantly reduce the energy coupling. In order to reduce pre-plasma formation, we propose two approaches, that is uses of thin film and a pointed cone tip, are proposed to decrease the pre-plasma formation inside the cone.

The fast ignition scheme of inertial confinement fusion is an attractive way to igniting thermonuclear burn. In this scheme the fast electron flow generated by ultra-high intensity laser is used for heating a compressed core and ignite it. First, a cone shell attached to the fuel capsule implodes. Subsequently, the imploded core achieves a high areal density enough to stop the electron flow, and the ultra-intense laser irradiates the cone tip, generating a fast electron flow. The fast electron flow gives the compressed core its kinetic energy as a thermal one, and heats it to the temperature that ignites the thermonuclear burn. This scheme has the potential advantage of being able to ignite using small laser energy compared to the conventional central ignition scheme.

However, in order to achieve the high-gain of the thermonuclear burn, we have to increase the energy coupling efficiency between the ultra-intense laser and the compressed core. Kodama et al. (2001) [1] conducted the first experiment on this fast ignition in 2000. They found the increase of the neutron yield from the highly dense core plasma heated by the ultra-intense laser. Their experimental result attracted attention to the fast ignition scheme by many researchers. Then for carrying out fast ignition experiments, an ultra-high intensity laser (LFEX) was

constructed at Osaka University, and in University of Rochester, the OMGA-EP laser system was constructed. Osaka University started the fast ignition realization experiment (FIREX). This project has two phases. In FIREX-I, the goal is to achieve the ignition temperature of 5 keV by heating with ultra-intense laser. In FIREX-II, we proceed to achieve high gain thermonuclear burn.

Unfortunately, we have not achieved a significant increase of the neutron yield after the first experiment by Kodama et al. One reason for this is the pre-formed plasma formation inside the cone. Cone is used to prevent the interaction region from being filled with implosion plasma. However, pre-plasma is generated inside the cone, and the interaction of ultra-high intense laser with the cone tip is disturbed. Baton et al. (2008) [2] pointed out that pre formed plasma inside the cone significantly lowers the coupling efficiency between the ultra high intensity laser and the core. Cai et al. (2010) [3] pointed out that existence of the pre-formed plasma inside the cone reduces creation of fast electrons of the energy less than 5 MeV. These electrons are the dominant contributor to heating of the core plasma. Johzaki et al. (2010) [4] simulated generation of fast electrons by ultra-intense laser, and investigated effects of the pre-formed plasma on coupling between the laser and the core. They compared two cases, i.e. 1micron and 10 micron scale pre-formed plasma, to study effects of pre-formed plasma on generation of these electrons, and found that 10 micron scale pre-formed plasma lowered the coupling efficiency by a factor of ~20 %. Therefore, we concluded that 1 micron-scale pre-formed plasma is preferable in gaining a high coupling efficiency. The author of this paper investigated the pre-formed plasma formation in various pre-pulse conditions, using 1D radiation hydrodynamic simulations, and showed that 1micron scale pre-formed plasma is obtainable using the laser of 1E10W/cm2 and 1ns duration, Sunahara et al. (2010) [5]. The author of this paper also found that when laser of 1E11W/cm2 and 1ns duration is used, the density gradient scale length of pre-formed plasma could be 7 microns.

In 2009, we at Osaka University conducted the first FIREX integrated experiment using a beam of LFEX laser. The author of this paper compared results of 2D radiation hydrodynamic simulations with the experimentally observed plasma formation on the plate target irradiated by the pre-pulse of the LFEX laser. The comparison showed that in this experiment a pre-pulse of 1E13W/cm2 and 1ns duration was present before the main pulse of LFEX laser. With 1E13W/cm2 and 1ns pre-pulse, the 2D radiation hydrodynamic simulations yielded the density gradient scale length of 100 microns, located at the 150 micron away from the target surface shown in Fig.1. Also, the blow off speed of the plasma was 1E7cm/s, in agreement with experimental observations.

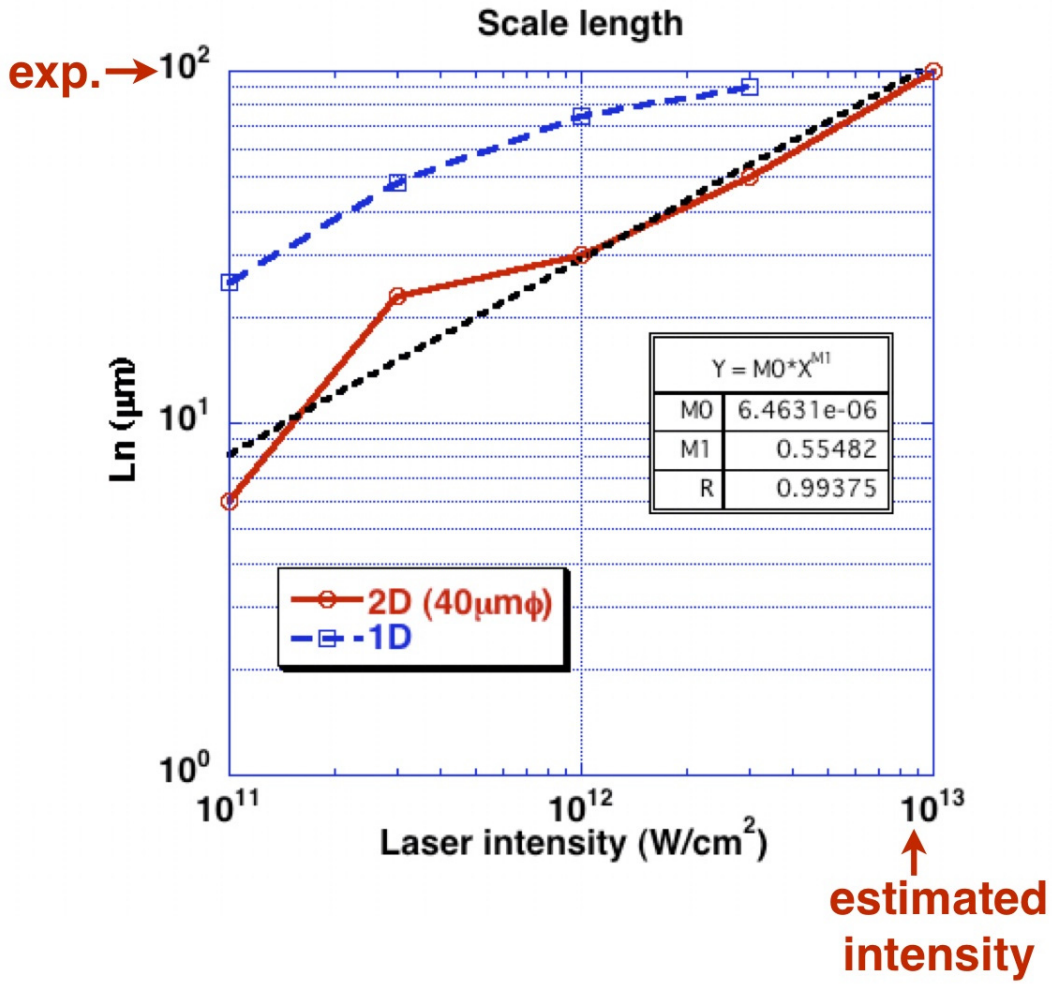

Fig.1 Calculated density scale length. Experimentally observed 100 μ m scale corresponds to 10^{13}W/cm^2 laser intensity.

The author of this paper also simulated the pre-plasma formation inside the cone shown in Fig.2. Using the pre-pulse of 1E13W/cm2, 1ns duration and 45 degree open angle, the density scale length of the pre-formed plasma ranged in 37 - 60 microns when the density was varied between the critical density to 1/3 of the critical density. With this 37-60 micron scale pre-formed plasma, the interaction of the ultra-intense laser occurs not at the tip surface of the cone but at the pre-formed plasma that has a relatively low density and long scale, and the kinetic energy of the fast electrons generated by this interaction of the ultra-high intense laser is beyond

the right range for heating the core plasma and decreases the energy coupling efficiency of the ultra-high intense laser.

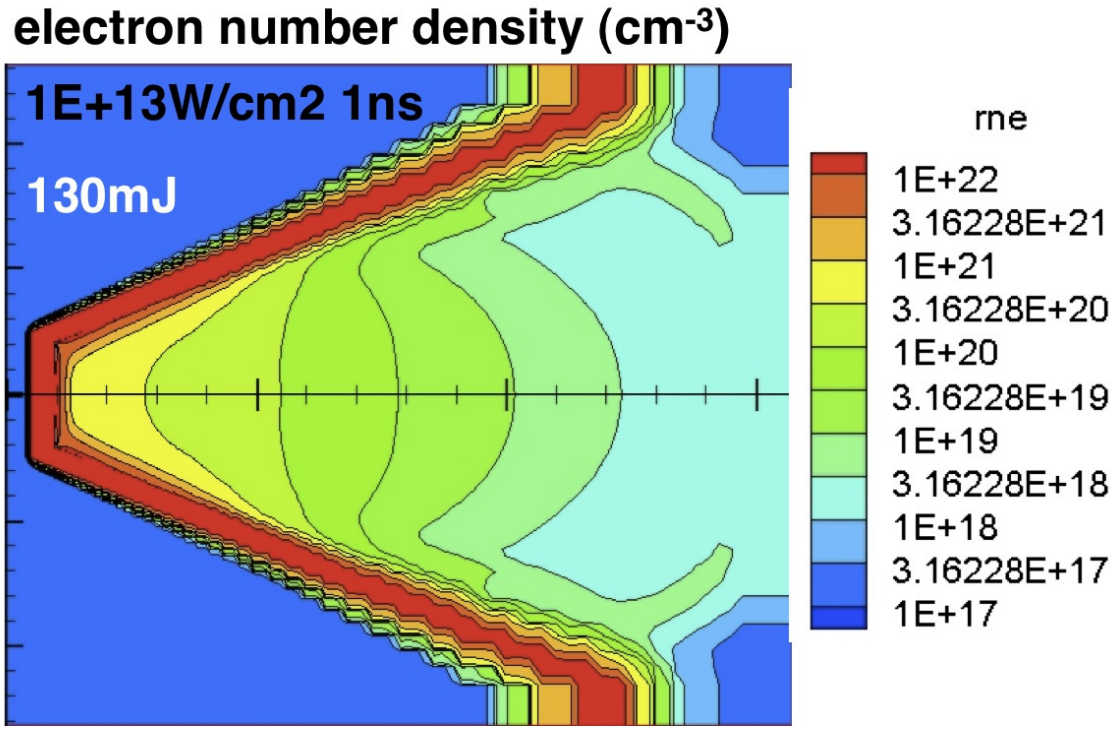

Fig. 2 Calculated electron number density with 10^{13}W/cm^2 and 1ns pulse for 45deg open angle cone.

In the 2009 experiment, the neutron yield increased almost 10 folds using this heating, compared to that without heating. However, the energy coupling efficiency was estimated to be 3-5%, considerably lower than 15-20% found in the earlier experiment by Kodama et al. Therefore, we conjectured that pre-plasma formation was lowering the energy coupling, and we need to reduce the pre-pulse level to at least 1E10 W/cm2 and 1ns (0.13 mJ), when the spot diameter is 40 microns for obtaining 1micron scale pre-formed plasma.

For the purpose of reducing the pre-plasma formation inside the core, the author of this paper proposes two approaches shown in Fig.3. One is to use a thin film as the saturable absorber of the pre-pulse. 2D simulation was done on the CH film with 0.1micron thickness irradiated by the pre-pulse of 3E11 W/cm2 intensity and a flat top temporal profile. The simulations shows that it takes 1ns for expanding the CH film to the below critical density of 1 micron wavelength laser.

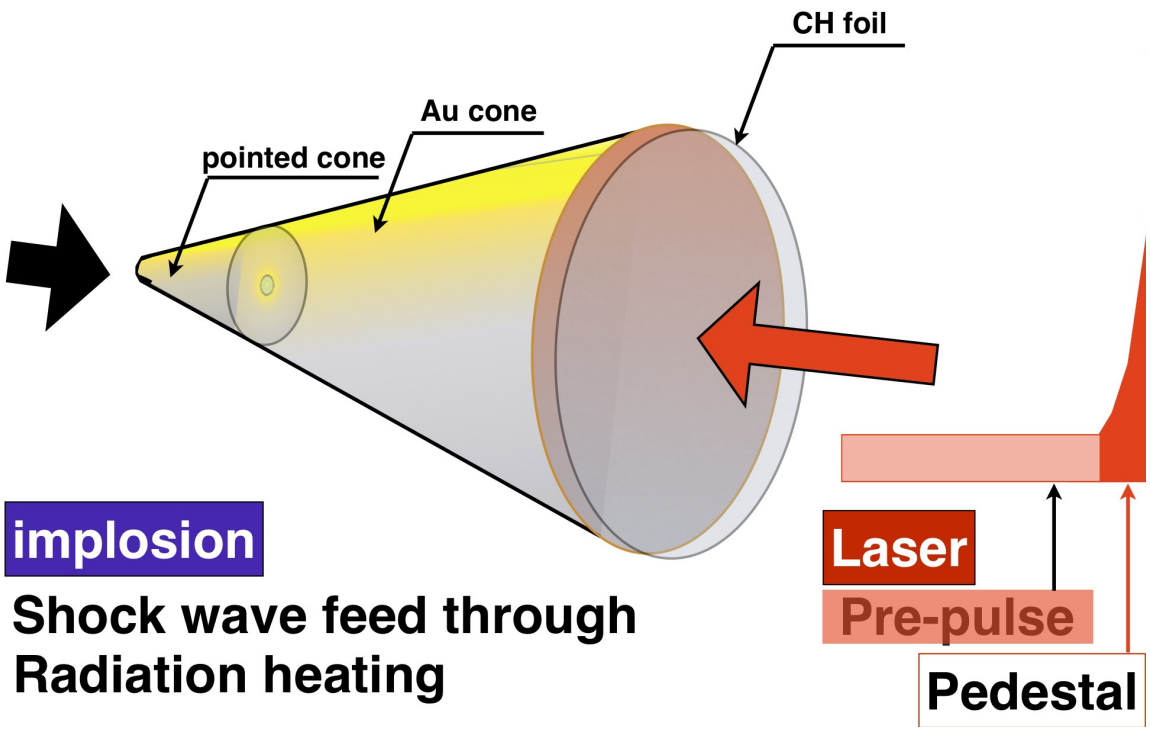

Fig.3 Schematic of reduction of pre-plasma formation.

Then, further expansion takes ~ 1ns before the plasma expands so that 80% of 1 micron wavelength light can penetrate into the plasma. Also, choosing an appropriate film thickness is crucial. For the quantitative analysis of proper film thickness, we investigated the mass ablation rate in a CH film[6], to find a scaling law similar to that given in the Fabbro et al. (1982) [7]. This enabled us to find an appropriate thickness of CH film, depending on the pre-pulse level.

The second approach is to use a pointed cone tip in order to prevent the shock break through from the imploded core to the interior of the cone.
The shock break through from outside of the cone to interior of it also can generate the pre-formed plasma. When heavier material such as aluminum is used for pointed cone tip, timing of the shock breaking through the cone tip can take the duration time order of 10 ps. By further optimization of the pointed tip, we will be able to design a fast ignition target, where ultra-intense laser irradiates a clean tip without forming the pre-plasma caused by the shock break through from the implosion plasma.

In summary, it was shown that the pre-plasma formation should be reduced for obtaining a high energy coupling efficiency in the fast ignition scheme. In the 2009 FIREX experiment, the energy of the pre-pulse was estimated to be 130mJ, which is large enough to significantly reduce the energy coupling. In order to achieve pre-plasma of 1 micron-scale length, the energy of the pre-plasma must be reduced to the 0.1 mJ level. Two approaches, uses of thin film and a pointed cone tip, are proposed to decrease the pre-plasma formation inside the cone, and further optimization of these approaches by simulation must be carried out.

Acknowledgements

This work was partially supported by the JSPS-CAS Core-University Program in the field of Laser Plasma and High Energy Density Physics.

References

[1] R. Kodama, P. A. Norreys, K. Mima, A. E. Dangor, R. G. Evans, H. Fujita, Y. Kitagawa, K. Krushelnick, T. Miyakoshi, N. Miyanaga, T. Norimatsu, S. J. Rose, T. Shozaki, K. Shigemori, A. Sunahara, M. Tampo, K. A. Tanaka, Y. Toyama, T. Yamanaka, and M. Zepf, “Fast heating of ultrahigh-density plasma as a step towards laser fusion ignition”, Nature 412, 798 (2001).
[2] S. D. Baton, M. Koenig, J. Fuchs, A. Benuzzi-Mounaix, P. Guillou, B. Loupias, T. Vinci, L. Gremillet, C. Rousseaux, M. Drouin, E. Lefebvre, F. Dorchies, C. Fourment, J. J. Santos, D. Batani, A. Morace, R. Redaelli, M. Nakatsutsumi, R. Kodama, A. Nishida, N. Ozaki, T. Norimatsu, Y. Aglitskiy, S. Atzeni, and A. Schiavi, “Inhibition of fast electron energy deposition due to preplasma filling of cone-attached targets”, Phys. Plasmas 15, 042706 (2008).
[3] H. B. Cai, K. Mima, A. Sunahara, T. Johzaki, H. Nagatomo, S. Zhu and X. T. He, “Prepulse effects on the generation of high energy electrons in fast ignition scheme”, Phys. Plasmas,17, 023106 (2010).
[4] T. Johzaki, et al.,"Core Heating Scaling for Fast Ignition Experiment FIREX-I", Proc. of 23rd IAEA Fusion Energy Conference, (Daejob, Korea, Oct. 2010).
[5] A. Sunahara and K. A. Tanaka, “Atomic number Z dependence of dynamics of laser-ablated materials”, Fusion Engineering and Design, 85, 935 (2010).
[6] K. Kinoshita et al., Appl. Phys. Lett. 84, 4623 (2004).
[7] R. Fabbro, E. Fabre, F. Amiranoff, C. Garban-Labaune, J. Virmont, and M. Weinfeld and C. E. Max, “Laser-wavelength dependence of mass-ablation rate and heat-flux inhibition in laser-produced plasmas”, Phys. Rev. A 26, 2289 (1982).

Numerical Simulations of Inertial Confinement Fusion Hohlraum with LARED-Integration Code

Jinghong Li*, Shuanggui Li, Chuanlei Zhai, Qinghong Zeng, Rong Yang,
Aiqing Zhang, Hong Guo, Juan Cheng, Xudeng Hang, Heng Yong, Jing Qi,
Peijun Gu, Wudi Zheng, Wenbing Pei, Zeyao Mo, Shao-Ping Zhu
Institute of Applied Physics and Computational Mathematics
P. O. Box 8009, Beijing 100094, P. R. China
* email: li_jinghong@iapcm.ac.cn

In the target design of the Inertial Confinement Fusion (ICF) program, it is common practice to apply radiation hydrodynamics code to study the key physical processes happened in ICF process, such as hohlraum physics, radiation drive symmetry, capsule implosion physics in the radiation-drive approach of ICF. Recently, many efforts have been done to develop our 2D integrated simulation capability of laser fusion with a variety of optional physical models and numerical methods. In order to effectively integrate the existing codes and to facilitate the development of new codes, we are developing an object-oriented structured-mesh parallel code-supporting infrastructure, called JASMIN. Based on two-dimensional three-temperature hohlraum physics code LARED-H and two-dimensional multi-group radiative transfer code LARED-R, we develop a new generation two-dimensional laser fusion code under the JASMIN infrastructure, which enable us to simulate the whole process of laser fusion from the laser beams' entrance into the hohlraum to the end of implosion. In this paper, we will give a brief description of our new-generation two-dimensional laser fusion code, named LARED-Integration, especially in its physical models, and present some simulation results of holhraum.

Inertial confinement fusion (ICF) is an approach to fusion that relies on the inertia of the fuel mass to provide confinement [1, 2]. Laser ICF is one of ways to fusion energy in the earth, which uses a high power laser as a driver to implode capsules filled with fusion fuel and to produce thermonuclear energy. The capsule implosion is driven by either electron ablation or radiation ablation. In direct drive ICF, the laser beams are aimed directly at the capsule. In indirect drive ICF, laser energy is first converted into x-ray radiation energy inside a high-Z enclosure, called hohlraum. The x-ray radiation drives implosion of the capsule at the hohlraum center.

The largest laser facility in the world, National Ignition Facility (NIF) housed at the Department of Energy's Lawrence Livermore National Laboratory, was formally completed in 2009 [3]. NIF is expected to allow scientists to achieve fusion ignition in the laboratory, obtaining more energy from the target than is provided by the laser. The completion of NIF opens the door to scientific advancement and discovery, and will lead to new breakthroughs in the worlds of astrophysics, materials science and many other scientific disciplines. Recently, the first integrated

experiment at NIF was successful. With the completion of this test, NIF is beginning its next phase of the campaign to culminate in fusion ignition tests. [4]

ICF is complex, and numerical simulations can help us understand what happens in a small hohlraum [5]. Laser ICF research in China, started late in 1970s, is now organized by National High-Tech Inertial Confinement Fusion Committee. Theory and simulation research on laser fusion is one of important parts, and mainly carried out at Institute of Applied Physics and Computational Mathematics (IAPCM). We have been developing two-dimensional (2D) and three-dimensional (3D) simulation codes for laser fusion since middle in 1990s. A system of 2D simulation based on LARED family of codes for the key physics issues of laser fusion was preliminarily built about ten years later [6].

With the rapid development of high performance computers, we need to develop ICF simulation codes to meet the requirement for large-scale simulation of laser fusion research. The difficulty to understand laser ICF physics comes from the fact that many physical processes, such as hydrodynamics, radiative transfer, and Non-LTE atomic physics, occur simultaneously. The great challenges for laser ICF simulation come from: multi-level parallel programming, load imbalance, fast algorithms implementation, code complexity, and data visualization. An easy way to use supercomputer efficiently for large-scale high performance simulation is based on an object-oriented parallel code-supporting infrastructure. JASMIN (J Adaptive Structured Mesh applications Infrastructure) has been developed for high performance computation of multi-physics at IAPCM since 2004 [7]. The infrastructure includes the common components independent of problem, such as the data management and communication, parallel, adaptive and visualization techniques, etc., and mature and standard algorithm. It supports large scale parallel simulations on adaptive structured mesh using massively parallel processing machines. Now, JASMIN have been developed to version 1.8, and finds many applications. It essentially meets requirement for laser ICF codes.

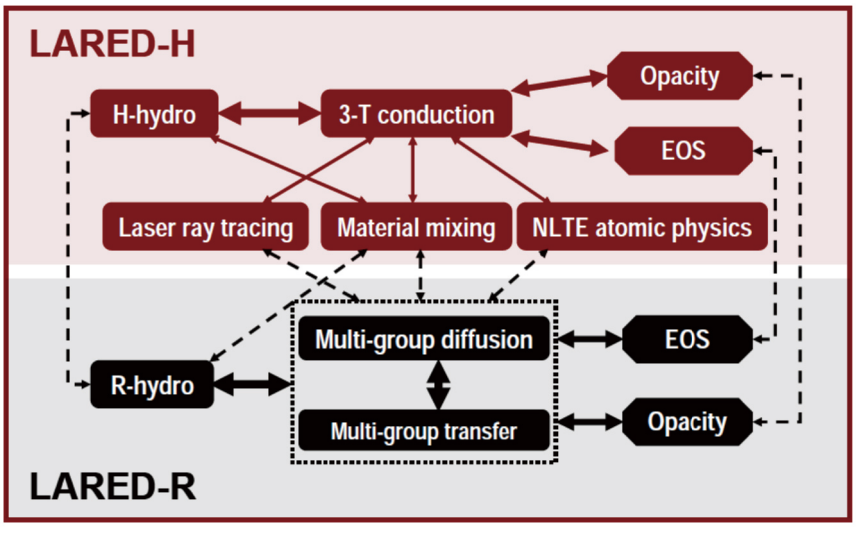

Fig. 1 LARED-Integration code is built mainly by assembling LARED-H and LARED-R codes.

In order to make use of the existing codes, we need assemble LARED-H, LARED-R and LARED-I codes under JASMIN into a new code, named LAERD-integration. It has a variety of

optional physical models and numerical methods. LARED-H is a two-dimensional non-LTE radiation hydrodynamic code for laser-target coupling and hohlraum physics modeling. Using the hohlraum radiation drive provided by the LARED-H calculation, we can perform simulations on capsule implosion and other application problems, such as hydrodynamic instability, radiation flux, opacity, and equation of state (EOS). RDMG is a 1D radiation hydrodynamic code with the radiation treated by models of transport, diffusion, and conduction. This code is used for research of problems such as laser-target coupling physics, capsule physics, radiation transport, radiation ablation, and shock. LARED-R is a 2D multi-group radiation diffusion-transport hydrodynamic code.

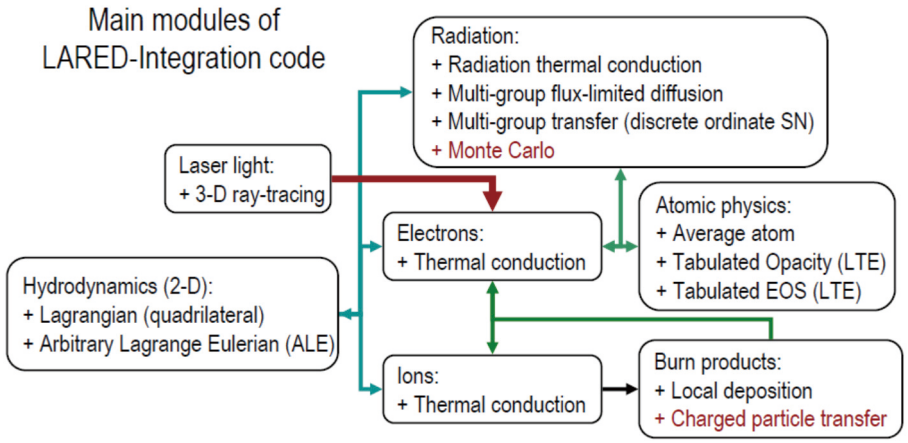

Fig. 1 Main modules of LARED-Integration code

Benefited from JASMIN strong supports in non-structured multi-block mesh for complicated geometry and by allowing Lagrangian mesh across material interface to deal with large deformation, LARED-H code now achieved a whole simulation of NIF ignition-like target.

LARED-Integration code will become our key 2-D physics code for studying laser indirect-drive ICF. Now, we give a brief description on its seven main modules shown in Fig 2: laser light, hydrodnamics, electron, ion, radiation, atomic physics, and burn products. 3-D ray-tracing technique is used for laser light propagation and absorption. Hydrodynamics (2-D) calculation relies on Lagrangian method on quadrilateral grid and Arbitrary Lagrange Eulerian (ALE) method. We use flux-limited thermal conduction for electrons and ions, and use several methods for radiation modeling: thermal conduction, multi-group flux-limited diffusion, multi-group transfer (discrete ordinate S_N), Monte Carlo method (to be installed). Atomic physics includes average atom modeling, Tabulated Opacity (LTE), and Tabulated EOS (LTE). Burn product has two choices: local deposition and Charged particle transfer (to be installed). Compared with LARED-H code, LARED-Integration code enhances physical modeling related to radiation.

LARED-Integration project started in September of 2009. Preliminary 3-temperature results of LLNL NIF ignition target with LARED-Integration increase our confidence.

After successfully passing a benchmark test for 1D laser gold planar target with simulation results of 1D RDMG code, LARED-Integration begins multi-group radiation diffusion simulation. By carefully compared the simulation results shown in Figs 3 and 4, we can find that there are some small differences on the computation mesh movement, the distributions of electron and ion

temperatures, laser deposition energy, and effective radiation temperature in one-group and 64-group radiation diffusion simulations.

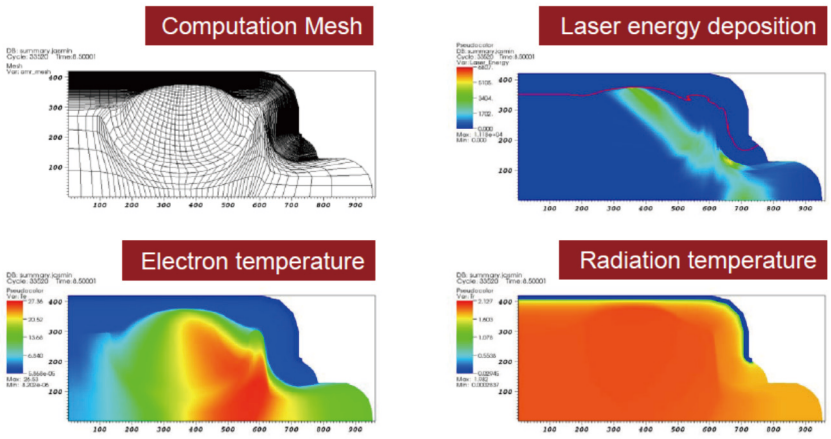

Fig. 3 One-group diffusion results of ICF hohlraum with LARED-Integration code.

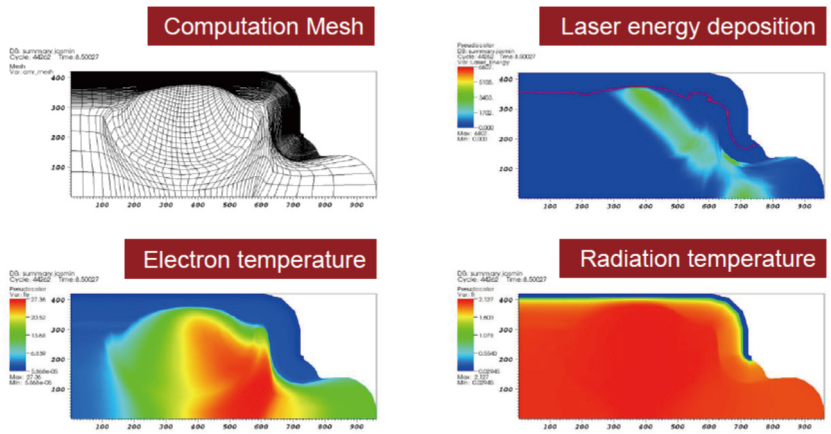

Fig. 4 64-group diffusion results of ICF hohlraum with LARED-Integration code.

In summary, we are developing an object-oriented structured-mesh parallel code-supporting infrastructure JASMIN to effectively integrate the existing codes and to facilitate the development of new codes, Based on two-dimensional three-temperature hohlraum physics code LARED-H and two-dimensional multi-group radiative transfer code LARED-R, we develop a new generation two-dimensional laser fusion code under the JASMIN infrastructure. Now, we have completed the multi-group version of LARED-Integration code for studying indirect-drive ICF. Some numerical simulation results on multi-group radiation diffusion of ICF hohlraum with LARED-Integration code are presented. The multi-group modeling can give us much information on radiation spectrum. The more detail physical modeling on radiation can lead to some small differences on main physical quantities such as temperatures.

ACKNOWLEDGMENT

This work was supported by the National Hi-Tech Inertial Confinement Fusion Committee of China and partly by the National Natural Science Foundation of China under Grant No. 10775019.

References

1. J. D. Lindl, Development of the indirect-drive approach to inertial confinement fusion and the target physics basis for ignition and gain, Phys. Plasmas 2(11), 3933-4024(1995).
2. J. D. Lindl, et al., The physics basis for ignition using indirect-drive targets on the National Ignition Facility, Phys. Plasmas 11(2), 339-491 (2004).
3. http://www.energy.gov/news2009/.
4. http://www.llnl.gov/
5. D. S. Clark, et al., Robustness studies of ignition targets for the National Ignition Facility in two dimensions, Phys. Plasmas 15(5), 056305 (2008).
6. W. B. Pei, The construction of simulation algorithms for laser fusion, Commun. Comput. Phys. 2, 255-270 (2007).
7. http://www.iapcm.ac.cn/jasmin.

Collisional Effects on Fast Electron Generation and Transport in Fast Ignition

H. Sakagami[1], K. Okada[2], T. Taguchi[3] and T. Johzaki[4]

[1] *Fundamental Physics Simulation Division, National Institute for Fusion Science*

[2] *Department of Physics, Nagoya University*

[3] *Department of Electrical and Electronics Engineering, Setsunan University*

[4] *Institute of Laser Engineering, Osaka University*

E-mail: sakagami.hitoshi@nifs.ac.jp

Abstract. As the binary collision process requires much more computation time, a statistical collision model based on modified Langevin equation is developed to reduce it. This collision model is installed into 1D PIC code, and collisional effects on fast electron generation and transport in fast ignition is investigated. In the collisional case, the density profile steepening at the laser front is enhanced due to low electron pressure in the x-direction, and then the low energy component of fast electrons is generated much less than that of the collisionless case.

1. Introduction

The FIREX-I project, which is promoted in Osaka University, aims to demonstrate that the imploded core could be heated up to the ignition temperature, 5[keV]. Efficient heating mechanisms and achievement of such high temperature have not been, however, clarified yet, and we have been promoting the Fast Ignition Integrated Interconnecting code (FI^3) project to boldly explore fast ignition frontiers. Under this project, interaction between ultrahigh-intense laser and Au cone plasma is computed by PIC code. As the Au plasma is extremely overdense, collisional effects (drag and scattering) within the cone would be important. According to 1D collisional PIC code PICLS1d [1], relatively low energy fast electrons, which are expected to mainly heat the core, suffer from strong scattering by highly ionized ions, and lose their kinetic energies through collisional interactions with background electrons and a resistive field. In addition the return current carried by background electrons is significantly damped by the increased resistivity [2].

We have been investigated collisional effects on fast electron generation and transport in fast ignition using 1D PIC code with a statistical collision model. In the collisional case, the pressure of electrons in the x-direction decreases by the isotropic process due to scattering by collisions. Consequently, the density profile steepening at the laser front is enhanced, and then the low energy component (<8[MeV]) of fast electrons is generated much less than that of the collisionless case.

2. Statistical Collision Model

2.1. Antonsen's method

A PIC code introduces a spatial mesh on which fields are defined and the field value on a particle is determined by interpolating field values on neighboring mesh points. This algorithm can greatly reduce calculations, but forces of direct interaction between two particles, i.e. collisions, are automatically filtered out. So PIC codes are widely used for modeling plasmas where collisions are not important in physical processes. When the plasma density is as high as solid density, binary collisions cannot be ignored in determining physical processes such as heat conduction and energy relaxation. Collisional effects can be calculated by the binary collision process, where the collision frequency depends on the relative velocity of pairing particles. Installing the binary collision model into PIC code, however, requires very long computation time. Thus many statistical collision models that are based on Langevin equation for electron-electron collisions are already developed to reduce computations [3-5]. In this paper, we use the collision model based on Antonsen's method [6] which is given by

$$\frac{d\mathrm{v}}{dt} = -\left(\nu_S + \nu_D\right)\mathrm{v} + R(t). \tag{1}$$

In our model, the velocity change of each electron by collisions is computed with two components. First one describes a slowing down term with the electron-electron slowing down rate ν_S by Coulomb collisions and an additional term ν_D given by

$$\nu_S = \frac{8\pi e^4 n_e \ln\Lambda}{m_e^2 \mathrm{v}^3}\mu(x), \quad \mu(x) = \frac{2}{\sqrt{\pi}}\int_0^x t^{1/2} e^{-t} dt, \quad x = \frac{m_e \mathrm{v}^2}{2\mathrm{k}_\mathrm{B} T_e} \tag{2}$$

and

$$\nu_D = -\frac{k_B T_e}{m_e \mathrm{v}}\frac{\partial \nu_S}{\partial \mathrm{v}}. \tag{3}$$

Second component represents a fluctuation term, which is calculated as a random force *R(t)* and *R(t)* satisfies following equations:

$$\begin{cases} \langle R(t)\rangle = 0 \\ \langle R(t)R(t')\rangle = 2D\delta(t-t') \end{cases}, \quad D = \frac{k_B T_e}{m_e}\nu_S. \tag{4}$$

Once we define T_e as a target state, we can compute time evolution of velocity of electrons, and a velocity distribution function is relaxed to Maxwellian distribution with T_e regardless of initial distributions. Existence of ν_D enables us to correctly compute this relaxation process even for a one-dimensional velocity space. These computations have the order of number of particles and CPU time can be saved.

In the fast ignition scheme, fast electrons are generated by ultrahigh-intense laser and propagate toward the core through the dense plasma. Thus collisions between fast (beam) and background electrons should be important. First, we calculate collisional effects between background 90,000 electrons ($\mathrm{v}_{\mathrm{thermal}}=\mathrm{v}_{\mathrm{th0}}$, $\mathrm{v}_{\mathrm{drift}}=0$) and beam 10,000 electrons ($\mathrm{v}_{\mathrm{thermal}}=0$,

$v_{drift}=5v_{th0}$) using equations (1)-(4). Our statistical collision model is extended to Maxwellian distribution with the drift velocity, and the thermal and drift velocities of the target state are determined as an equilibrium state to conserve total energy and momentum of electrons. Time evolutions of thermal and drift velocities of all electrons are shown in figure 1 (a). Each velocity is relaxed to the desired value of the equilibrium state, namely $1.79v_{th0}$ and $0.5v_{th0}$, respectively. Time evolutions of background, beam and total electron energies are shown in figure 1 (b). The total energy is not conserved in early stage. In this situation, beam and background electrons are independently relaxed to the target state, where the total energy and momentum of electrons are the same as those of the initial state. As an averaged velocity of background electrons is lower than that of beam electrons, background electrons are relaxed much faster than beam electrons because ν_S is inversely proportional to the cube of electron velocity. Thus the background electron energy quickly increases, but the beam electron energy slowly decreases without conserving the total energy.

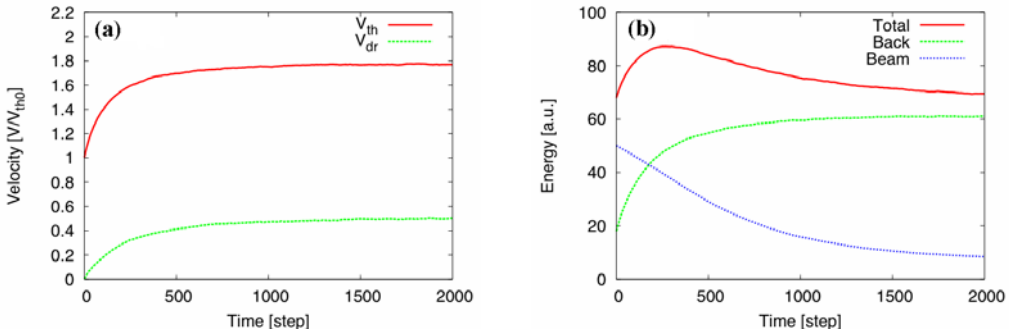

Figure 1. Collisions between background and beam electrons. Time evolutions of (a) thermal and drift velocities of all electrons, and (b) background, beam and total electron energies.

2.2. Improved Collision Model

To conserve the total energy and momentum of electrons at any time, we improve algorithm of our statistical collision model as follows: 1) discriminate between background and beam electrons, 2) measure thermal and drift velocities of background electrons as the target state, 3) compute collisions of beam electrons with the target state and calculate momentum and energy losses, 4) compute collisions of background electrons with the target state, and 5) correct background electron velocity to conserve the total energy and momentum [4]. Momentum and energy losses are given by

$$\sum_{beam}\left(v_{before}-v_{after}\right)=\Delta M,\quad \sum_{beam}\left(v_{before}^{2}-v_{after}^{2}\right)=\Delta E. \tag{5}$$

We define correction terms for background electrons as follows:

$$v'_{after}=\alpha(v_{after}-v_{drift})+v_{drift}+\beta. \tag{6}$$

The conservation of the total momentum and energy after correction is given by

$$\sum_{background}\left(\mathrm{v}'_{after}-\mathrm{v}_{before}\right)=\Delta M,\quad \sum_{background}\left(\mathrm{v}'^{2}_{after}-\mathrm{v}^{2}_{before}\right)=\Delta E\,. \tag{7}$$

As the thermal and drift velocities of background electrons are the same as those of the target state, we can assume that collision calculations of background electrons preserve the total momentum and energy and give following equations:

$$\sum_{background}\left(\mathrm{v}_{after}-\mathrm{v}_{before}\right)=0,\quad \sum_{background}\left(\mathrm{v}^{2}_{after}-\mathrm{v}^{2}_{before}\right)=0\,. \tag{8}$$

From equations (5) – (8), we can get the correction terms as follows:

$$\alpha=\left[\left(\Delta E-\frac{\Delta M^{2}}{N}-2\mathrm{v}_{drift}\Delta M\right)\left(\sum_{background}\mathrm{v}^{2}_{after}-N\mathrm{v}^{2}_{drift}\right)^{-1}+1\right]^{1/2},\quad \beta=\frac{\Delta M}{N}\,, \tag{9}$$

where N is the number of background electrons.

Time evolutions of thermal and drift velocities of all electrons for the same problem are shown in figure 2 (a). We give the target state as the equilibrium state in the previous collision model, but each velocity is asymptotically approaching to the value of the equilibrium state even though we give only the current state as the instantaneous target state of background electrons. Time evolutions of background, beam and total electron energies are shown in figure 2 (b). The total energy is always conserved as we expect. It is noted that the beam electron energy exponentially drops in figure 1 (b), but it has an inflection point in figure 2 (b) just as observed in the binary collision calculation [1].

We extend our electron-electron collision model to a two-dimensional velocity space, and then install it into 1D PIC code. We also install a simple electron-ion scattering model in which the scattering angle is randomly chosen with the Gaussian distribution [7]. We divide the whole simulation system into subspaces. In each subspace, the target state is individually evaluated and collision calculations are performed.

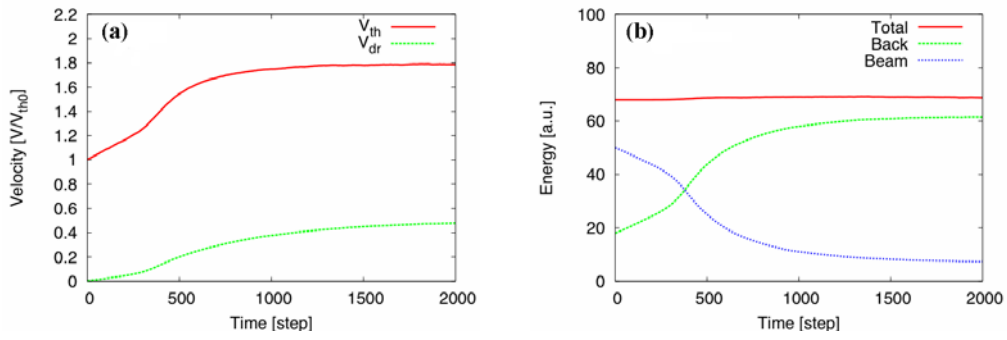

Figure 2. Collision calculations with improved model. Time evolutions of (a) thermal and drift velocities of all electrons, and (b) background, beam and total electron energies.

3. Collisional Effects

To evaluate collisional effects in the fast ignition, we set the heating laser to λ_L=1.06[μm], $\tau_{rise/fall}$=200[fs], τ_{flat}=500[fs], $I_L=10^{20}$[W/cm^2], and the Au-cone tip is introduced as 10[μm], 500n_{cr}, real mass and Z=30 plasma with preformed Au plasma, which has a exponential profile of the scale length L=1[μm] with density from 0.1n_{cr} up to 500n_{cr}. Time evolutions of fast electron beam intensity, fast electron energy spectra (t=0.5 and 1[ps]) and electron density profiles near the laser front (t=0.5 and 1[ps]) are shown in figure 3 (a), (b) and (c), respectively. The fast electron beam intensity is reduced by collisions. Fast electron energy spectra and electron density profiles at t=0.5[ps] are almost same for both cases, but the number of fast electrons in a low energy component (<8[MeV]) at t=1[ps] is also reduced by collisions. As fast electrons are mainly accelerated into an x-direction due to the relativistic laser-plasma interaction, the electron velocity distribution in the collisional case becomes more isotropic than that of the collisionless case due to scattering by collisions. This isotropic process repeatedly occurs because of fast electron circulations and the pressure of electrons in the x-direction decreases. The density profile steepening at the laser front, therefore, is enhanced in the collisional case at t=1[ps] (*see figure 3 (c)*), and then the low energy component of fast electrons is generated much less than that in the collisionless case [2]. However, high energy components (>8[MeV]) of fast electrons are similarly generated in both cases because of same structures of a low density ledge.

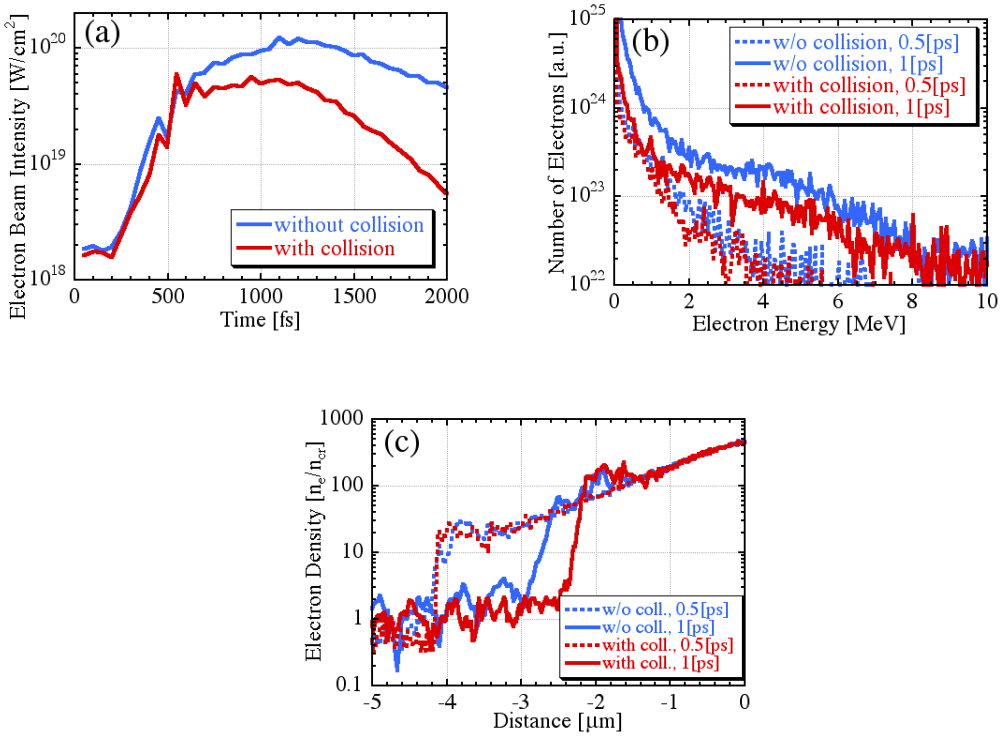

Figure 3. Collisional effects. (a) Time evolutions of fast electron beam intensity thermal, (b) time averaged fast electron energy spectra and (c) electron density profiles near laser front at t=1[ps].

For the parameters used here, collisions have little effect; and more research is needed to investigate collisional effects on fast electron generation and transport in fast ignition.

Acknowledgments

This work was partially supported by JSPS Grant-in-Aid for Scientific Research (C)(22540511) and the JSPS-CAS Core-University Program in the field of Laser Plasma and High Energy Density Physics.

References

[1] Y. Sentoku and A. J. Kemp, J. Comput. Phys., 227, 6846 (2008).
[2] T. Johzaki, et al., Plasma Phys. Control. Fusion, 51, 014002 (2009).
[3] M. E. Jones, et al., J. Comput. Phys. 123 169 (1996).
[4] W. M. Manheimer, M. Lampe, G. Joyce, J. Comput. Phys., 138, 563 (1997).
[5] B. I. Cohen, L. Divol, A. B. Langdon, and E. A. Williams, Phys. Plasmas, 13, 022705 (2006).
[6] T. Taguchi, T. M. Antonsen Jr., et al., Optics Express, 18, 2389 (2010).
[7] T. Takizuka and H. Abe, J. Comp. Phys., 25, 205 (1977).

Angular resolved electron spectra relevant to core heating

H. Habara,[1,2] A. Okabayashi, [1,2] T. Iwawaki,[1,2)] T. Tanimoto,[3] N. Nakanii,[1,2] ,K. Shimada,[1,2] T. Yabuuchi,[4] K. Kondo,[3] and K. A Tanaka[1,2]
[1]*Graduate school of Engineering, Osaka University, Yamada-oka, 2-1, Suita, Osaka, Japan*
[2]*Institute of Laser Engineering, Osaka University, Yamada-oka, 2-6, Suita, Osaka, Japan*
[3]*Kansai Photon Science Institute, Japan Atomic Energy Agency, Umemidai, 8-1-7, kizugawa, Kyoto, Japan*
[4]*Department of Mechanical and Aerospace Engineering, University of California–San Diego, 9500 Gillman Drive 0411, La Jolla, California 92093-0411, USA*

Abstract. In order to obtain the angular dependent electron energy distributions, we developed a multichannel electron spectrometer (MCESM) with high energy and angular resolutions. The MCESM consists of seven small electron spectrometers set in every 5 deg. on the basement, each of which detection range is up to 25 MeV. In the experiment, we successfully obtained electron spectra from imploded cone-shell target as well as gold plane target irradiated by ultra intense (300 J/5 ps) laser beam. In order to understand the effect of collisional heating process, a relativistic Monte-Carlo calculation is carried out.

I. INTRODUCTION

In the fast ignition (FI) of inertial fusion research [1], an ultra intense laser (UIL) pulse is irradiated on the imploded plasma in order to generate hot electrons to heat the high-density core plasma. At the time, the measurement of fast electrons (number, slope temperature, emission angle, and so on) is crucially important for estimation of heating efficiency to the core. Especially, it is considered that the electron beam has an emission divergence which can reduce the heating efficiency. In the previous studies, the beam divergence has been measured without energy distribution such as measurements of Kα X-rays [2] or optical transition radiation (OTR) [3], and different measurement techniques or different conditions of laser-plasma interaction give different beam divergences [4,5]. In addition, momentum distribution of electron beam could have a complicated structure; ex. two different acceleration mechanisms (J×B [6] or Brunel like[7]), and for cone-in-shell target, it is expected that the electrons are accelerated along to the cone-wall, not to the cone rear-surface [8]. From these viewpoints, we performed a angular resolved electron spectra could be very important information for core heating.

II. DEVELOPMENT OF MULTICHANNEL ELECTRON SPECTROMETER

We developed a multi-channel electron spectrometer (MCESM) with a high angular resolution for FI experiment [9]. Basically the magnet electron spectrometer is very simple diagnostics to measure the energy of electrons. When the electrons reach in the area where the magnetic field exists, the electron orbit is bent due to Lorentz force. If magnetic flux density can be considered as a constant, the electrons move according to simple Larmor motion only determined by the electron kinetic energy. Because different energy electrons reach on the different position in detector, the electron energy distribution can be easily obtained. As an electron detector, we use an IP which has a large dynamic range (~10^5) and a high sensitivity (~100 times higher than normal X-ray film). In addition IP is free from strong electromagnetic pulse (EMP) noises created by UIL interaction with target. For the single spectrometer, detection errors are mainly caused by finite collimator size as described in the later section. On the other hand MCESM has more complicated factors arisen from the alignment errors in the channels.

A. Required specifications

We consider the required range and resolution on angle and energy for MCESM. As mentioned in the introduction, the measurement of spectral modification of the electrons in different viewing angle gives us an important insight of heating mechanism to the core. In the previous FI experiment [10], the core diameter is about 50 μm and the distance from the center of core plasma to gold cone tip is also 50 μm. From this geometry it is expected that the electrons within 60° divergence angles are possible to interact with the core. We therefore decide that the angular range must be about 60° with 5° angular resolutions. On the other hand, the modification on electron spectrum is mostly appeared within 10 MeV at the previous experiment. So the energy range is set from 0.2 to 25 MeV with high energy resolution (it is about 50 keV at 10 MeV).

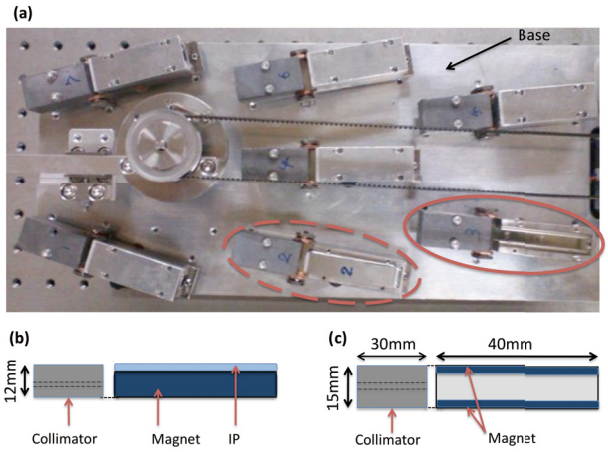

FIG.1. (a) MCESM stage. (b) Side view of one ESM. (c) Top view of ESM.

B. Mechanical design

We designed the MCESM for the Gekko FIREX experiment. The diameter of the Gekko chamber is 2 m, and the nearest port angle is 20°. It is therefore necessary to insert the spectrometer to the chamber and bring it close to target chamber center (TCC) in order to obtain the required angular resolution. Due to the restriction of the solid angle of one chamber port, we decide to cover 35° angular ranges with about 20 cm distance from TCC. MCESM is translated close to TCC via motorized rails. The head of MCESM has a mock-up shell target that can move in and out inside the vacuum chamber. By adjusting the target in the optimum position using the target monitor system, MCESM can be assured to set the exact position with the error less than 100 μm in three dimensions.

C. Arrangement of ESM channels

Figure 1 (a) shows seven ESM channels arranged on the basement with 5° angular intervals with different distance from 15.5 to 33.0 cm. Figures 1(b) and (c) are the top and side view of one channel. The magnetic flux density is 0.45 T and the magnet length is 40 mm. The collimator is set in the front side of the magnet pair. The total length is 75 mm including a gap between magnets and collimator. The width and height is 15 and 12 mm, respectively. IP is set on the top of the magnets with cover holder parallel to the electron beam. In order to avoid exposure to x ray or laser light, the IP is shielded by thin aluminum film. The dotted and solid circles in Fig. 1(a) represent the ESM channel with and without IP.

D. Error estimation

Even electron beam is injected parallel to the collimator, the error on electron energy depends on the collimator size and height to IP. Different energy electrons coming from the top (bottom) of collimator reach as same position on IP through the orbit as the center part of electrons. From this consideration, we choose the collimator size and h in order that maximum error on energy of electrons becomes less than 5%. On the other hand, the electron number is in proportion to the cross section that electrons pass the collimator. If ESM is aligned correctly, the cross section is same as the collimator size. However, if it is slightly tilted or rotated, the collimator clips electron beam, resulting in reduction of number of detected electrons. Especially for MCESM, because each ESM channel has a freedom in three dimensions individually, the relative error loses reliability for angular distribution of fast electrons. Taking account of the off-line alignment method above, the maximum reduction on number is estimated at about 15%.

Moreover, the error due to setting accuracy of the mock-up target in TCC can be negligible because the collimator size is much larger than the core size (~50 μm).

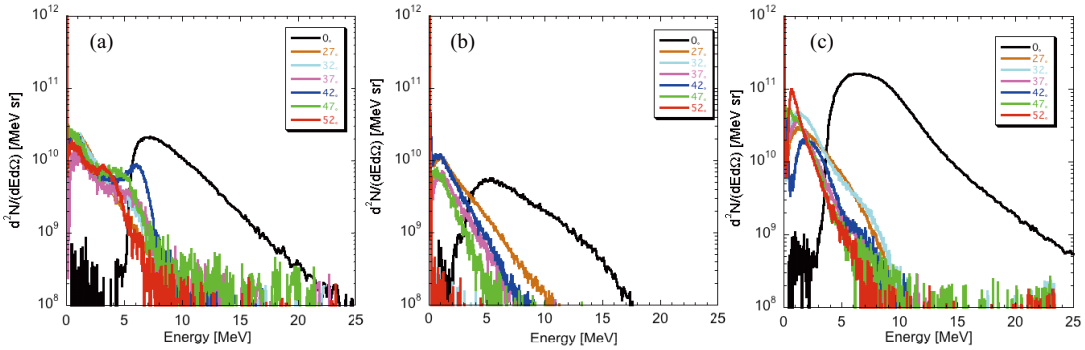

FIG.2. Typical electron spectra. (a) Cone target. (b) Solid target. (c) Imploded core target.

III. FAST IGNITION EXPERIMENT

We measured the angular dependent electron spectra with the MCESM and single channel ESM at fast ignition integrated experiment conducted in Osaka University. The detector angles are 0°, 26.9°, 31.7°, 36.7°, 41.8°, 47.1°, 52.4°, and 57.9° from the laser axis, respectively. Unfortunately in most of experiments, electron spectrum was not obtained at 57.9° due to poor S/N ratio. The typical results are shown in Fig. 2. Fig. 2(a) and (b) shows spectra taken from cone and solid target, respectively. Comparing these two results, the spectra from cone target exhibit second peaks on the spectra from 37° to 52°. And also more number of electrons on the laser axis even the laser energy is 2/3 of the solid target shot. These results agree with the results from 2D PIC calculation [8], which shows that lower energy electrons are accelerated toward the cone-surface, whereas the higher electrons flow between laser axis and target normal directions.

On the other hand, Fig. 2(c) shows the spectra taken from imploded shell target with re-entrant cone. The spectra are taken at the shot when heating laser energy is 310 J with 5 ps pulse duration. The shell diameter is 500 μm and the cone tip diameter is 10 μm with 10 μm thickness. Implosion energy is 2.9 kJ. The intense beam is injected at the timing of maximum implosion. At this shot the neutron yield is 1×10^4. In the result, it can be seen that the emission angle of hot electrons passing through core plasma is smaller than that from gold plane foil. Concretely, in the case of gold foil, the emission angle is about 30° in half width of half maximum by Gaussian fitting. On the other hand for imploded plasma, this decreases to about 10°. The narrowing can be considered that collimating characteristics of the cone structure [8] or effect of presence of preformed plasma filled in gold cone [11].

In the previous FI integrated experiment, we observed the spectral modification due to core heating by the fast electrons. Figure 3 shows the electron spectra taken at (a) 20° and (b) 40° from the laser axis. On the near-axis spectra, there are the significant modifications for wider energy range only when the intense laser light injected at the maximum compression timing of the core (0 ps) whereas no reduction at off-timing spectra (+50 or -170 ps from the maximum compression). We also observed the neutron yield enhancement only when such modification was observed. On the other hand, we did not observe such modification in the off-axis spectra in which electrons did

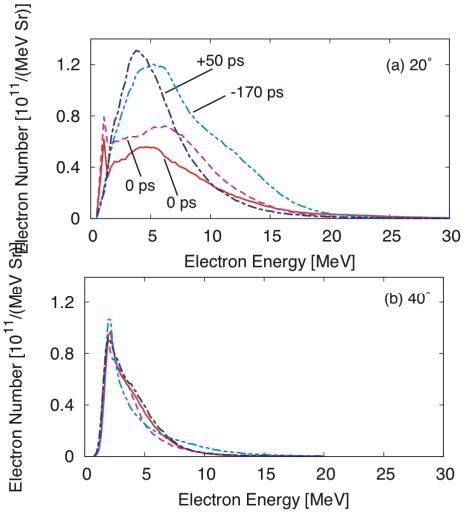

FIG.3. Spectral modulation due to core heating on the spectra detected at (a) 20° and (b) 40° [10]

not pass through the core plasma taking into account of core size and position of cone tip. In the conclusion, this reduction is a direct evidence of core heating by the fast electrons [10].

IV. MONTE-CARLO TESTING

As shown in the previous sections, the angular resolved electron spectra are one of useful diagnostics in order to understand the imbedded physics of transport and heating in dense plasma. The heating mechanisms are now intensively investigating by using computer simulations [12-14], but it is still under investigations. Therefore for the simple estimation of heated temperature of the core, we carried out calculations of spatial temperature distribution in the superdense matter by the EGS5 (Electron Gamma Shower 5) [15] program using the experimental parameters [16]. EGS5 is the electromagnetic cascade Monte-Carlo code of electron and photon transportation calculation in a wide-range of energies in an arbitrary geometry. Specifically, the transportation of electrons, photons, and positrons in any elements, compounds, and the mixture can be treated.

When electrons pass in the material, the energy is dissipated through the ionization and the propagation direction is shifted via multiple scattering. In the process, X-rays are radiated via bresmsstrahlung, Compton scattering, and the electron pair creation, etc., resulting in the electromagnetic cascade shower happens. The types of Fredholm transportation equation and the Monte-Carlo method are used as the basis for this electromagnetic cascade shower. The particle translocation is as follows: (1) Set the initial particle location, energy, and weight, (2) Determine the free path of the particle to the next collision point, (3) Calculate the weight on the particle with the next collision point, (4) Settle the scattering angle according to energy and incident angle in the next collision point. The process ends if the energy is below the cutoff within the range of the object otherwise the calculation goes back to step 2. In the calculation, the step size is not decided discretely but is taken as a sampling random hinge.

A. Simulation conditions

In EGS5 simulation, required are the conditions of the material composition, geometry, incident particle, and the physical mechanism of object substance. In our calculations, the superdense material geometry is taken from the dense plasma core at the integrated FI experiment [10] at Institute of Laser Engineering. The plasma electron density profile of the superdense matter is fitted by a suitable Gaussian function onto the data point [10]. Since it is difficult to define the density and the material composition by a continuous function on the programming material composition data in EGS5 simulations, density intervals are given to divide the core sphere (radius ~ 24 μm) into 9 layers. Also to evaluate the local energy deposition, the region was sliced into 4×4×4. In the result, the sphere is subdivided to 296 regions as the logical product of the sphere in the code.

Regarding to the incident particle condition, it is necessary to approximate the energy spectrum of fast electrons with a relativistic Maxwellian that fits well with the ESM experimental data. The electron numbers in the high-energy part of this distribution is quite less than the low-energy part, so that the distribution of high energy electrons is not so important on the fitting (only less than 10 MeV fast electrons are well fitted to the approximation). The electron spatial distribution was appropriately given by Gaussian distribution as centering the laser directions with about ±20° dispersions (FWHM).

Multiple scattering, bresmsstrahlung, Møller scattering, and electron pair creation, Compton scattering, Rayleigh scattering, and photoelectric absorption are considered as physical mechanisms. However, neither BhaBha scattering, positron annihilation, nor electron impact ionization are excluded because these effects are almost negligible for the energy range in this simulation. The equilibrium plasma that ionized completely has been assumed, so that the optional definitions such as Auger electron, polarized lights of the secondary photon, and Compton profiles are not taken into consideration.

B. Results and Discussions

At first we check whether the incident electrons are correctly generated in the calculation. The output average energy of the spectrum was 6.65 MeV when the no plasma is presented. The energy spectrum uses the approximate function by a relativistic Maxwellian and the average energy is calculated

with $3T_e$ by argument $1/T_e$ about the electron temperature of the spectrum. The fitting curve we used is T_e=1/0.4512, resulting in $3T_e \approx 6.648$, in agreement with the output value above. This indicates that the incident particles were handled correctly in the calculation.

The track data of electrons is shown in Fig. 4(a). Around the incidence axis of laser, the high-energy electron easily passes through the superdense matter. On the other hand the low-energy electron is stopped because of multiple scattering by the collision and apparently has been absorbed. It is clear that the energy deposition rate of the low-energy electron (≤ 1 MeV) is significant. In the calculation result, the whole energy deposition to the superdense matter was about 0.384 MeV × electron number (10 millions).

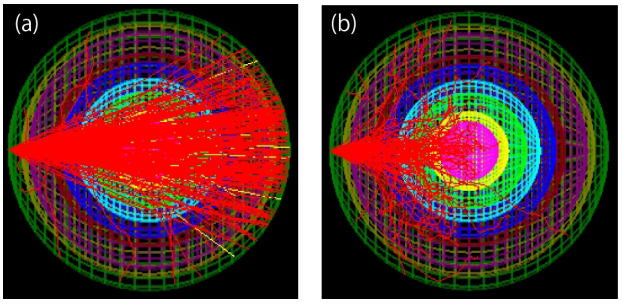

FIG.4. (a) Particle track data in the case that incident electron spectrum is relativistic Maxwellian, and (b) mono energy of 0.5 MeV. The diameter of the most outside sphere is 0.00482 cm [16].

It is interesting to consider energy deposition by mono energy electrons at the low-energy range without changing other conditions for this simulation. In the results, the energy deposition gives 80-100 % of the energy of the electron to the vicinity of 0.5 MeV, 50-70 % for 0.7-1 MeV, and the energy deposition decreases to 0.38 MeV gradually when incident energy is over 3 MeV. Therefore, it is clear that the energy deposition to the core can increase if fast electrons of which energy is around 1 MeV can be enhanced.

Finally we calculate the electron temperature from the energy deposition in each region using a relativistic Maxwellian spectrum. In the energy deposition processes, the energy was also consumed for creation of secondary particles such as X-ray. However, the energy deposition by photons is usually smaller than the thermal energy, so that all of energy deposition ε was used for heating and then calculated the temperature from ε=(3/2)T. For the simplicity, ion temperature T_i is assumed to be same with electron temperature T_e (T_e=T/2). The energy deposition calculated in each region is divided by the volume and the electron density of the region. The value was normalized by the initial energy of fast electrons = 24 J (the laser energy = 60 J and the conversion efficiency 40 %). As the result, the maximum electron temperature becomes 50 eV at the core center in the case of energy spectrum by Relativistic Maxwellian (T_e = 2.216 MeV).

In the recent experiment [10] of the same conditions, the core temperature is 120 eV (±20%) from the number of thermonuclear neutrons when 60 J additional laser light was injected. This is higher than that in the simulation. This may be reasonable by considering that the calculation includes only collisional processes.

V. CONCLUSION

We have developed a multichannel electron spectrometer with high spatial resolution and wide angular ranges. The MCESM consists 7 channels with 5° angular resolution with detection energy range from 0.5 to 25 MeV. The error on the electron number and energy is estimated as about 15% and 5%. The measured electron spectra show the difference of emission angle between foil and imploded cone-shell target, 30° and near 10°, respectively. In addition comparing the angular resolved electron spectra from cone and solid target, enhancement of number of electrons and existence of second peak imply the surface acceleration and resulting collimaion of electrons on the cone wall as predicted in simulations. Also significant modification of electron spectra indicates strong heating of the core. In order to estimate collisional heating to the core by fast electrons, we performed a relativistic Monte-Carlo calculation. Because the results only reproduce the half of the heated temperature in the experiment, the collective processes is also important to understand the core heating mechanism. However the measurement of angular resolved electron spectra is very important technique to understand the physics on interaction, transport, and heating by the fast electrons.

ACKNOWLEDGMENTS

The authors gratefully acknowledge the support of the Grant-in-Aid for Scientific Research (Contract No. 19206099) and International Collaboration for High Energy Density Science (ICHEDS) of Core-to-Core Program organized by Japan Society for the Promotion of Science (JSPS). And also this work was partially supported by the JSPS-CAS Core-University Program in the field of Laser Plasma and High Energy Density Physics.

[1] M. Tabak et al., Phys. Plasmas 1, 1626 (1994).
[2] R.B. Stephens et al., Phys. Rev. E 69 (2004) 066414.
[3] J. J. Santos et al., Phys. Plasmas. **14**, 103107 (2007).
[4] J. S. Green et al., Phys. Rev. Lett. **100**, 015003 (2008).
[5] H. Habara et al., Phys. Rev. Lett. 104 (2010) 055001.
[6] S.C. Wilks, W.L. Kruer, M. Tabak and A.B. Langdon, Phys. Rev. Lett. 69 (1992) 1383.
[7] F. Brunel, Phys. Rev. Lett. 59 (1987) 52.
[8] Y. Sentoku, K. Mima, P. Kaw, and K. Nishikawa, Phys. Rev. Lett. 90 (2003) 155001; H. Habara et al., Phys. Rev. Lett. 97 (2006) 095004.
[9] T. Iwawaki et al., Rev. Sci. Instruments 81 (2010) 10E535.
[10] R. Kodama et al., Nature, 412, 798, (2001); T. Yabuuchi et al., New J. Phys. 11, 093031 (2009).
[11] T. Tanimoto et al., J. Phys. 112, 022095 (2008)
[12] A. J. Kemp et al., Phys. Rev. Lett. 97, 235001 (2006).
[13] R.B. Campbell et al., Phys. Rev. Lett. 94 (2005) 055001.
[14] R.J. Mason, Phys. Rev. Lett. 96 (2006) 035001.
[15] KEK, Stanford Linear Accelerator Center, the University of Michigan teams, SLAC-R-730, (2007).
[16] A. Okabayashi, T. Yabuuchi, H. Habara and K.A. Tanaka, J. Plasma and Fusion Res. 8 (2009) 122

Relativistic correction of $(v/c)^2$ to the collective Thomson scattering from high-temperature high-density plasmas

Jian Zheng,* Chenfanfu Jiang, and Bin Zhao
CAS Key Laboratory of Basic Plasma Physics, University of Science and Technology of China, Hefei, Anhui 230026, People's Republic of China and
Department of Modern Physics, University of Science and Technology of China, Hefei, Anhui 230026, People's Republic of China

Collective Thomson scattering with inclusion of relativistic correction of $(v/c)^2$ is theoretically investigated. The correction is rather small when inferring plasma parameters from the spectra off thermal electron plasma waves in the plasmas. Since the full formula of the corrected result is rather complicated, a simplified one is derived for the sake of practical use, which agrees well with the un-simplified one.

PACS numbers: 52.25.Os, 52.25.Gj, 52.70.Kz

I. INTRODUCTION

Thomson scattering [1, 2], which can provide highly reliable time- and space-resolved measurements of plasma parameters such as electron density, temperature and plasma flow, is now widely utilized to measure laser-produced plasmas relevant to inertial confinement fusion (ICF) in recent years [3–11]. Thomson scattering is usually operated in the *collective* regime in the field of ICF. In the most of these experiments, only the ion-acoustic features of the Thomson scattering spectra are detected, and the following equation is usually adopted in inferring plasma parameters from experimental data [1, 2],

$$\frac{d^2P}{d\omega_s d\Omega} = r_e^2 I_0 V_s n_e (\mathbf{e}_0 \times \mathbf{n}_s)^2 S(\omega, k). \tag{1}$$

Here r_e is the classical electron radius, I_0 is the intensity of the probe light, V_s is the scattering volume, n_e is the electron density, $\mathbf{e}_0$ is the polarization of the probe light, $\mathbf{n}_s$ is the scattering direction, $S(k,\omega)$ is the so-called dynamic form factor , and ω and $\mathbf{k}$ are the differential frequency and wave vector respectively given by

$$\omega = \omega_s - \omega_0, \tag{2a}$$
$$\mathbf{k} = \mathbf{k}_s - \mathbf{k}_0, \tag{2b}$$

where $\omega_{0,s}$ is the frequency of the probe/scattering light and $\mathbf{k}_{0,s}$ is the wave vector of the probe/scattering light. *The wave number of the electromagnetic wave depends on the plasma density* $k_{0,s} = (\omega_{0,s}/c)(1-\omega_{pe}^2/\omega_{0,s}^2)^{1/2}$*, where* ω_{pe} *is the Langmuir frequency of the plasma. When the plasma density is dilute and the differential frequency is small, the differential wave vector is usually approximated as [1, 2],*

$$\mathbf{k} = \frac{\omega_0}{c}\mathbf{n}_s - \mathbf{k}_0 \tag{3}$$

In the previous experiments, it is Eq. (3) that is used to calculate the differential wave vector instead of the accurate one (2b). For a collisionless non-relativistic plasma in quasi-equilibrium state, the dynamic form factor is given by

$$S(\omega,k) = \frac{1}{n_e}\left(\left|1-\frac{\chi_{e0}}{\epsilon_{l0}}\right|^2 F_{e0} + Z^2\left|\frac{\chi_{e0}}{\epsilon_{l0}}\right|^2 F_{i0}\right), \tag{4}$$

*Electronic address: jzheng@ustc.edu.cn

where ϵ_{l0} is the non-relativistic longitudinal permittivity of the plasma, and χ_{e0} is the non-relativistic electron susceptibility, Z is the charge state of the ions, and $F_{e0,i0}$ are given by

$$\begin{aligned} F_{e0,i0} &= \int f_{e0,i0}(\mathbf{p})\delta(\omega - \mathbf{k}\cdot\mathbf{v})d^3p. \\ &= \frac{n_{e,i}}{\sqrt{2\pi}kv_{e,i}} \exp\left(-\frac{\omega^2}{2k^2v_{e,i}^2}\right) \end{aligned} \tag{5}$$

Here, $f_{e0,i0}$ are the Maxwellian momentum distribution functions of the electrons and ions, $\delta(x)$ is the $\delta-$function, and $v_{e,i} = \sqrt{T_{e,i}/m_{e,i}}$ are the electron/ion thermal speeds.

The theories of Thomson scattering are thus developed to include various effects that may have important influences on the dynamic form factor $S(\omega, k)$, such as super-Gaussian electron velocity distribution due to strong inverse bremsstrahlung absorption [12, 13], frequent Coulomb collisions [14, 15] and plasma inhomogeneity [16, 17], etc. However, scattering spectra from thermal electron plasma waves that allow direct measurements of electron density and temperature are also successfully detected by Glenzer et al [6]. Noticing the plasma temperature is rather high in this experiment and that the differential frequency ω is no longer negligible in comparison with the probe frequency ω_0, we revisited the first order correction of v/c (where v and c are the electron and light speeds, respectively) to the scattering power spectrum [18], and obtained the same result as that presented in the monograph of Sheffield [2],

$$\frac{d^2P}{d\omega_s d\Omega} = r_e^2 I_0 V_s n_e (\mathbf{e}_0 \times \mathbf{n}_s)^2 S(k,\omega)\left(1 + \frac{2\omega}{\omega_0}\right). \tag{6}$$

Here $S(k,\omega)$ in Eq. (6) is the same as the one in Eq. (1), and the new term $2\omega/\omega_0$ comes from the first order correction of v/c. Another correction to Eq. (1) is implied with the exact differential wave vector,

$$\mathbf{k} = \frac{\omega_s}{c}\mathbf{n}_s - \mathbf{k}_0. \tag{7}$$

Equations (3) and (7) are different from each other with a term proportional to ω/ω_0. With inclusion of the first order of v/c, we find that not only the intensity but also the spectral profile of the scattering light off electron plasma waves changes significantly [18]. With Eq. (6), the inferred electron temperature from the scattering spectra in Ref. 6 is about 30% higher than that obtained with Eq. (1) [18]. *With inclusion of the dependence of wave number on plasma density, the differential wave vector becomes a little smaller, leading to a smaller wavelength of the resonance peaks of the scattering spectrum[18].*

As indicated in Eq. (6), the correction term of $2\omega/\omega_0$ can become the order of 1 when light scattering from electron plasma waves is detected. This fact means that the first order correction may not be enough in the fitting of Thomson scattering spectra from electron plasma waves in high-temperature high-density plasmas. On the other hand, the electron temperature in coronal region of laser-produced plasmas may reach 5 keV, and plasmas become mildly relativistic in the coming ignition experiment [25]. Therefore, a theory of collective Thomson scattering with inclusion of the relativistic correction, i.e., $(v/c)^2$, may be necessary for such high-temperature plasmas. Actually, the relativistic correction to Thomson scattering was already addressed many years ago [19–24]. However, these previous studies concentrated on the relativistic effect on incoherent Thomson scattering. In this paper, we calculate the power spectrum of collective Thomson scattering with the correction up to $(v/c)^2$. *When the ration of the electron density T_e to the electron rest energy m_ec^2 is over a few percent, or when the phase velocity of the detected fluctuations is larger than $0.2c$, the relativistic effects should be included in the theory of Thomson scattering.* The electron temperature inferred with the corrected theory is a little higher than that inferred with the theory only with inclusion of v/c. Since the full formula of the corrected spectrum is rather lengthy and complicated, a simplified one is derived for routine applications. The results may make collective Thomson scattering a more accurate method of diagnosing plasma parameters in laser-produced high-temperature plasmas.

II. BASIC EQUATIONS

In the wave zone, the spectral energy emitted from N accelerated electrons into the solid angle $d\Omega$ is approximately given by [18]

$$\frac{d^2\mathcal{E}_{\mathbf{n},\omega_s}}{d\Omega d\omega_s} = \frac{e^2}{8\pi^2c^3}\left|\sum_{i=1}^{N}\int_{-\infty}^{\infty}\frac{d}{d\tau}\left[\frac{\mathbf{v}_i(\tau)\times\mathbf{n}_s}{1-\mathbf{n}_s\cdot\mathbf{v}_i(\tau)/c}\right]e^{i\omega_s\tau - i(\omega_s/c)\mathbf{n}_s\cdot\mathbf{r}_i(\tau)}d\tau\right|^2, \tag{8}$$

where $-e$ is the electron charge, $\mathbf{v}_i$ and $\mathbf{r}_i$ are the velocity and coordinate of the $i-$th electron, $\mathbf{R}$ is the observation coordinate, and τ is the retardation time defined as $t = \tau + R/c - \mathbf{n}_s \cdot \mathbf{r}_i(\tau)/c$, and ω_s denotes the frequency of the emitted electromagnetic waves.

The incident wave is assumed plane, monochromatic and linearly polarized,

$$\mathbf{E}_0 = \mathbf{e}_0 E_0 \cos(\mathbf{k}_0 \cdot \mathbf{r} - \omega_0 t), \tag{9}$$

$$\mathbf{B}_0 = (\mathbf{n}_0 \times \mathbf{e}_0) E_0 \cos(\mathbf{k}_0 \cdot \mathbf{r} - \omega_0 t), \tag{10}$$

where ω_0 and $\mathbf{k}_0$ are the frequency and wave vector of the incident wave, and $\mathbf{n}_0$ is the propagation direction of the incident wave. Here we do not discuss the effect of plasma polarization on the electromagnetic fields, which was justified in our previous article [18]. Under the action of the incident wave, the acceleration of an electron is given by

$$\dot{\mathbf{v}}(\tau) = -\frac{eE_0}{m_e}\left[\left(1 - \frac{1}{2}\frac{v^2}{c^2}\right)\mathbf{e}_0 + \frac{1}{c}\mathbf{v} \times (\mathbf{n}_0 \times \mathbf{e}_0) - \frac{1}{c^2}(\mathbf{v} \cdot \mathbf{e}_0)\mathbf{v}\right] \cos[\mathbf{k}_0 \cdot \mathbf{r}(\tau) - \omega_0 \tau] + O[(v/c)^3]. \tag{11}$$

Here we neglect those terms with the orders higher than $(v/c)^2$. For the sake of simplification, we assume that $\mathbf{e}_0$ is perpendicular to the scattering direction $\mathbf{n}_s$ in the following calculations, i.e., $\mathbf{e}_0 \cdot \mathbf{n}_s = 0$. This condition can easily be achieved by suitable experimental setup.

Substituting Eq. (11) into Eq. (8) and performing ensemble average, we can obtain the spectral power of the Thomson scattering via the procedure presented in our previous article [18], while the only difference is that the Klimontovich distribution function in this paper is defined as

$$F_e(\mathbf{r}, \mathbf{p}, \tau) = \sum_{i=1}^{N} \delta[\mathbf{r} - \mathbf{r}_i(\tau)] \delta[\mathbf{p} - \mathbf{p}_i(\tau)], \tag{12}$$

instead of $F_e(\mathbf{r}, \mathbf{v}, \tau)$ in Ref. 18. The spectral power is hence given by

$$\frac{d^2 P_{\mathbf{n},\omega_s}}{d\Omega d\omega_s} = \frac{1}{2\pi n_e} I_0 r_e^2 V_s n_e \int d^3p d^3p' \left(1 + \frac{1}{c}\Xi_1 + \frac{1}{c^2}\Xi_2\right) (\delta f_e^2)^{\mathrm{rel}}_{\mathbf{k},\omega,\mathbf{p},\mathbf{p}'}, \tag{13}$$

Here Ξ_1 and Ξ_2 are the first and second order corrections respectively given by

$$\Xi_1 = (\mathbf{n}_s - \mathbf{n}_0) \cdot (\mathbf{v} + \mathbf{v}'), \tag{14}$$

$$\Xi_2 = \mathbb{A} \colon (\mathbf{v}\mathbf{v} + \mathbf{v}'\mathbf{v}') + \mathbb{B} \colon \mathbf{v}\mathbf{v}'. \tag{15}$$

Here the velocities $\mathbf{v}$ and $\mathbf{v}'$ are the functions of $\mathbf{p}$ and $\mathbf{p}'$, respectively, and $\mathbb{A}$ and $\mathbb{B}$ are two tensors defined as

$$\mathbb{A} = -\frac{1}{2}\mathbb{I} + \mathbf{n}_s(\mathbf{n}_s - \mathbf{n}_0) - [1 - (\mathbf{n}_0 \cdot \mathbf{n}_s)]\mathbf{e}_0\mathbf{e}_0, \tag{16}$$

$$\mathbb{B} = (\mathbf{n}_s - \mathbf{n}_0)(\mathbf{n}_s - \mathbf{n}_0) + \left[1 - (\mathbf{n}_0 \cdot \mathbf{n}_s)^2\right] \mathbf{e}_0\mathbf{e}_0, \tag{17}$$

where $\mathbb{I}$ is the unit tensor of rank two. The function $(\delta f_e^2)^{\mathrm{rel}}_{\mathbf{k},\omega,\mathbf{p},\mathbf{p}'}$ in the integrand of Eq. (13) is the spectral density of the correlation function of the Klimontovich electron distribution functions, which is already obtained [26]. It should be pointed out that with inclusion of the relativistic effects $(\delta f_e^2)^{\mathrm{rel}}_{\mathbf{k},\omega,\mathbf{p},\mathbf{p}'}$ is different from the non-relativistic one $(\delta f_e^2)^{\mathrm{non}}_{\mathbf{k},\omega,\mathbf{p},\mathbf{p}'}$ presented in Ref. 27 because both fluctuating electric and magnetic fields have effects on particle fluctuations.

Introducing the notations,

$$\frac{1}{2\pi n_e}\int (\delta f_e^2)^{\mathrm{rel}}_{\mathbf{k},\omega,\mathbf{p},\mathbf{p}'} d^3p d^3p' = A(k,\omega), \tag{18a}$$

$$\frac{1}{2\pi n_e}\int \mathbf{v}(\delta f_e^2)^{\mathrm{rel}}_{\mathbf{k},\omega,\mathbf{p},\mathbf{p}'} d^3p d^3p' = B(k,\omega)\frac{\mathbf{k}}{k}, \tag{18b}$$

$$\frac{1}{2\pi n_e}\int (\mathbf{v}\mathbf{v} + \mathbf{v}'\mathbf{v}')\,(\delta f_e^2)^{\mathrm{non}}_{\mathbf{k},\omega,\mathbf{p},\mathbf{p}'} d^3p d^3p' = C_1(k,\omega)\frac{\mathbf{k}\mathbf{k}}{k^2} + D_1(k,\omega)\left(\mathbb{I} - \frac{\mathbf{k}\mathbf{k}}{k^2}\right), \tag{18c}$$

$$\frac{1}{2\pi n_e}\int \mathbf{v}\mathbf{v}'(\delta f_e^2)^{\mathrm{non}}_{\mathbf{k},\omega,\mathbf{p},\mathbf{p}'} d^3p d^3p' = C_2(k,\omega)\frac{\mathbf{k}\mathbf{k}}{k^2} + D_2(k,\omega)\left(\mathbb{I} - \frac{\mathbf{k}\mathbf{k}}{k^2}\right), \tag{18d}$$

Eq. (13) can now be written as

$$\frac{d^2P_{n,\omega_s}}{d\Omega d\omega_s} = I_0 r_e^2 N_s \left(\sigma_1 + \sigma_2 + \sigma_3 + \sigma_4\right), \tag{19}$$

where

$$\sigma_1 = A(k,\omega) \tag{20a}$$

$$\sigma_2 = \frac{2}{c}(\mathbf{n}_s - \mathbf{n}_0)\cdot\frac{\mathbf{k}}{k}B(k,\omega), \tag{20b}$$

$$\sigma_3 = \frac{1}{c^2}\left\{\frac{(\mathbf{k}\cdot\mathbf{n}_s)\left[\mathbf{k}\cdot(\mathbf{n}_s-\mathbf{n}_0)\right]}{k^2}(C_1 - D_1) + [1-(\mathbf{n}_s\cdot\mathbf{n}_0)]D_1 - \frac{C_1+2D_1}{2}\right\}, \tag{20c}$$

$$\sigma_4 = \frac{1}{c^2}\left\{\frac{\left[\mathbf{k}\cdot(\mathbf{n}_s-\mathbf{n}_0)\right]^2}{k^2}(C_2 - D_2) + (1-\mathbf{n}_s\cdot\mathbf{n}_0)\left(3+\mathbf{n}_s\cdot\mathbf{n}_0\right)D_2\right\}. \tag{20d}$$

It should be pointed out that Eqs. (18) are valid only if the fluctuations in the plasma are statistically isotropic.

III. THE RELATIVISTIC CORRECTIONS

The integral $A(k,\omega)$ in Eq. (18a) is actually the auto-correlation function of electron density, which essentially has the same form with that of a non-relativistic plasma,

$$A(\omega,k) \equiv S^{\rm rel}(\omega,k) = \frac{1}{n_e}\left(\left|1-\frac{\chi_e}{\epsilon_l}\right|^2 F_e + Z^2\left|\frac{\chi_e}{\epsilon_l}\right|^2 F_i\right), \tag{21}$$

where ϵ_l is the relativistic longitudinal permittivity of the plasma, and χ_e is the relativistic electron susceptibility, and $F_{e,i}$ are given by

$$F_{e,i} = \int f_{e,i}(\mathbf{p})\delta(\omega - \mathbf{k}\cdot\mathbf{v})d^3p. \tag{22}$$

Here, $f_{e,i}$ are the momentum distribution functions of the electrons and ions, $\delta(x)$ is the $\delta-$function. The relativistic dynamic form factor Eq. (21) is different from the non-relativistic Eq. (4) through the relativistic momentum distribution functions instead of the non-relativistic ones.

For a relativistic plasma, the momentum distribution function of the electrons is given by the Maxwell-Jüttner function,

$$f_e(p) = \frac{n_e\alpha^{-1}}{4\pi m_e^3c^3K_2(\alpha^{-1})}\exp\left[-\alpha^{-1}(1+p^2/m_e^2c^2)^{1/2}\right], \tag{23}$$

where $\alpha = T_e/m_ec^2$, T_e is the electron temperature, and $K_2(x)$ is the modified Bessel function. With the relativistic distribution function of Eq. (23), the function F_e can be written as

$$F_e = \frac{n_e}{kv_e}\frac{\alpha^{1/2}}{2K_2(\alpha^{-1})}\left(\frac{1}{1-2\alpha\xi^2} + \frac{2\alpha}{\sqrt{1-2\alpha\xi^2}} + 2\alpha^2\right)\exp\left(-\frac{\alpha^{-1}}{\sqrt{1-2\alpha\xi^2}}\right), \tag{24}$$

where $\xi = \omega/\sqrt{2}kv_e$, and $v_e = (T_e/m_e)^{1/2}$ is the electron thermal velocity. The function F_e becomes zero when $2\alpha\xi^2 \geqslant 1$ because no particle can move faster than the light speed. In Fig. 1, we compare the function F_e with the non-relativistic function F_{e0} of Eq. (5) in the case of $\alpha = 0.01$. As seen in Fig. 1, the two functions are different from each other only when ω/k becomes closer to the light speed, and the two curves are not separable when $\xi < 2$.

The real part of the full relativistic electron susceptibility χ_e is very complicated and no analytical form is available at present. The detailed discussions on this function can be found in the recent articles on the linear wave dispersion relation of relativistic plasmas [28, 29]. For laser-produced plasmas, the parameter α is usually less than 0.01. Hence the relativistic correction to the real part of χ_e is small. The real part of χ_e can be approximately written as (seeing Appendix A)

$$\mathrm{Re}\,\chi_e = \mathrm{Re}\,\chi_{e0} + \frac{\alpha}{k^2\lambda_D^2}\left[\left(\frac{5}{4} - \frac{3}{2}\xi^2\right)\xi^2 + \left(\frac{1}{8} + 2\xi^2 - \frac{3}{2}\xi^4\right)\xi\,\mathrm{Re}\,Z(\xi)\right], \tag{25}$$

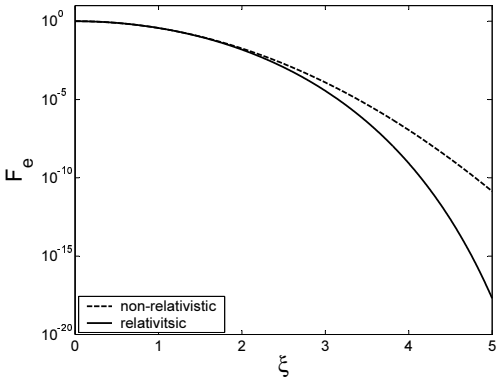

FIG. 1: The comparison between F_e and F_{e0} in the case of the parameter $\alpha = 0.01$, i.e., $T_e = 5.11$ keV.

where $\mathrm{Re}\,\chi_{e0} = (k\lambda_D)^{-2}[1 + \xi\,\mathrm{Re}(\xi)]$ is the real part of the non-relativistic electron susceptibility, $\mathrm{Re}\,Z(x)$ is the real part of the plasma dispersion function. When $\xi \gg 1$, the asymptotic expansion of $\mathrm{Re}\,\chi_e$ is given by

$$\mathrm{Re}\,\chi_e = -\frac{1}{(k\lambda_D)^2}\left[\left(1 - \frac{5}{2}\alpha\right)\frac{1}{2\xi^2} + (1 - 8\alpha)\,\frac{3}{4\xi^4}\right] + \cdots . \tag{26}$$

With Eq. (26), we can obtain the relativistic correction to the dispersion relation of the electron plasma wave,

$$\omega^2 = \omega_p^2\left(1 - \frac{5}{2}\alpha\right) + 3k^2v_e^2, \tag{27}$$

where $\omega_p = (4\pi n_e e^2/m_e)^{1/2}$ is the Langmiur frequency. Equation (27) is the same as that obtained by Buti [30]. As indicated by Bergman and Eliasson [28], the Eq. (26) is accurate enough when $\alpha \lesssim 0.01$.

The imaginary part of χ_e can be analytically calculated, and is given by

$$\mathrm{Im}\,\chi_e = \frac{1}{k^2\lambda_D^2}\frac{\sqrt{2}\alpha}{2K_2(\alpha^{-1})}\xi\left(\frac{1}{1 - 2\alpha\xi^2} + \frac{2\alpha}{\sqrt{1 - 2\alpha\xi^2}} + 2\alpha^2\right)\exp\left(-\frac{\alpha^{-1}}{\sqrt{1 - 2\alpha\xi^2}}\right). \tag{28}$$

When $2\alpha\xi^2 \geqslant 1$, i.e., $\omega/k \geqslant c$, $\mathrm{Im}\,\chi_e$=0. In this case, the Landau damping of the electron plasma waves disappears because no particles can catch up with the wave with a phase velocity faster than the light speed.

Since the relativistic corrections are proportional to $(v/c)^2$ in the case of $(v/c)^2 \ll 1$, the integrals of $C_{1,2}(\omega, k)$ and $D_{1,2}(\omega, k)$, which appears in the terms proportional to $1/c^2$, can be calculated with the non-relativistic spectral density $(\delta f_e^2)^{\mathrm{non}}_{\mathbf{k},\omega,\mathbf{p},\mathbf{p}'}$. The calculations are straight, and similar with those presented in the Appendix of Ref. 18. Since the first correction term is the order of 1, the integral $B(\omega, k)$ in the first correction term should also be calculated with the relativistic spectral density $(\delta f_e^2)^{\mathrm{rel}}_{\mathbf{k},\omega,\mathbf{p},\mathbf{p}'}$. Its calculation is also similar with that presented in Ref. 18. These integrals are given by,

$$B = \frac{\omega}{k}S^{\mathrm{rel}}(\omega, k), \tag{29}$$

$$C_1 = 2\frac{\omega^2}{k^2}S(k,\omega) + \frac{\omega_p^2}{k^2}\frac{1}{n_e}\left\{\frac{\chi_{e0}^* + \chi_{e0}}{|\epsilon_{l0}|^2}\sum_{\alpha=e,i}(e_\alpha/e)F_{\alpha 0} - \left(\frac{1}{\epsilon_{l0}} + \frac{1}{\epsilon_{l0}^*}\right)F_{e0}\right\}, \tag{30}$$

$$D_1 = 2\frac{T_e}{m_e}S(k,\omega), \tag{31}$$

$$C_2 = \frac{\omega^2}{k^2}S(\omega, k), \tag{32}$$

$$D_2 = \frac{T_e}{m_e}F_{e0}, \tag{33}$$

where ϵ_{l0} is the non-relativistic permittivity of the plasma, and F_{a0} are the non-relativistic limits of the functions F_α defined by Eq. (22).

In Eq. (20b), the unit vector $\mathbf{k}/k$ should be approximated as

$$\frac{\mathbf{k}}{k} = \frac{1}{\sqrt{2(1-\mathbf{n}_0\cdot\mathbf{n}_s)}}\left[(\mathbf{n}_0-\mathbf{n}_s)+\frac{\omega}{2\omega_0}(\mathbf{n}_0+\mathbf{n}_s)\right]. \tag{34}$$

Then the second term in Eq. (19) can be approximately written as

$$\frac{2}{c}B(\omega,k)(\mathbf{n}_s-\mathbf{n}_0)\cdot\frac{\mathbf{k}}{k} = \left(\frac{2\omega}{\omega_0}-\frac{\omega^2}{\omega_0^2}\right)S^{\rm rel}(\omega,k).$$

In Eqs. (20c) and (20d), the unit vector $\mathbf{k}/k$ can be approximated as

$$\frac{\mathbf{k}}{k} = \frac{(\mathbf{n}_0-\mathbf{n}_s)}{\sqrt{2(1-\mathbf{n}_0\cdot\mathbf{n}_s)}}. \tag{35}$$

Thus we have

$$\frac{(\mathbf{k}\cdot\mathbf{n}_s)\,[\mathbf{k}\cdot(\mathbf{n}_s-\mathbf{n}_0)]}{k^2} = 1-\mathbf{n}_s\cdot\mathbf{n}_0,$$

$$\frac{[\mathbf{k}\cdot(\mathbf{n}_s-\mathbf{n}_0)]^2}{k^2} = 2(1-\mathbf{n}_s\cdot\mathbf{n}_0).$$

Finally, we obtain the spectral power of the Thomson scattering with the corrections of $(v/c)^2$,

$$\begin{aligned}\frac{d^2P_{\mathbf{n},\omega_s}}{d\Omega d\omega_s} = r_e^2 I_0 V_s n_e \Bigg\{ & S^{\rm rel}+\frac{2\omega}{\omega_0}S^{\rm rel}-\frac{\omega^2}{\omega_0^2}S^{\rm rel} \\ & +\frac{1}{c^2}\left[2(C_1+2C_2-D_1)\sin^2\frac{\theta_s}{2}-\frac{C_1+2D_1}{2}+D_2\sin^2\theta_s\right]\Bigg\},\end{aligned} \tag{36}$$

where θ_s is the scattering angle given by $\cos\theta_s = \mathbf{n}_s\cdot\mathbf{n}_0$.

In Figure 2(a) we plot the three spectral powers respectively given by Eqs. (1), (6) and (36). The parameters that we take in the calculations are the same as those used by Glenzer et al [6], i.e., $T_e = 2$ keV, $n_e = 2.1\times10^{20}$ cm^{-3} , $\lambda_0 = 0.5266$ μm, and $\theta_s = 104^\circ$. Equation (7) is used in the computations of Eqs. (6) and (36), but Eq. (2b) is used in the computation of Eq. (1). It is shown in Fig. 2(a) than the maximum intensity given by the corrected formula of Eq. (36) is higher than that given by Eq. (6), and that the peak position predicted by Eq. (36) is a little blue shifted in comparison with that by Eq. (6). The physical reason is that both the damping rate and frequency of electron plasma waves become a little smaller when relativistic effect is included [28, 29]. However, the profile of Eq. (36) is rather close to that of Eq. (6). This result means that the relativistic corrections are not significant in the case of this example. In order to show the relativistic effects more clearly, we plot in Fig. 2(b) the profiles of the three equations in the case of $T_e = 3$ keV, $n_e = 4\times10^{20}$ cm^{-3}, $\lambda_0 = 0.5266$ μm, and $\theta_s = 104^\circ$. In Fig. 2(b), we can clearly see the difference between the first order theory and the second order one.

We pointed out in our previous article [18] that in comparison with the fitting results obtained with the uncorrected theory the inferred electron temperature could be significantly underestimated but the inferred electron density is nearly unchanged when the corrections of v/c to the Thomson scattering are included. We now investigate the influences of the relativistic corrections on the inferring of the plasma parameters. We still use the uncorrected theory to generate an artificial scattering spectrum, and fit it with Eq. (6) and Eq. (36), respectively. One of the comparison is shown in Fig. 2(a), where the plasma parameters for the dashed line are $T_e = 2$ keV, $n_e = 2.1\times10^{20}$ cm^{-3} while those for the first order fitting curve (dotted line) are $T_e = 2.7$ keV, $n_e = 2.15\times10^{20}$ cm^{-3}, and for the second order fitting curve (solid line) are $T_e = 2.75$ keV, $n_e = 2.15\times10^{20}$ cm^{-3}. Another is shown in Fig. 3(b), where the plasma parameters for the dashed line are $T_e = 3$ keV, $n_e = 4\times10^{20}$ cm^{-3} while those for the first order fitting curve (dotted line) are $T_e = 4.44$ keV, $n_e = 4.08\times10^{20}$ cm^{-3}, and for the second order fitting curve (solid line) are $T_e = 4.48$ keV, $n_e = 4.10\times10^{20}$ cm^{-3}. From these results, we conclude that the first order corrected theory can very slightly underestimate the electron temperature.

Equation (36) is rather lengthy and complicated. For the sake of routine application, we can further simplify it. Noticing that the relativistic corrections are important only in the high-frequency part of a Thomson scattering

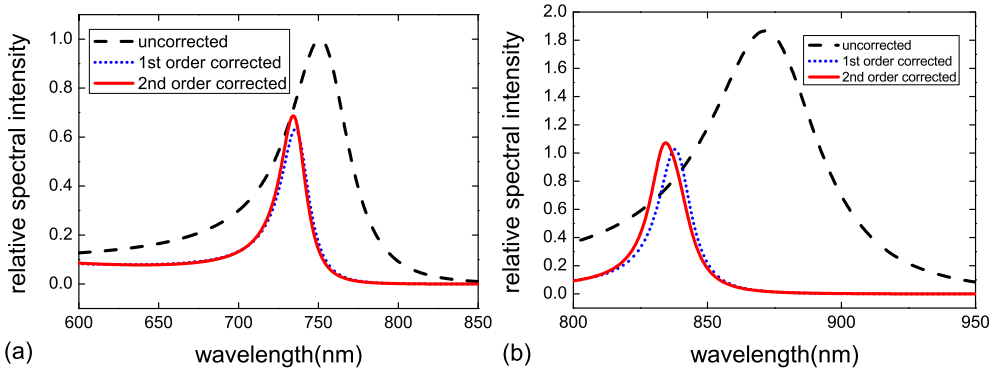

FIG. 2: (Color online) The profiles of the scattering spectral power, where the dashed line is the uncorrected result, the dotted line is the first order one, the solid line is the second order one. The parameters used in calculations are (a) $T_e = 2$ keV, $n_e = 2.1 \times 10^{20}$ cm^{-3} , $\lambda_0 = 0.5266$ μm, and $\theta_s = 104°$, and (b) $T_e = 3$ keV, $n_e = 4 \times 10^{20}$ cm^{-3} , $\lambda_0 = 0.5266$ μm, and $\theta_s = 104°$.

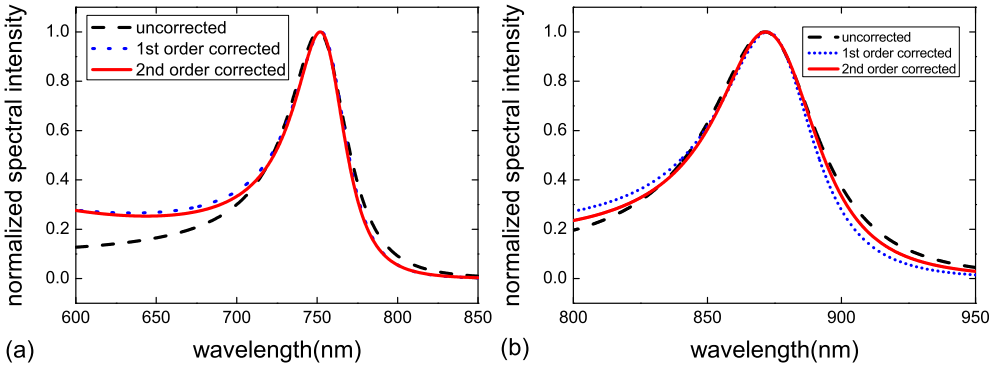

FIG. 3: (Color online) A fitting of the first and second order corrected theories to the uncorrected one, where the dashed line is the uncorrected result, the dotted line is the first order corrected one and the solid line is the second order corrected one. The plasma parameters used to calculate the uncorrected spectrum are (a) $T_e = 2$ keV, $n_e = 2.1 \times 10^{20}$ cm^{-3}, $\lambda_0 = 0.5266$ μm, and $\theta_s = 104°$; and (b) $T_e = 3$ keV, $n_e = 4 \times 10^{20}$ cm^{-3}, $\lambda_0 = 0.5266$ μm, and $\theta_s = 104°$.

spectrum, we can neglect the low-frequency response of the electrons that screen the ion motions in the plasma, i.e., we approximately have $\chi_i \approx 0$ and $F_i \approx 0$ when $\omega/kc_s \gg 1$ where c_s is the ion-acoustic speed of the plasma. In this case, the normal dynamic form factor can be written as

$$S(k,\omega) \approx \frac{1}{|\epsilon_{l0}|^2}\frac{1}{n_e}F_{e0}.$$

And C_1 and D_2 can be simplified,

$$C_1(k,\omega) \approx 2\frac{\omega^2}{k^2}\left(1-\frac{\omega_p^2}{\omega^2}\right)S(k,\omega),$$
$$D_2(k,\omega) \approx \frac{T_e}{m_e}|\epsilon_{l0}|^2 S(k,\omega).$$

With these approximations, Eq. (36) can be written as

$$\frac{d^2P_{\mathbf{n},\omega_s}}{d\Omega d\omega_s} = r_e^2 I_0 N_s \left\{\left[S^{\rm rel}(k,\omega)+\frac{2\omega}{\omega_0}S^{\rm rel}(k,\omega)\right]\right.$$
$$\left.+\left[\left(1-\frac{\omega_p^2}{\omega^2}\right)\left(1-\frac{1}{4\sin^2(\theta_s/2)}\right)\frac{\omega^2}{\omega_0^2}+\alpha\left(-4\sin^2\frac{\theta_s}{2}-1+|\epsilon_{l0}|\sin^2\theta_s\right)\right]S(k,\omega)\right\}. \quad (37)$$

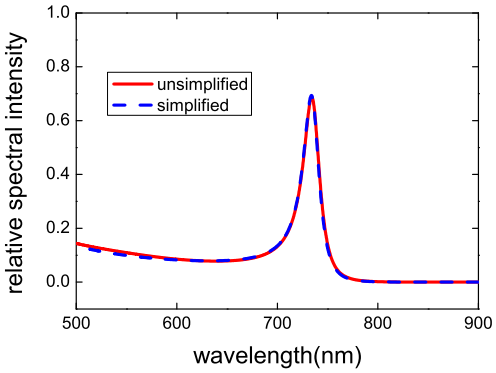

.

FIG. 4: (Color online) The comparison between the unsimplified result Eq. (36) and the simplified result Eq. (38). The parameters used in calculations are $T_e = 2$ keV, $n_e = 2.1 \times 10^{20}$ cm^{-3} , and $\lambda_0 = 0.5266$ μm, $\theta_s = 104^\circ$

Here we replace $(\omega/\omega_0)^2 S^{\rm rel}(k,\omega)$ with $(\omega/\omega_0)^2 S(k,\omega)$ since $(\omega/\omega_0)^2$ is small in the second order correction. The term proportional to α can be neglected because of $\alpha \lesssim 10^{-2}$ for the laser-produced plasmas with a temperature lower than 5 keV. The term proportional to $(1-\omega_p^2/\omega^2)$ can also be neglected because of $\omega \approx \omega_p$ around the maximum of a collective scattering spectrum. Therefore, we approximately have

$$\frac{d^2P_{\mathbf{n},\omega_s}}{d\Omega d\omega_s} = r_e^2 I_0 N_s \left(1+\frac{2\omega}{\omega_0}\right) S^{\rm rel}(k,\omega). \tag{38}$$

In Fig. 4, we plot the profiles of the scattering spectral power respectively given by Eq. (36) and Eq. (38). The parameters used in calculations are $T_e = 2$ keV, $n_e = 2.1 \times 10^{20}$ cm^{-3}, $\lambda_0 = 0.5266$ μm, and $\theta_s = 104^\circ$. As seen in this figure, the difference between the two curves is really very small, indicating that Eq. (38) is a good approximation of Eq (36). The accuracy of the approximation becomes worse when the plasma density becomes higher because the difference between $(\omega/\omega_0)^2 S^{\rm rel}(k,\omega)$ and $(\omega/\omega_0)^2 S(k,\omega)$ increases with the plasma density.

IV. CONCLUSION

In summary, we revisit the theory of collective Thomson scattering from high-temperature high-density plasmas. The spectral power of the Thomson scattering with inclusion of relativistic corrections of $(v/c)^2$ is derived with the aid of fluctuation theory. It is found that with inclusion of relativistic corrections the inferred electron temperature is even higher than that obtained with the theory with inclusion of the first order of v/c. The full formula Eq. (36) for the scattering spectrum with inclusion of relativistic corrections is rather lengthy and complicated. For the sake of practical use, a simplified formula Eq. (38) is given. A comparison between the two equations shows that the later well agrees with the former.

Acknowledgments

The authors are grateful to Prof. A. Bers of Massachusetts Institute of Technology for the discussions when the authors revise the manuscript.

This work is supported by Natural Science Foundation of China (Nos. 10625523, 10676033), and National Basic Research Program of China under Grant No. 2008CB717800.

APPENDIX A: THE DERIVATION OF EQ. (25)

The real part of relativistic electron susceptibility can be written as [30]

$$\mathrm{Re}\,\chi_e = \frac{1}{k^2\lambda_D^2}\left[1+\frac{\omega}{kc}\frac{\alpha^{-1}}{4K_2(\alpha^{-1})}\int_0^\infty \exp\left(-\alpha^{-1}\cosh x\right)\ln\frac{(\tanh x-\omega/kc)^2}{(\tanh x+\omega/kc)^2}\sinh x\cosh^2 x dx\right]. \tag{A1}$$

After integrating by part, we have

$$\mathrm{Re}\,\chi_e = \frac{1}{k^2\lambda_D^2}\left\{1+\frac{\omega}{kc}\frac{1}{4K_2(\alpha^{-1})}\int_0^\infty e^{-\alpha^{-1}\cosh x}\frac{d}{dx}\left[\ln\frac{(\tanh x-\omega/kc)^2}{(\tanh x+\omega/kc)^2}\cosh^2 x\right]dx\right\}. \tag{A2}$$

Introducing a new variable $t=\alpha^{-1}\cosh x$, we can rewrite the second term of Eq. (A2) as

$$\frac{\omega}{kc}\frac{\alpha}{K_2(\alpha^{-1})\exp(\alpha^{-1})}\int_0^\infty e^{-t}\left\{-\frac{1}{\sqrt{2\alpha t+\alpha^2t^2}}\frac{(\omega/kc)}{(\omega/kc)^2-(2\alpha t+\alpha^2t^2)/(1+\alpha t)^2}\right.$$
$$\left.+\frac{(1+\alpha t)}{2}\ln\frac{[\sqrt{(2\alpha t+\alpha^2t^2)}/(1+\alpha t)-\omega/kc]^2}{[\sqrt{(2\alpha t+\alpha^2t^2)}/(1+\alpha t)+\omega/kc]^2}\right\}dt.$$

Due to the rapid decreasing factor $\exp(-t)$ in the integrand, the important contribution to the integral comes from $t<1$. When $\alpha\ll 1$, we can expand the bracketed part in the integrand in series of α, and obtain

$$\mathrm{Re}\,\chi_e = \frac{1}{k^2\lambda_D^2}\left\{1+\frac{\sqrt{2\alpha}\xi^2}{K_2(\alpha^{-1})\exp(\alpha^{-1})}\int_0^\infty e^{-x^2}\left[\frac{1}{x^2-\xi^2}\right.\right.$$
$$\left.\left.+\ \alpha\left(\frac{2}{(x^2-\xi^2)}-\frac{x^2}{4(x^2-\xi^2)}+\frac{3x^4}{2(x^2-\xi^2)^2}\right)\right]\right\}.$$

Noticing that the real part of the plasma dispersion function can be written as

$$\mathrm{Re}\,Z(\xi)=\frac{2\xi}{\sqrt{\pi}}\int_0^\infty\frac{1}{x^2-\xi^2}e^{-x^2}dx.$$

we have

$$\mathrm{Re}\,\chi_e=\mathrm{Re}\,\chi_{e0}+\frac{\alpha}{k^2\lambda_D^2}\left[\left(\frac{5}{4}-\frac{3}{2}\xi^2\right)\xi^2+\left(\frac{1}{8}+2\xi^2-\frac{3}{2}\xi^4\right)\xi\,\mathrm{Re}\,Z(\xi)\right] \tag{A3}$$

[1] D. E. Evans and J. Katzenstein, Rep. Prog. Phys. **32**, 207 (1969).
[2] J. Sheffield, *Plasma Scattering of Electromagnetic Radiation* (Academic Press, New York, 1975).
[3] B. La Fontaine, H. A. Baldis, D. M. Villeneuve, J. Dunn, G. D. Enright, J. C. Kieffer, H. Pépin, M. D. Rosen, D. L. Matthews, and S. Maxon, Phys. Plasmas **1**, 2329 (1994).
[4] S. H. Glenzer, C. A. Back, K. G. Estabrook, R. Wallace, K. Baker, B. J. MacGowan, B. A. Hammel, R. E. Cid, and J. S. De Groot, Phys. Rev. Lett. **77**, 1496 (1996).
[5] S. H. Glenzer, C. A. Back, L. J. Suter, M. A. Blain, O. L. Landen, J. D. Lindl, B. J. MacGowan, G. F. Stone, R. E. Turner, and B. H. Wilde, Phys. Rev. Lett. **79**, 1277 (1997).
[6] S. H. Glenzer, W. Rozmus, B. J. MacGowan, K. G. Estabrook, J. S. De Droot, G. B. Zimmerman, H. A. Baldis, J. A. Harte, R. W. Lee, E. A. Williams, and B. G. Wilson, Phys. Rev. Lett. **82**, 97 (1999).
[7] B. Bai, J. Zheng, W. D. Liu, C. X. Yu, X. H. Jiang, X. D. Yuan, W. H. Li, and Z. J. Zheng, Phys. Plasmas **8**, 4144 (2001).
[8] Z. B Wang, J. Zheng, B. Zhao, C. X. Yu, X. H. Jiang, W. H. Li, S. Y. Liu, Y. K. Ding, and Z. J. Zheng, Phys. Plasmas **12**, 082703 (2005).
[9] Q. Z. Yu, J. Zhang, Y. T. Li, X. Lu, J. Hawreliak,J. Wark, D. M. Chambers, Z. B. Wang, C. X. Yu, X. H. Jiang, W. H. Li, S. Y. Liu, and Z. J. Zheng, Phys. Rev. E **71**, 046407 (2005).
[10] D. H. Froula, P. Davis, L. Divol, J. S. Ross, N. Meezan, D. Price, S. H. Glenzer, and C. Rousseaux, Phys. Rev. Lett. **95**, 195005 (2005).
[11] D. H. Froula, J. S. Ross, B. B. Pollock, P. Davis, A. N. James, L. Divol, M. J. Edwards, A. A. Offenberger, D. Price, R. P. J. Town, G. R. Tynan, and S. H. Glenzer, Phys. Rev. Lett. **98**, 135001 (2007).
[12] J. Zheng, C. X. Yu, and Z. J. Zheng, Phys. Plasmas **4**, 2736 (1997).
[13] Z. J. Liu, J. Zheng, and C. X. Yu, Phys. Plasmas **9**, 1073 (2002).
[14] J. F. Myatt, W. Rozmus, V. Y. Bychenkov, and V. T. Tikhonchuk, Phys. Rev. E **57**, 3383 (1998).
[15] J. Zheng, C. X. Yu, and Z. J. Zheng, Phys. Plasmas **6**, 435 (1999).
[16] W. Rozmus, S. H. Glenzer, K. G. Estabrook, H. A. Baldis, and B. J. MacGowan, Astrophys. J., Suppl. Ser. **127**, 459 (2000).
[17] Z. B. Wang, B. Zhao, J. Zheng, G. Y. Hu, W. D. Liu, C. X. Yu, X. H. Jiang, W. H. Li, S. Y. Liu, Y. K. Ding, and Z. J. Zheng, Acta Phys. Sin. **54**, 211 (in Chinese) (2005).

[18] J. Zheng and C. X. Yu, Plasma Phys. Control. Fusion **51**, 095009 (2009).
[19] R. A. Pappert, Phys. Fluids **6**, 1452 (1963).
[20] R. E. Pechacek and A. W. Trivelpiece, Phys. Fluids **10**, 1688 (1967).
[21] G. Ward and R. E. Pechacek, Phys. Fluids **15**, 2202 (1972).
[22] A. B. Kukushkin, Sov. J. Plasma Phys. **7**, 63 (1981).
[23] S. C. Chen and T. C. Marshall, Phys. Rev. Lett. 52, 425 (1984).
[24] O. Naito, H. Yoshida, and T. Matoba, Phys. Fluids B **5**, 4256 (1993).
[25] J. Lindl, Phys. Plasmas **2**, 3933 (1995).
[26] Yu. L. Klimontovich, *Kinetic Equations for Nonideal Gas and Nonideal Plasma* (Pergamon, Oxford, 1974).
[27] E. M. Lifshitz and L. P. Pitaevskii, *Physical Kinetics* (Pergamon, Oxford, 1981), Sect. 51.
[28] J. Bergman and B. Eliasson, Phys. Plasmas **8**, 1482 (2001).
[29] A. Bers, I. P. Shkarofsky, and M. Shourci, Phys. Plasmas **16**, 022104 (2009).
[30] B. Buti, Phys. Fluids **5**, 1 (1962).

Collisionless Shockwaves Formed by Counter-Streaming Laser-produced Plasmas

Y. T. Li[1], X. Liu[1], Y. Zhang[1], J. Y. Zhong[2], W. D. Zheng[3], Q. L. Dong[1], M. Chen[1], G. Zhao[2], Y. Sakawa[4], T. Morita[4], Y. Kuramitsu[4], T. N. Kato[4], H. Takabe[4], Yong-Joo Rhee[5], Y. Gu[6], J. Q. Zhu[6], and J. Zhang[1,7*]

[1]*Beijing National Laboratory for Condensed Matter Physics, Institute of Physics, Chinese Academy of Sciences, Beijing 100190, China*

[2]*National Astronomical Observatories, Chinese Academy of Sciences, Beijing 100012, China*

[3]*Institute of Applied Physics and Computational Mathematics, Beijing 100094, China*

[4]*Institute of Laser Engineering, Osaka University, 2-6 Yamada-oka, Suita, Osaka, 565-0871, Japan*

[5]*Laboratory for Quantum Optics, Korea Atomic Energy Research Institute, 1045 Daedeok Street Yuseong-gu, Daejon 305-353,Korea*

[6]*National Laboratory on High Power Lasers and Physics, Shanghai, 201800*

[7]*Department of Physics, Shanghai Jiao Tong University, Shanghai 200240, China*

Abstract: The interaction between two counter-streaming laser-produced plasmas is investigated with the high-power Shenguang II laser facility. The shockwaves observed in our experiment are believed to be excited by collisionless mechanisms. The dimensionless parameters calculated with the results suggest that it is possible to scale the observation to the supernova remnants by transformation and similarity criteria.

Subject key words: instabilities – plasmas – shock waves – supernova remnants

1. INTRODUCTION

Collisionless shockwave is one of the important phenomena in astrophysical plasmas (Ness et al. 1964; Sagdeev & Kennel 1991; McKee & Draine 1991), such as in solar wind and supernova remnants (SNRs) (He et al. 2007; Romagnani et al. 2008; Chen et al. 2007). It is believed that the dissipation process of the forward and the reverse shockwaves in SNRs is one of the mechanisms to generate high-energy charged particles and cosmic rays (e.g., Bell 1978; Blandford & Ostriker 1978; Axford et al. 1982; Krymsky 1977) . Those shocks are generally collisionless because the shock transition occurs on a length scale that is much shorter than particle mean free paths, i.e., Coulomb collisions between particles are not important for the shock formation.

Collisionless shockwaves can also be generated with high-power lasers in laboratories. Though the space and time scales of laser-produced plasmas are very

different with the astrophysical, the comparison of hydrodynamic and radioactive properties between them can throw light on the astrophysical processes through transformation and similarity criteria proposed by Ryutov et al. (1999), so that laboratory plasmas have been applied to understand astrophysical phenomena (Remington et al. 2006; Wei et al. 2008; Takabe et al. 2008). Drake (2000) has studied the formation of collisionless shocks in the laboratory relevant to such cosmic shocks, and discussed the constraints that must be met by experiments. Courtois et al. (2004) have tried to demonstrate the shocks of SNRs by adding a magnetic field in counter-streaming laser-produced plasmas. Romagnani et al. (2008) have observed the collisionless shockwaves in an interaction between laser-produced plasma and the ambient low-density plasma.

Recent simulations show that collisionless shockwaves are formed in the unmagnetized electron-ion counter-streaming plasmas (Kato & Takabe 2008; Takabe et al. 2008; Sorasio et al. 2006). In this paper, we present our experimental studies of the interactions of two counter-streaming plasmas produced by high power laser pulses. By carefully choosing the laser energy, thickness of the targets and distance between the targets, the collisionless shockwaves have been observed. Numerical simulations are used to interpret the observation.

2. EXPERIMENTAL SETUP

The experiments were carried out on Shenguang II (SG II) laser facility at National Laboratory on High Power Lasers and Physics, which can delivery a total energy of 2.0 kJ in 1 ns at 3ω (351nm). The experimental setup is shown in Fig. 1. The eight laser pulses of the SG II laser were divided into two bunches. Each bunch consisted of 4 laser pulses. Two separated CH foils were used as the targets. The two laser bunches were focused onto the facing surfaces of the CH foils to generate two counter-streaming plasmas. Compared with shining on the outside surfaces of the foils, shining on the facing surface could generate plasmas with high temperature, high velocity, low density and without solid grains. The diameter of the focal spot was 150 μm, giving a laser intensity of 5.7×10^{15} W cm^{-2}. Another SG II laser pulse (the 9th pulse) with a duration of 70 ps and wavelength of 526 nm (2ω) was used as a probe. The interactions of the two plasmas were diagnosed by a Nomarski interferometer and shadowgraph. A time series of snapshots were obtained by changing the delay between the probe and main pulses. Two pinhole cameras were also used to measure the focus spots on the CH targets.

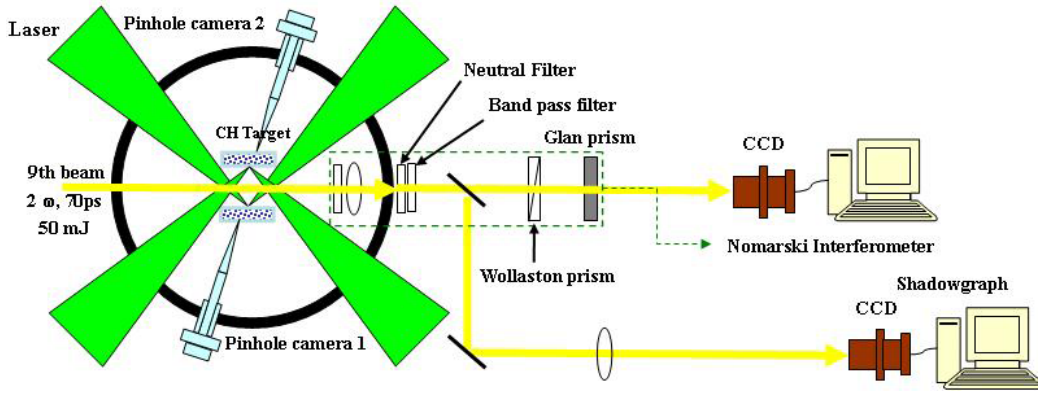

Fig. 1. (Color online) Schematic view of the experimental setup. Two 0.1 mm thick CH targets with a separation of 4.5 mm were placed at the center of the chamber. The interaction of the two counter-streaming plasmas was measured by a Nomarski interferometer and shadowgraph with a 2ω short laser probe. The magnification of the interferometer and shadowgraph was 1.53 and 1.86 respectively. Two pinhole cameras with a 20x magnification were used to monitor the focus on each target.

To make the interaction to be collisionless, low density and high flow velocity of the plasmas were necessary. The CH targets used in the experiment were two 2×2×0.1 mm Mylar foils with a separation of 4.5 mm. The thickness and the separation of the targets were designed according to our one-dimensional simulations, which indicated that such target configuration could produce required plasmas when the laser intensity was 5×10^{15} W cm^{-2}.

3. EXPERIMENTAL RESULTS AND DISCUSSIONS

The interferograms taken at delay times of 1 ns and 2 ns are shown in Fig. 2(a) and Fig. 2(b). The delay is defined as the time separation between the falling edges of the probe and the main pulses. The black regions correspond to the original target foils. Two bundles of the laser pulses strike on the facing surfaces of the foils, respectively. This results in two counter-streaming plasmas, which interact with each other around the center of the targets. At 1 ns, the fringes between the targets are shifted, indicating that the two plasmas have met with each other. At 2 ns, a clear density jump is observed at the middle.

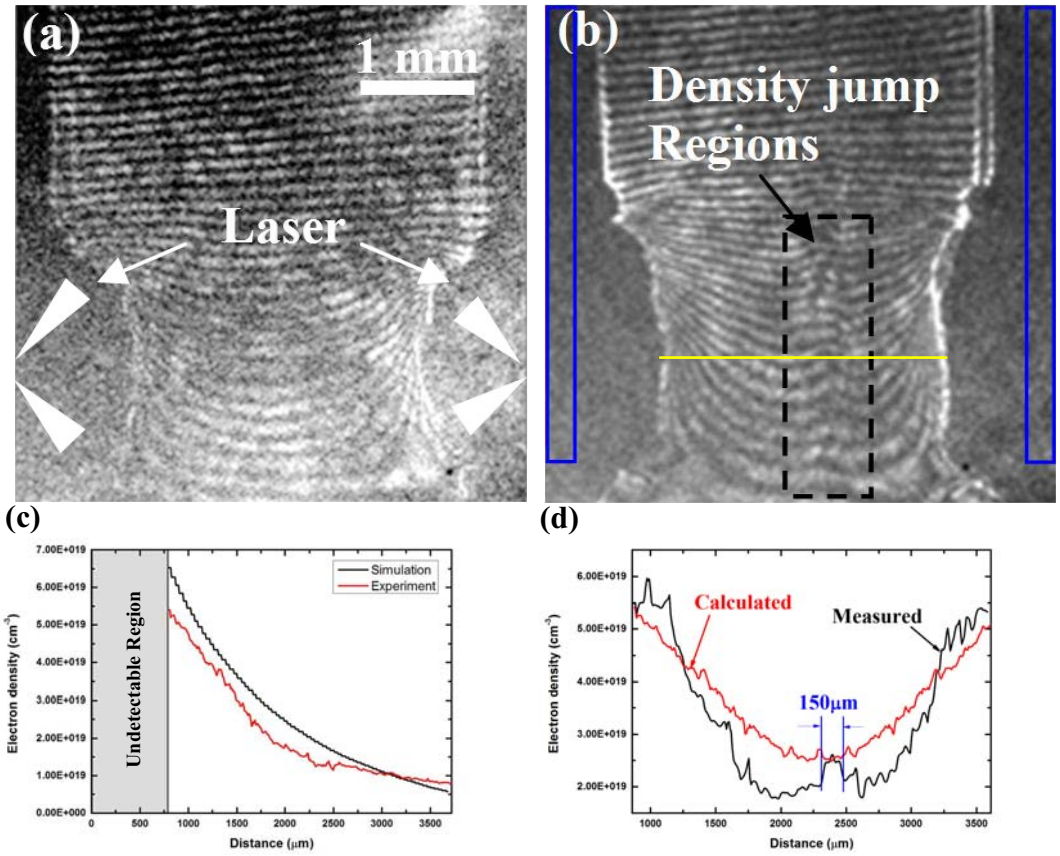

Fig. 2. (Color online) (a) and (b) are the interferograms obtained at 1 ns and 2 ns, respectively. (c) Experimental and simulated electron density distributions along the target normal for the

single target. (d) Comparison of measured density profile along the yellow line in (b) with that calculated by flipping left-to-right and adding with the experimental density profile of (c).

The expansion velocity and electron density of the plasmas before the collision were measured by irradiating only a target foil with one of the laser bunches. The density profile of the plasma was deduced using Abel inversion of the measured interferogram. The measured electron density distribution along the target normal direction is shown in Fig. 2(c). A two-dimensional radioactive hydrodynamical code using ALE (Arbitary Lagrange and Euler) method in the non-LTE (Local Thermal Equilibrium) condition, XRL2D, was also used to simulate the single plasma expansion (Zheng & Zhang 2008). The same laser and target parameters as the experimental were used in the simulations. The simulated density distribution is also shown in Fig. 2(c). We can see that the hydrodynamic simulations can reproduce well the expansion of single plasma.

Fig. 2(d) shows the comparison of observed density profile along the yellow line in (b) with that calculated by flipping the experimental profile of Fig. 2(c) left-to-right and added with the unflipped. No density peak is presented for the calculated profile. This is much different with the experimental one, which shows an obvious density peak with a width of ~150μm at the middle. Therefore, the comparison shows that the observed density jump indicates a shock generation, rather than a simple interpenetration of the two plasmas.

Using the formula of the ion-ion mean free path, λ_{ii} (Popovics et al. 1997),

$$\lambda_{ii} = \frac{m_i^2 v_{12}^4}{4\pi e^4 Z^4 n Ln\Lambda_{12}} \tag{1}$$

where n is the ion density in the plasma, v_{12} is the relative plasma expanding velocity, Z is the ionization state of the plasma, m_i is the ion mass, e is the elementary electric charge, and $Ln\Lambda_{12}$ is the so-called "Coulomb logarithm" (Sivukhin 1966). When $n\sim10^{19}cm^{-3}$, $v_{12}=2.2\times10^{8}cm\cdot s^{-1}$, $Z=6$ (taking Z as the maximum), $m_i=20.04\times10^{-27}kg$, $e=1.6\times10^{-19}C$, and $Ln\Lambda_{12}=6$, the low-limit of λ_{ii} is estimated to be ~1100 mm. The width of measured density jump is about 150μm. Since the width of the measured density jump is much shorter than λ_{ii}, the interaction of the two counter-streaming plasmas observed in our experiment is collisionless.

The generation of collisionless shockwaves has been studied with Particle-in-cell (PIC) simulations (Forslund et al. 1970; Kato & Takabe 2008; Mason 1972; Takabe et al. 2008). Their results show that two types of instabilities can generate collisionless shockwaves in counter-streaming plasmas. One is the electrostatic (ES) instability, which is driven by the large difference between the electron temperature and ion temperature, and the other is electromagnetic (EM) Weibel-type instability.

Figure 3(a) shows the distribution of the ratio of the electron temperature to ion temperature at 2.5 ns, simulated by our hydrodynamical code with the same conditions as the experimental. We can see that the electron temperature is much

higher than the ion temperature. This indicates that the observed collisionless shock waves in our experimental are probably excited by ES instability.

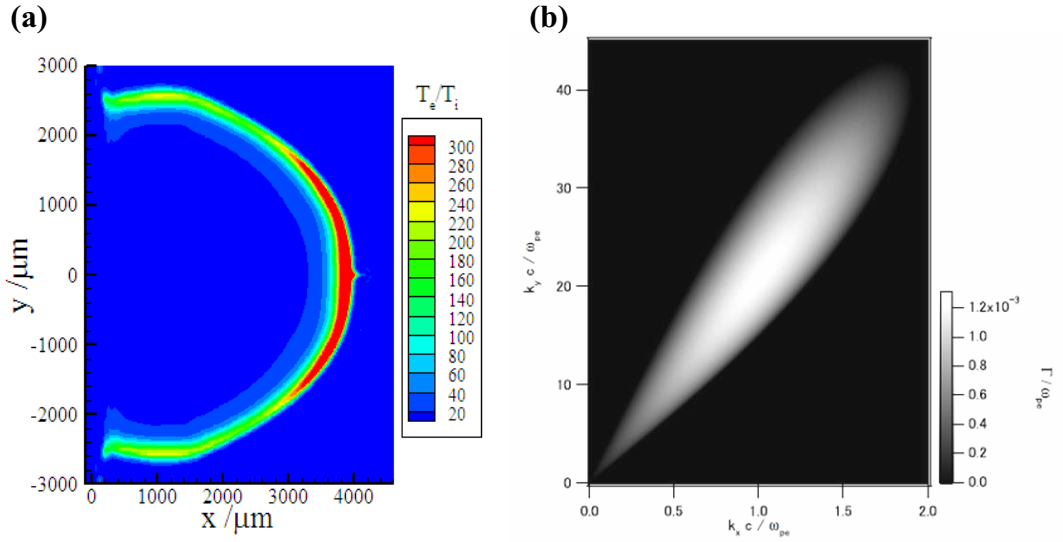

Fig. 3. (Color online) (a) The distribution of electron to ion temperature ratio at 2 ns, obtained with the hydrodynimical code. (b) The linear growth rates of the electrostatic ion-ion instability.

By using the parameters obtained from our experiments and hydrodynimical simulations, the linear dispersion relations of the ES instability are solved (Kato & Takabe 2010). The linear growth rate of the instability is shown in Fig. 3(b), when Te/Ti is 100. The results show that the ES instability can grow up rapidly and may play main role in the counter-streaming plasma interaction.

Our experimental results and theoretical analysis show that it is possible to generate the collisionless shocks in low density non-relativistic plasmas, which conditions are similar to the environment of supernovae and SNRs. A similarity principle that allows a direct scaling between the laboratory plasmas and the astrophysical objects such as SNRs has been proposed by Ryutov et al (1999). To do this, both the astrophysical and laboratory systems must behave as an ideal fluid, which is characterized by three parameters, the Reynolds number, *Re*, the Peclet number, *P*e, and the collisionality, ζ. ζ is defined as the ratio of mean free path to the system size. ζ must be larger than 1 to provide that the plasmas are collisionless. The Reynolds number and the Peclet number are also important, which force the plasmas to behave like a fluid and provide a dissipative effect. For the Euler equations to be valid and usable require that P_e and R_e must be very large,

$$P_e = \frac{\upsilon L}{\chi} >> 1, R_e = \frac{\upsilon L}{\chi_h} >> 1, \tag{2}$$

where υ is the characteristic fluid speed, L is the system size, χ is the thermal diffusivity and χ_h is the viscosity, respectively. If the three conditions for ζ, *Re* and

*P*e are satisfied, the similarity of the laboratory system to the astrophysical is compared by Euler number, *Eu*, and Mach number, *M*. The Euler number provides that the Euler equations are invariant under Euler transformation. The Mach number provides that a shock is formed. They can be obtained with the equations $Eu = \upsilon(\rho/p)^{1/2}$ and $M \approx U_f(\rho/p)^{1/2}$, where p is the plasma pressure, ρ is the mass density, and U_f is the bulk fluid speed (Courtois et al. 2004). Table 1 gives the parameters of our experiment at 2 ns and a young SNR (Decourchelle et al. 2000). We use the plasma parameters in the density jump regions where the collisionless shockwaves occurr, as shown in Fig. 2(b), to calculate those parameters in Table.1. One can see that the ζ, *Re* and *Pe* are all far larger than 1. This indicates that scaling the collisionless interaction in our experiments to the SNR is possible.

Table 1

Comparison of the dimensionless parameters of the shock in a SNR (Decourchelle et al. 2000) with the experimental at 2 ns.

Parameters	**SNR**	**Expt.**
Collisionality, ζ	2E6	4E2
Euler number, *Eu*	18	28
Mach number, *M*	16	14
Reynolds number, *Re*	1E13	2.5E6
Peclet number, *Pe*	1E11	4.5E3

4. CONCLUSIONS

The counter-streaming plasmas are generated by shining 8 laser pulses on two facing CH targets. In our experiment, the collisionless shockwaves were observed. Numercal simulations are used to analyze the experiment results, which indicate that the collisionless shockwaves may be excited by ES instability. The comparison of the dimensionless parameters of our experiment with those of SNR indicates that it is feasible to scale our measurements to the astrophysical objects.

Acknowledgements

This work is supported by the National Nature Science Foundation of China (Grant Nos. 10925421, 10720101075 and 10734130), and National Basic Research Program of China (973 Program) (Grant No.2007CB815101). The authors thank the staff of Shengguang II laser facility for operating the laser and target area.

References:

Axford, W. I., Leer, E., & McKenzie, J. F. 1982, A&A, **111**, 317
Bell, A. R. 1978, Mon. Not. R. Astron. Soc. **182**, 147
Blandford, R. D., & Ostriker, J. P. 1978, ApJL, **221**, L29
Chen, M., et al. 2007, Phys. Plasmas, **14**, 053102
Courtois, C., et al. 2004, Phys. Plasmas, **11**, 3386
Decourchelle, A., Ellison, D. C., & Ballet, J. 2000, ApJL, **543**, L57
Drake, R. P. 2000, Phys. Plasmas, **7**, 4690
Forslund, D. W., & Shonk, C. R. 1970, Phys. Rev. Lett., **25**, 1699

He, M. Q., Dong, Q. L., & Sheng, Z. M. 2007, Phys. Rev. E, **76**, 035402
Kato, T. N. & Takabe, H. 2008, ApJ, **681**, L93
Kato, T. N. & Takabe, H. 2010, Phys. Plasmas, **17**, 032114
Krymsky, G. F. 1977, Dokl. Akad. Nauk SSSR **234**, 1306
Mason, R. J. 1972, Phys. Fluids, **15**, 845
McKee, C. F. & Draine, B. T. 1991, Interstellar shock-waves, Science, **252**, 397
Ness, N. F., Searce, C. S., & Seek, J. B. 1964, J. Geophys. Res., **69**, 3531
Popovics, C. C., et al. 1997, Phys. Plasmas, **4**, 190
Remington, B. A., Drake, R. P., & Ryutov, D. D. 2006, Rev. Mod. Phys., **78**, 755
Romagnani, L., et al. 2008, Phys. Rev. Lett., **101**, 025004
Ryutov, D., et al. 1999, ApJ, **518**, 821
Sagdeev, R. Z., & Kennel, C. F. 1991, Sci. Am., **264**, 106.
Sivukhin, D. V. 1966, in *Reviews of Plasma Physics*, edited by M. A. Leontovich (Consultants Bureau, New York), Vol. 4, p. 93
Sorasio, G., et al. 2008, Phys. Rev. Lett., **96**, 045005
Takabe, H., et al. 2008, Plasma Phys. Control. Fusion, **50**, 124057
Wei, H. G., et al. 2008, ApJ, **683**,577
Zheng, W. D., & Zhang, G. P. 2008, Chinese Journal of Computational Physics, 25, 36

Periodic grating structures self-formed on metal surfaces under femtosecond laser pulse irradiation

Masaki Hashida, Shigeki Tokita, and Shuji Sakabe

Advanced Research Center for Beam Science, Institute for Chemical Research, Kyoto University, Gokasho, Uji, Kyoto 611-0011, Japan

Department of Physics, Graduate School of Science, Kyoto University, Kitashirakawa, Sakyo, Kyoto 606-8502, Japan

I. Introduction

Periodic grating structures self-formed inside or on the surface of materials under femtosecond-pulse laser irradiation have been found for insulators [1], semiconductors [2], and metals [3]. These structures have certain features that are not observed for picosecond- or nanosecond-pulse lasers. For metals irradiated with linear polarized laser light, the grating structures formed on the metal surface are oriented perpendicular to the laser polarization. The interspaces of the grating structures are shorter than the laser wavelength and depend on laser fluence [3–12]. However, the mechanism of self-formation is still under investigation. The structures depend on material properties and laser parameters (fluency, pulse duration, number of pulses, etc.). Even for the same metal, not all experimental results reported in the literature [3–27] can be directly compared because of differing parameters, such as the laser parameters. The relation between the type of metal and the interspaces of periodic grating structures has not been investigated, and therefore the amount of systematic experimental data is insufficient for discussing the mechanism at present.

We have reported that the formation of grating interspaces depends on laser fluence in the case of copper [3] with < 100-fs laser pulses. At laser fluence near the ablation threshold, the grating structures have an interspace of 300 nm, which is much shorter than the laser wavelength of 800 nm. The interspace increases up to about 700 nm as laser fluence increases. This dependence of the interspaces on laser fluence has been explained by Sakabe *et al*. on the basis of the parametric decay (stimulated Raman scattering) model [28]. In this model, a surface plasma waves are induced at the interface between free space (air) and either laser-produced plasma or metal plasma by parametric decay; in other words, the incident laser light decays into a surface plasma

wave and a scattered electromagnetic wave. Although the process whereby generation of the surface plasma wave leads to formation of periodic structures is not yet fully understood, we assume the following: when the plasma wave travels slowly, locally charged areas are periodically generated on the surface and positively charged areas are exploded toward free space by the Coulomb repulsive force (Coulomb explosion); consequently, a thin layer is ablated and the grating pattern is printed [29]. The wavenumber (wavelength) of the surface plasma wave induced on the surface depends on only the plasma frequency (electron density) of the surface plasma (see Fig. 3 of Ref. [28]). The ratio of the wavelength of the plasma wave to that of the laser light changes from 0.5 to 0.85 for plasma frequencies in the range of $0 < \omega_p / \sqrt{2} < \omega_L$, where ω_p and ω_L are the frequencies of the plasma and laser light, respectively. When the plasma electron density depends on laser fluence, the wavelength of the plasma wave in turn depends on laser fluence. The results reported in Ref. [3] for copper are well explained by this model; however, experimental data are too scarce at present for this model to be confirmed.

In the present study, we investigated by electron microscopy the state of surfaces irradiated with femtosecond laser pulses for Al, Au, Cu, Ti, Pt, Mo, and W metals. In addition, we evaluated the dependence of periodic structure interspaces on laser fluence to discuss the validity of the parametric decay model.

II. Experimental

To ablate metals, we used linear polarized laser pulses (160-fs pulse duration, 800-nm center wavelength, 10-Hz repetition rate) from a Ti:sapphire chirped-pulse amplification laser system (T^6-laser, ICR, Kyoto University). The root-mean-square fluctuation of pulse energy was ±0.3% [30]. In air, the laser pulses were focused onto the metals by a spherical lens with focal length of 100 mm (*F*/15). The focal spot was 45 μm in diameter. To avoid non-uniformity of structure in the irradiated area on the surface, the laser intensity distribution was adjusted to be spatially uniform. A super Gaussian profile was produced as follows. From a Gaussian profile pulse, the center part was cut away by an aperture of 1 mm in diameter, and the cut image was relayed to the target surfaces. The laser pulses were directed at normal incidence onto the target surface. The targets were Al, Au, Cu, Ti, Pt, Mo, and W metals, which had been mechanically polished. The roughness, as characterized by the arithmetic mean value,

was less than 2 nm for all metals. Through a pair of half-wave plates and two polarizers, the energy was varied in the range of 1.1–34 μJ, corresponding to fluence of 50–2100 mJ/cm^2. Energy (average of 500 pulses) was measured just before irradiating a target for each laser fluence. The number of irradiating pulses was 50 in all experiments. The irradiated spots were separated by more than 100 μm. Laser-produced surface structures were examined by scanning electron microscopy (JSM-5560 made in JEOL). The periodic grating interspace was determined by reading the peak value in the frequency domain after taking the Fourier transform for the 20 μm × 15 μm area of the SEM image, which is equivalent to the laser irradiated area on the targets. The resolution of the present measurements of the periodic spacing was better than 34 nm. The interspace of the grating structure was obtained by analyzing a set of 10 irradiated spots on a metal surface. Figure 1 shows typical SEM images and the corresponding Fourier transform spectra. To evaluate the ablation rate, the crater produced by 200 laser pulses was measured by confocal laser scanning microscopy (HL-150, Lasertec).

III. Results and discussion

Self-formation of periodic structures was not observed for Al, Au, and Cu metals, but was observed for Ti, Pt, Mo, and W metals. Here, we must make particular note of Cu metal. As reported in Ref. [3], periodic structures clearly formed on Cu, and the interspaces depended on laser fluence. In the present experiments, self-formation of periodic structures was not observed. We discuss these findings later.

Figure 2 shows the dependence of the periodic structure interspaces on laser fluence for Ti, Pt, Mo, and W metals. Al, Au, and Cu are excluded from the following discussion as no periodic structures were observed for these metals. The upper limit on the laser fluence at which the periodic structures are formed can be seen; let us define this fluence as F_{M}. The laser fluence in Fig. 2 is normalized by the fluence F_{M} (see Table 1 for F_M of each metal). As the laser fluence increases, the periodic interspace increases up to about 700 nm for all metals, and this maximum interspace is obtained at the fluence F_{M}.

Let us compare these experimental results with the predictions from the model of plasma wave induction by parametric decay of laser light [28]. Here, the model is

briefly described. The parametric process of photon → photon + plasmon can occur on a plasma surface as well as in a bulk plasma (i.e., stimulated Raman scattering). The parametric conditions of $\omega_L = \omega_2 + \omega_{SP}$ and $\mathbf{k}_L = \mathbf{k}_2 + \mathbf{k}_{SP}$, where the subscripts L, 2, and SP indicate the incident laser light, scattered light, and surface plasma wave, respectively, are reduced to

$$\omega_L - \omega_{SP} = ck_{SP} - ck_L, \quad \omega_L = ck_L,$$

$$\omega_{SP}{}^2 = c^2 k_{SP}{}^2 + \frac{1}{2}\omega_p{}^2 - \left(c^4 k_{SP}{}^4 + \frac{1}{4}\omega_p{}^2\right)^{1/2}.$$

The wavenumber of the plasma wave induced by the parametric process can be related to the plasma frequency, and the k_L/k_{SP} ratio (= λ_{SP}/λ_L; λ is the wavelength) changes from 0.5 to 0.85 for plasma frequencies in the range of $0 < \omega_p/\sqrt{2} < \omega_L$, where the plasma wavenumber increases as the plasma frequency decreases. As mentioned above, assuming that the self-formation is induced by the plasma wave, the grating spaces correspond to the wavelength of the induced plasma wave, and the fluence dependence of the interspaces can be reduced to plasma density dependence. The dependence of the surface electron density n_{es} on the laser fluence F_L can be interpreted as follows. The electron density n_e of the plasma bulk produced on the surface by the laser is proportional to the laser energy: $n_e \propto F_L$. The heated plasma bulk with temperature T_e expands at the sonic speed $c_s = \sqrt{k_B T_e / m}$, and the surface electron density decreases from the bulk density as n_e/c_s, and the temperature is proportional to the laser energy: $T_e \propto F_L$. Therefore, the surface electron density is related to the laser fluence as $n_{es} \propto n_e/c_s \propto n_e/T^{1/2} \propto F_L{}^{1/2}$. It is reasonable to assume that the plasma frequency is $\omega_p = \sqrt{2}\omega_L$ for the laser fluence F_M since no grating structures are produced at laser fluence over F_M. In this case, n_{es} [cm^{-3}] = $3.5\times10^{21}(F_L/F_M)^{1/2}$. Applying this expression together with $\omega_p = \sqrt{4\pi n_{es} e^2/m}$ to the dependence of λ_{SP}/λ_L on ω_p, the spatial dependence of the laser fluence is obtained. This relation is shown as a solid line in Fig. 2. For each metal, the experimental results agree reasonably well with this model, although there is disagreement in the relatively low fluence range. This disagreement is considered to arise from non-uniformity of ablation. At laser fluence near the ablation threshold, the amount of ablated plasma is too small to construct a uniform plasma surface. The measured ablation rate is shown in Fig. 3. The threshold of nanostructure formation can be defined for an ablation rate less than several nanometers per pulse.

For such a thin ablated layer, a uniform plasma surface is difficult to form. Here, let us define F_{10nm} as the fluence at which a 10-nm layer is ablated. The values of F_{10nm} are listed in Table 1. As shown in Fig. 2, the model is in fairly good agreement with the experimental results in the fluence range of $F_{10nm} < F_L < F_M$, and a common fluence dependence of the periodic grating interspaces can be found for self-formation induced by femtosecond laser pulses for all metals. These experimental results indicate that the interspaces of the self-formed periodic structure depend not on metal characteristics, but rather on the density of the surface plasma produced by a laser pulse. For high laser fluence ($F_L > F_M$), the plasma expands too greatly for a clear surface to be constructed, or the plasma density is too high; in such cases, a surface plasma wave is not produced. Now, let us return our attention to the metals for which self-formation of periodic structures was not observed. Metals such as Al and Au, which have low melting points, easily form gas plasmas, and thus F_M is not defined. For Cu metal, which melts at an intermediate temperature, F_M is defined for 100-fs pulses, but not for 160-fs pulses, because the plasma expands too greatly and a clear surface is not produced for the longer pulse.

IV. Conclusions

In summary, we measured the periodic structures self-formed on the surface of Al, Au, Cu, Ti, Pt, Mo, and W metals. We found that the laser fluence dependence of periodic structure interspaces is the same for all metals on which the structure is self-formed. The dependence can be explained by the induction of a surface plasma wave through the parametric decay of laser light, and can be reduced to the dependence of the density of laser-produced plasmas.

Acknowledgments

We thank Professors T. Kanaya, K. Nishida, and T. Terashima for their assistance with SEM and AFM. This work was partially supported by the JSPS-CAS Core-University Program in the field of Laser Plasma and High Energy Density Physics, financially supported by a Grant-in-Aid for the Global COE Program “The Next Generation of Physics, Spun from Universality and Emergence” from the Ministry of Education, Culture, Sports, Science and Technology (MEXT) of Japan and supported in part by the

Amada Foundation for Metal Work Technology and a Grant-in Aid for Scientific Research (C)(22560720) from MEXT, Japan.

References

1. F. Costache, M. Henyk, and J. Reif, Appl. Surf. Sci. **208** 486-491(2003).
2. N. Yasumaru, K. Miyazaki, and J. Kiuchi, Appl. Phys. A **76**, 983-985(2003).
3. M. Hashida, M. Fujita, Y. Izawa, and A. F. Semerok, *in Laser Precision Microsfablication*, Proc. SPIE, edited by I. Miyamoto *et al*. (SPIE, Washington, 2002), Vol.**4830** pp.452-457.
4. A. Y. Vorobyev, V. S. Makin, and C. Guo, J. Appl. Phys. **101**, 034903(2007).
5. A. Y. Vorobyev and C. Guo, Appl. Surf. Sci. **253**, 7272-7280(2007)
6. M. Tsukamoto, K. Asuka, H. Nakano, M. Hashida, M. Katto, N. Abe, M. Fujita, Vacuum **80**, 1346-1350(2006).
7. V. S. Makin, R. S. Markin, A. Ya Vorobyev, and C. Guo, Technical Phys. Lett. **34**, 387-390 (2008).
8. A. Y. Vorobyev, and C. Guo, J. Appl. Phys. **104**, 063523(2008).
9. Q. Z. Zhao, S. Malzer, and L J. Wang, Opt. Lett. **32**, 1932-1934(2007).
10. E. V. Golosov, V. I. Emel'yanov, A. A. Ionin, Yu. R. Kolobov, S. I. Kudryashov, A. E. Ligachev, Yu. N. Novoselov, L. V. Seleznev, and D. V. Sinitsyn, JETP Lett. **90**, 107-110(2009).
11. J. Wang and C. Guo, J. Appl. Phys. **100**, 023511(2006).
12. G. A. Shafeev, J. Degert, N. Lascoux, E. Freysz, "*Periodic structures produced by a scanning beam of a femtosecond Ti: sapphire laser*" *Conference on lasers and Electro-Optics (CLEO),* Baltimore, Maryland, JTuC45(2005).
13. A. Y. Vorobyev, and C. Guo, J. Appl. Phys. **103**, 043513(2008).
14. J. Wang and C. Guo, Appl. Phys. Lett. **87**, 251914(2005).
15. J. Gottmann, D. Wortmann, and M. H-Jungemann, Appl. Surf. Sci. **255**, 5641-5646(2009).
16. A. Y. Vorobyev, and C. Guo, Phys. Rev. B **72**, 195422 (2005).
17. J. Kim, S. Na, S. Cho, W. Chang, and K. Whang, Opt. Lasers Eng. **46**, 306-310(2008).
18. S. E. Kirkwood, A. C. Popta, Y. Y. Tsui, R. Fedosejevs, Appl. Phys. A **81**, 729-735(2005).

19. A. Weck, T. H. R. Crawford, D. S. Wilkinson, H. K. Haugen, J. S. Preston, Appl. Phys. A **89**, 1001-1003(2007).
20. A. Weck, T. H. R. Crawford, D. S. Wilkinson, H. K. Haugen, J. S. Preston, Appl. Phys. A **90**, 537-543(2008).
21. R. V Volkov, D. M. Golishnikov, V. M. Gordienko, A. B. Savel'ev, JETP Lett. **77**, 473-476(2003).
22. A. Y. Vorobyev and C. Guo, Appl. Phys. A **86**, 321-324(2007).
23. B. K. Nayak, M. C. Gupta, and K. W. Kolasinski, Appl. Phys. A **90**, 399-402(2008).
24. V. Oliveira, S. Ausset, and R. Vilar, Appl. Surf. Sci. **255**, 7556-7560(2009).
25. Y. Huang, S. Liu, W. Li, Y. Liu, and W. Yang, Opt. Express **17**, 20756-20761(2009).
26. H. Zhang, M. Tang, J. McCoy, and T. Her, "Growth of Periodic Tungsten Nanoripples Induced by Linearly Polarized Femtosecond Laser. in Lasers and Electro-Optics", *Conference on lasers and Electro-Optics (CLEO),* California, JTuD6(2006).
27. Q. Z. Zhao, S. Malzer, and L.J. Wang, Optics Express **15**, 15741-15746(2007).
28. S. Sakabe, M. Hashida, S. Tokita, S. Namba, and K. Okamuro, Phys. Rev. B **79**, 033409(2009).
29. M. Hashida, S. Namba, K. Okamuro, S. Tokita, and S. Sakabe, Phys. Rev. B **81**, 115442(2010).
30. S. Tokita, M. Hashida, S. Masuno, S. Namba, S. Sakabe, Opt. Express **16**, 14875-14881(2008).

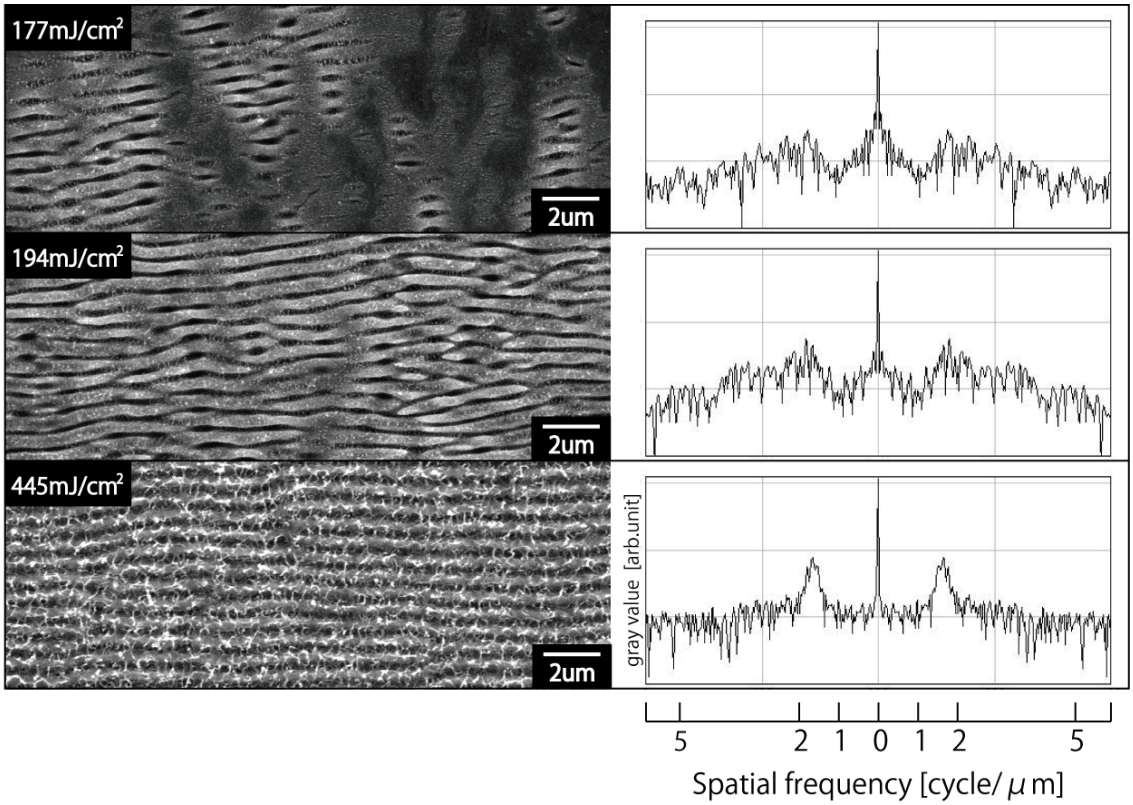

Fig. 1 SEM images of periodic surface structures on tungsten produced by 160-fs laser pulses of 50 and Fourier transform spectra.

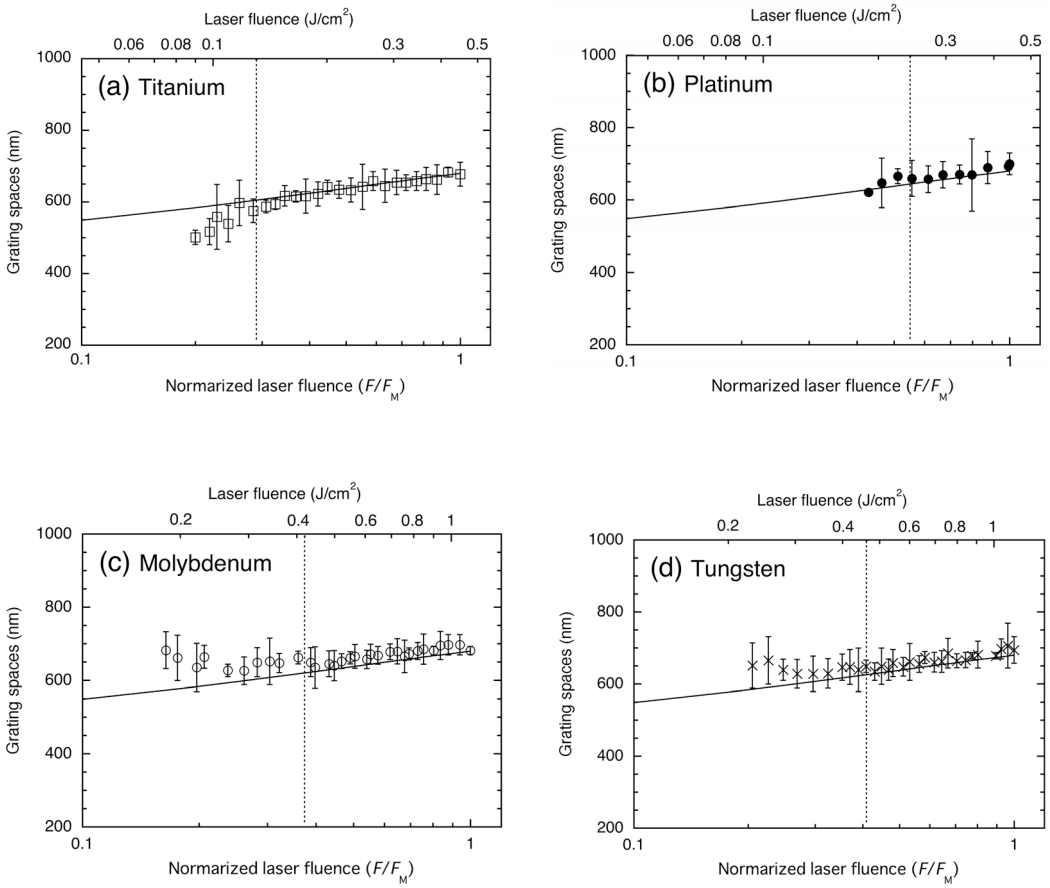

Fig. 2 Laser fluence dependence of the periodic structure interspaces produced by femtosecond laser pulses for (a) Ti, (b) Pt, (c) Mo, and (d) W (pulse duration: 160 fs). The interspace of the grating structure was determined by analyzing a set of 10 irradiated spots on the metal surface. Error bars show the standard deviation of the interspaces. Laser fluence is normalized by the upper limit on laser fluence for producing periodic structures, F_M. Solid lines show calculation results according to the parametric decay model proposed by Sakabe *et al.* [23], and dotted lines show the laser fluence for the ablation rate of 10 nm/pulse.

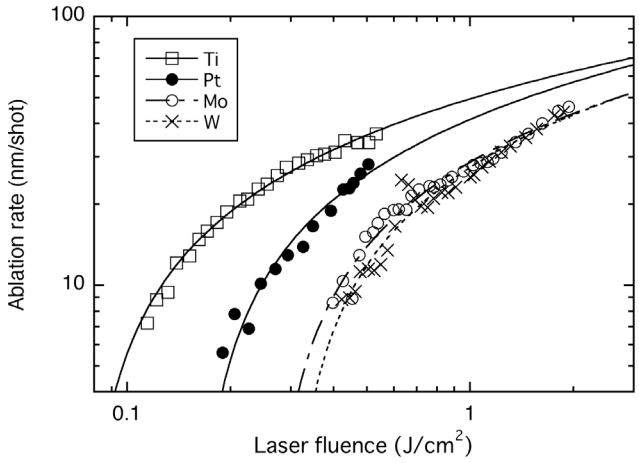

Fig. 3 Laser fluence dependence of ablation rate for metals on the surface of which self-formation of periodic structures occurs. Experimental data was fit to the well-known function $L=\alpha^{-1}\ln(F/F_{th})$, where α^{-1} is the optical absorption or heat penetration coefficient, F is the laser fluence, and F_{th} is the ablation threshold fluence.

Table 1 Upper limit on laser fluence for producing periodic structures, F_M, and the laser fluence corresponding to an ablation rate of 10 nm/pulse, F_{10nm}, are listed for the metals. T_m is the melting point.

Metal	T_{melt}(K)	F_M (J/cm^2)	F_{10nm}
Al	933		
Au	1337	No periodic structure	
Cu	1356		
Ti	1938	0.45	0.13
Pt	2042	0.44	0.24
Mo	2888	1.1	0.42
W	3672	1.1	0.46

Single-cycle short-wavelength laser pulse twowards Schwinger Limit

Baifei Shen

State Key Laboratory of High Field Laser Physics, Shanghai Institute of Optics and Fine Mechanics, Chinese Academy of Sciences, P. O. Box 800-211, Shanghai 201800, China

Email: bfshen@mail.shcnc.ac.cn

A scheme for producing nearly single-cycle relativistic laser pulses of wavelength 800 nm is proposed. When a laser pulse interacts with an overdense thin foil, because of self-consistent nonlinear modulation the latter will be more transparent to the more-intense part of the laser, so that a transmitted pulse can be much shorter than the incident pulse. Using two-dimensional particle-in-cell simulation and analytical modeling, it is found that a transmitted pulse of duration 4 fs and peak intensity $3x10^{20}$ W/cm^2 can be generated from a circularly polarized laser pulse. [1] We also propose a plasma approach to generate intense chirped pulse. When two counter-propagating circularly polarized (CP) pulses interact with an overdense foil, the driving pulse (with larger laser field amplitude) will accelerate the whole foil to form a double-layer structure, and the scattered pulse (with smaller laser field amplitude) is reflected by this flying-layer. Due to the Doppler effect and varying velocity of the layer, the reflected pulse is up-shifted for frequency and highly chirped, thus could be compressed to nearly single-cycle intense laser pulse with short wavelength. Simulations show that a sub-femtosecond nearly single-cycle relativistic pulse can be generated with wavelength of 0.2 μm after dispersion compensation. This method may lead to a laser pulse towards the Schiwinger limit. [2] Since the schemes involve only laser-plasma interaction, the intensity of the resulting short pulse is only limited by that of the incident pulse.

[1] L. Ji, B. Shen et al., Phys. Rev. Lett. 103, 215005 (2009)
[2] L. Ji, B. Shen et al., Phys. Rev. Lett. 105, 025001 (2010)

*Full paper was not submitted by authors.

Nonlinear optical phenomena in extreme ultra-violet region with high energy density conditions

Hitoki Yoneda, F. Sato, T. Ohashi, D. Baek
Institute for Laser Science, University of Electro-Communications, Japan
Y. Inubushi, T. Kumagai, D.Kimura, R. Kodama,
1Graduate School of Engineering, Osaka University
H. Kitamura
Department of Physics, Kyoto University
T. Ishikawa, H. Ohashi, H. Kimura, K. Tono, T. Togashi, M. Nagasono, A. Higashiya, M. Yabashi
XFEL RIKEN, and JASRI

Abstract: Advances of Free Electron Laser technology make us to open the new scientific field of nonlinear optics in extreme ultra-violet region. In this report, we show the recent experimental results of EUV-laser solid interaction. In this experiments, we observe (1)strong saturation of absorption in Sn, (2)increasing of absorption with two step excitation in Ti. In the case of Tin, we can achieve a large ratio of transmission between before and after bleaching. The four level simulation shows this feature is come from very short absorption length of EUV region and high interaction intensity for bleaching.

1. INTRODUCTION

Free electron laser can generate high energy photon up to X ray wavelength. Due to the mediumless feature in this laser, it also decrease pulse duration easily without any dispersion problem. Therefore, high intense with ultra-short pulse laser interaction experiments are now prepared with well wavelength tuned condition.

When we list up the energy state of elements, in extreme ultra-violet (EUV) region, we start to ionize or excite inner-shell electrons. In addition, the frequency of these photons already exceeds the plasma frequency of metals so that the EUV lasers has week interaction with free electrons in the conduction band of the metal and free electrons in the plasma. When EUV laser irradiate metals, inner shell electrons mainly excited if we select the EUV laser wavelength and potential energy of inner shell electrons. (Fig.1) In the conduction band there are enough rooms to shift the electrons easily. If the difference between inner-shell potential energy and upper level of conduction band is matched to EUV photon energy very carefully, the excited electrons in the conduction band has small difference energy to compare the original electrons(dE~0.1eV). As well-known, the additional electrons in the conduction band collide with each other or with originally located electrons and make another thermal equilibrium condition. But, the increment of temperature will be dE/2 at most, if we assume the single ionization. Therefore, we can create not so

hot materials even with inner shell ionization.

This nonthermal electrons component should be thermalized. For this time constant, there are several experimental data. For example, C.-K. Sun measured thermalization time inside conduction band with ultra-short-pulse laser pump-probe method, and conclude that it is 0.3~0.5ps with 2~3eV energy input. This relaxation time is longer than pulse duration of EUV laser and is shorter than expansion time.

Kitamura calculate the energy potential condition after inner shell ionization.[2, 3] In this calculation, 9 and 24 atoms cluster is used and if the ionization electrons is located just above the level of the original conduction band electrons. The results show that (1) even with 30% ionization of inner shell electrons, the system shows stable condition in energy.(bound structure of cluster can be kept.) (2)edge shift of absorption edge is occurred.

The summary above discussion suggest us the EUV laser interaction, we can/may keep the ordering structure of condensed matter after inner shell ionization. And that condition will deform the potential energy inside atoms. It also results in the large optical constant will change at the absorption edge and the interaction EUV laser itself will be modulated by this material changing.

2. Experiments

For demonstrate for the above idea, we use EUV-FEL of SPring-8 site, Japan. The nominal parameters of this laser are follows, pulse energy is 20μJ, pulse duration is ~100fs, and the minimum focusing diameter is 6μm. Tuning range of wavelength in this experiment is from 51nm to 61nm. We also use white light probe produced with self phase modulation in Sapphire crystal. The range of this white light is from 450nm to 800nm. By using optical delay line, the arrival time of probe laser can be scanned with every 97fs. Due to the transmission optics, this white light has positive chirp in wavelength. The 800nm component arrive the target about 4ps earlier than 450nm one.

Figure 2 is typical reflection spectrum of the EUV pump and white light probe experiment with Au thin(10nm) target. The number of each spectrum shows the position of the optical delay line. As we mentioned above, this white probe laser has chirped so that if we limit small frequency range, we can extract temporal feature of reflectivity even with single shot base. Figure 3 shows the estimated temporal profile of reflectivity at around 500nm wavelength. It is observed that rapid increasing of reflectivity and slow decay of it. The typical rise time is 100fs, while the decay constant is1ps, respectively. In the case of Au, spectral reflectivity profile at longer wavelength is well matched to Drude law(free electron component). This reflectivity curve has sharply decreasing at 500nm due to the d-f transition. If we use Drude formula for the dielectric constant and the increasing the carrier in the conduction band due to the photoexcitation

of EUV, it is easy to explain the increase of reflectivity of this range. With similarity of UV laser pump-probe experiment, the sequential decay of the reflectivity is explained by the AC conductivity reduction due to the target expansion. The temporal change in red region (Fig.4) has small increasing of reflectivity and large decreasing. That is also explained with Drude law because in this wavelength cold reflectivity is enough high so that change of the reflectivity looks emphasize decreasing phenomena .

However, we also observe very different reflectivity spectrum at delay line position of t=90. In this time, very broad and rapid increasing of reflectivity in 450nm region is observed. Lifetime of this feature is less than the scanning frame interval(97fs) and if we assume Fourier transform limit condition, the corresponding life time is estimated to be 40fs. Until now, we have no quantitative explanation for this “flash” in Blue, we consider d- and f- orbit energy are moved toward higher energy by inner shell ionization. This means we can keep band structure even with inner shell ionization and this is one of the experimental evidence for cold hollow atom solid.

Previously, we observe strong recovery of absorption in Sn thin films.[4] To seek another nonlinearity with EUV region, we shoot Al, Ge, Sc, SiO2, Au and Ti. Thickness of each material is chosen to be absorption length ($1/\alpha$) in the cold condition. Figure 5 shows the typical results of these materials(Ge, SiO_2, Al, Sc). Behavior of these four materials shows almost linear phenomena. However, Ti case, we observe strong reduction of transmission at higher intensity region. In the case of Ti, we have small absorption coefficient in fundamental wavelength while a large absorption is expected at twice energy of incident photons due to M shell electron excitation. Due to the two photon absorption β scaling with band gap energy E_g in visible and infrared region, β is considered to be proportional to Eg-3. If we extrapolate this feature to EUV region, the β value estimated from the experiments is extremely high. ($x10^5$) In addition, even though there is far from the resonance of atomic energy state at the fundamental wavelength, we have non-negligible absorption in this wavelength. Therefore, up to now, we consider that these phenomena are due to the excitation absorption process. Even though mechanism is not cleared, feature of intensity depend transmission can be used for diagnostics for EUV lasers.

3. Conclusion

We observe the evidence of keeping band structure of Au even with inner shell ionization in condensed matter in Au. In Ti, we also observe different type of nonlinear phenomena in EUV region. The mechanism of this new nonlinearity is considered to be multi-(step)-photon absorption. We can apply these nonlinear

mechanism for characterize EUV lasers and these idea can be extrapolated to X-ray region.

Acknowledgements

This work was supported by XFEL project in Japan by Ministry of Education, Science , Culture, and Sports. This work was partially supported by the JSPS-CAS Core-University Program in the field of Laser Plasma and High Energy Density Physics.

References

[1] C.-K. Sun, F. Vallée, L. H. Acioli, E. P. Ippen and J. G. Fujimoto, Femtosecond-tunable measurement of electron thermalization in gold, Phys. Rev. B 50, 15337–15348 (1994)

[2] H. Kitamura, Eur. Phys. J. D **52**, pp.147-150 (2009)

[3] H. Kitamura, "Rate equation for intense core-level photoexcitation and relaxation in metals", J. Phys. B: At. Mol. Opt. Phys. 43, 115601 (2010)

[4] H. Yoneda, et al. Optics Express, Vol. 17 Issue 26, pp.23443-23448 (2009)

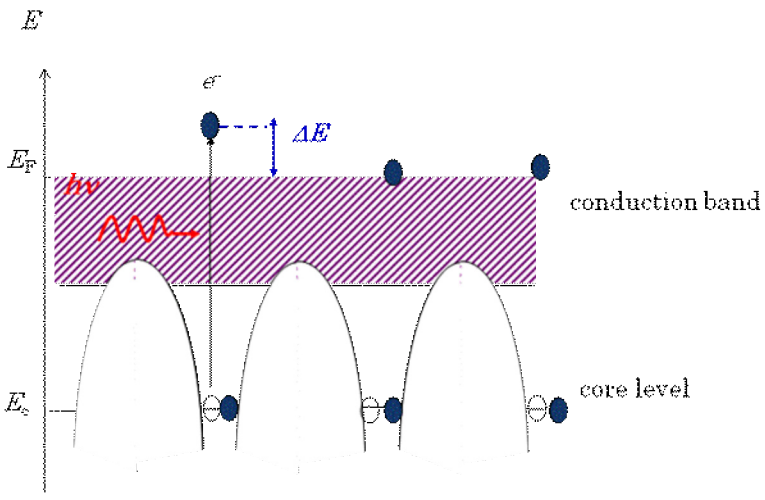

Fig.1 Image of inner shell ionization to conduction band in metal

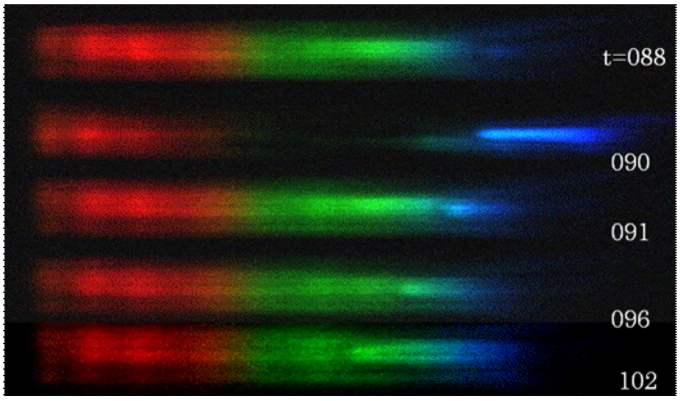

Fig.2 Typical reflective spectrum of white light probe with EUV pump

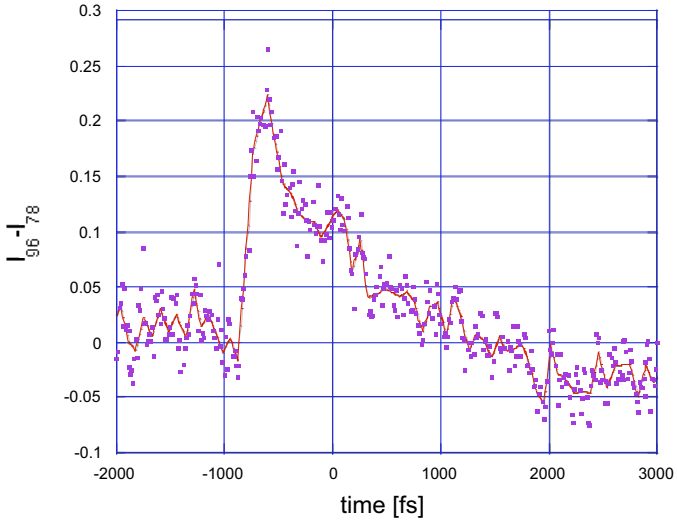

Fig.3 Temporal profile of reflectivity after EUV illumination. (The probe light wavelength is 500nm.)

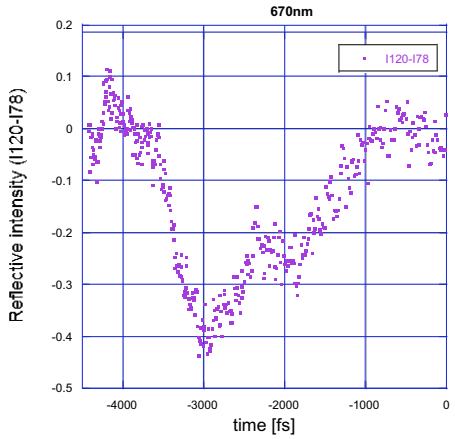

Fig. 4 Temporal profile of reflectivity after EUV illumination. (The probe light wavelength is 670nm.)

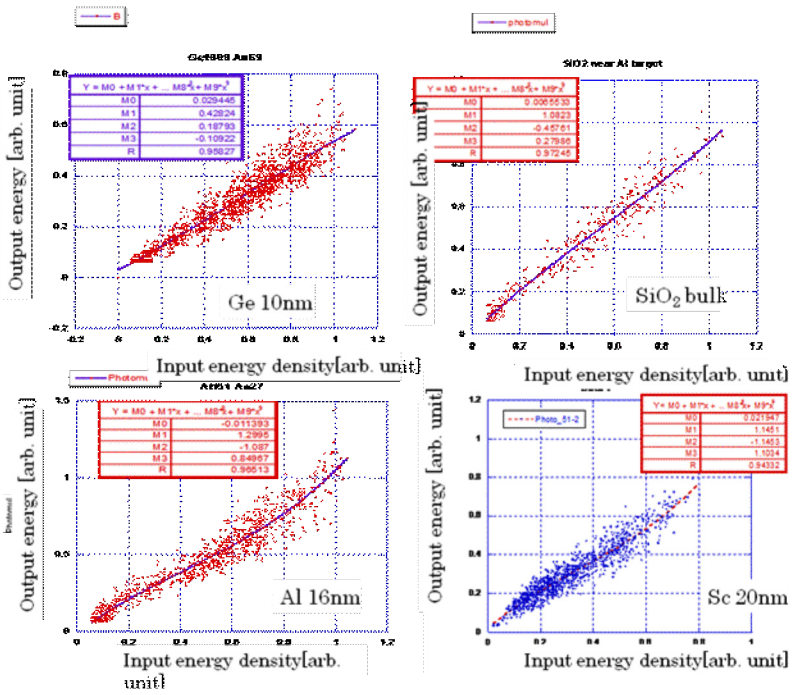

Fig.5 Intensity dependence of transmission for various materials.

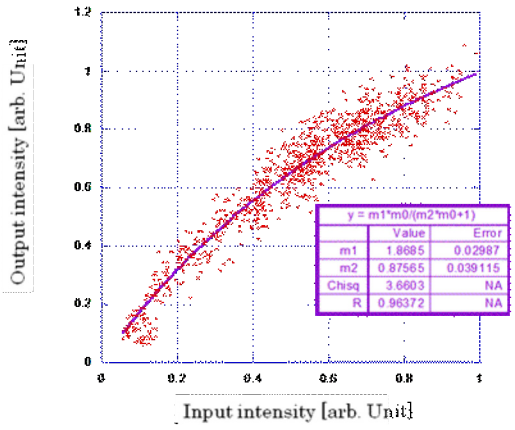

Fig.6 Nonlinear transmission of Ti in EUV wavelength.

Experimental study and application of laser-driven shock waves at SILP

Xiuguang Huang（黄秀光） Sizu Fu（傅思祖）

Hua Shu（舒桦） Junjian Ye（叶君建）

Shanghai Institute of Laser Plasma, P.O. Box 800-229, Shanghai 201800, China

Abstract:

In this paper, some important characters of laser-driven shock waves are discussed, including the planarity and stability of the shock wave, and the material's preheating ahead of the shock front. The Hugoniot data of Cu, Au, Pt, CH2, C8H8 obtained with this shock wave loading and impedance-match method are reported, the maximum pressure is up to ~2.7TPa in Au and the relative expanded uncertainties of the measured shock velocity are about 2% (K=2). Also, the isentropic release of Au after the intense shock is presented. Finally, the first experimental study on shock-timing in double-shocked CH is shown, and the results are compared with Omega's.

邀请报告，报告人：黄秀光，email：huangxiuguang@sohu.com，021-69914219

*Full paper was not submitted by authors.

Computational Study of Shock Instability and Its Application

Naofumi Ohnishi, Masami Tate, Yousuke Ogino
Department of Aerospace Engineering, Tohoku University, 6-6-01 Aramaki-Aza-Aoba, Aoba-ku, Sendai 980-8579, Japan
ohnishi@rhd.mech.tohoku.ac.jp

Wakana Iwakami Nakano
Institute of Fluid Science, Tohoku University, 2-2-1 Katahira, Aoba-ku, Sendai 980-8577, Japan

Kei Kotake
Division of Theoretical Astronomy / Center for Computational Astrophysics, National Astronomical Observatory of Japan, 2-21-1 Osawa, Mitaka, Tokyo 181-8588, Japan

Shoichi Yamada
Science & Engineering / Advanced Research Institute for Science and Engineering, Waseda University, 3-4-1 Okubo, Shinjuku, Tokyo 169-8555, Japan

ABSTRACT

Three-dimensional simulations of standing accretion shock instability in core-collapse supernova cores have been done with realistic EOS, neutrino heating, and steady initial conditions, and their results indicate that neutrino heating level is not different from the two-dimensional case while much more modes are excited in the nonlinear growth of the non-axisymmetric perturbations. Also, we have developed a computational code based on axisymmetric Navier-Stokes equations with thermochemical kinetics for assessing wave drag reduction and other effects in pulse energy deposition ahead of a bow shock by means of full-simulation from generation of laser-induced blast wave to interaction with the bow shock. The result suggests that the shape of the blast wave affects on the resultant wave drag, and parameters of laser incident should be taken into account for exploring the optimal condition of the proposed wave drag scheme.

Subject headings: Supernovae, Shock Wave Instability, Wave Drag Reduction

1. Introduction

Many efforts have been made for the multi-dimensional modeling of core-collapse supernovae (see Woosley & Janka (2005); Kotake et al. (2006) for reviews), urged by accumulated observational evidences that core-collapse supernovae are globally aspherical commonly (Wang et al. 1996, 2001, 2002). Various mechanisms to produce the asymmetry have been discussed so far: convection (e.g., Herant et al. (1994); Burrows et al. (1995); Janka & Mueller (1996)), magnetic field and rapid rotation (see, e.g., Kotake et al. (2006) for collective references), standing (/stationary/spherical) accretion shock instability, or SASI, (Blondin et al. 2003; Scheck et al. 2004; Blondin & Mezzacappa 2006; Ohnishi et al. 2006, 2007; Foglizzo et al. 2006), and g-mode oscillations of protoneutron stars (Burrows et al. 2006). Note, however, that most of them have been investigated with two-dimensional (2D) simulations.

Recently a 3D study on SASI was reported by

Blondin & Mezzacappa (2007). In 2D, the shock deformation by SASI is described with the Legendre polynomials $P_l(\theta)$, or the spherical harmonics $Y_l^m(\theta, \phi)$ with $m = 0$. Various numerical simulations have demonstrated unequivocally that the $l = 1$ mode is dominant and a bipolar sloshing of the standing shock wave occurs with pulsational strong expansions and contractions along the symmetry axis (Blondin et al. 2003; Scheck et al. 2004; Blondin & Mezzacappa 2006; Ohnishi et al. 2006, 2007). In 3D, on the other hand, Blondin & Mezzacappa (2007) perturbed a non-rotating accretion flow azimuthally and observed the dominance of a non-axisymmetric mode with $l = 1$, $m = 1$, which produces a single-armed spiral in the later nonlinear phase. They claimed that this "spiral SASI" generates a rotational flow in the accretion (see also Blondin & Shaw (2007) for 2D computations in the equatorial plane) and that it may be an origin of pulsar spins.

There are many questions on 3D SASI remaining to be answered yet, however. For example, we are interested in how the growth of SASI differs between 3D and 2D among other things. In particular, the change in the saturation properties should be made clear. Another issue will be the generation of rotation in the accretion flow by SASI (Blondin & Mezzacappa 2007). Its efficiency and possible correlation with the net linear momentum should be studied more in detail. Incidentally, it is noted that the neutrino heating and cooling were entirely ignored and the flow was assumed to be isentropic in Blondin & Mezzacappa (2007), but the implementation of this physics is helpful for considering the implications not only for the shock revival but also for the nucleosynthesis (Kifonidis et al. 2006).

On the other hand, a kind of shock instability may be applied for the flow control technique such as wave drag reduction of a supersonically moving object. In a supersonic flight, a blunt vehicle experiences unavoidable large drag originated from a detached shock wave ahead of it. Reducing this wave drag improves the fuel efficiency and the operation flexibility of the vehicle. Attaching a spike on the body nose is one of the methods to reduce the wave drag (Bogdonoff & Vas 1959; Crawford 1959; Maull 1960). The spike forms a conical shock wave that changes the flow direction outward, leading to reduce the drag and the convective heat flux of the body. Although this method can reduce the drag significantly, it seems to have problems towards a practical application. The spike needs to endure the large heat flux at the apex, and the pitching moment must be generated in a flight with angle of attack. In order to avoid these problems, nonstructural methods of drag reduction have been investigated, which use energy deposition instead of the physical spike (Bushnell 1990; Myrabo & Raizer 1994; Riggins et al. 1999; Takaki 2002). By continuously supplying energy using CW laser ahead of the blunt body, a conical shock wave is formed and the drag of the body is reduced as with the structural method.

In the last decade, a supersonic flow controlling method using a pulse energy deposition has been proposed (Georgievsky & Levin 1993; Adelgren et al. 2001; Kandala & Candler 2004; Georgievsky & Levin 2004; Adelgren et al. 2005; Zheltovodov et al. 2007). In this method, a pulse energy supplied ahead of a bow shock over a blunt body generates a blast wave, and it interacts with the bow shock. Since in an inviscid flow the wave drag is originated from only the entropy production due to the shock wave, it can be considered that the drag reduction comes from any mechanisms that effectively achieve a low-entropy bow shock. Therefore, a unsteady shock wave including vortices behind it may suppress the entropy jump at the (time-averaged) shock front. If any density perturbations are supplied in front of the bow shock, the vortex must be generated at the shock front due to the Richtmyer-Meshkov-like instability, or the baroclinic effect in other words. In the blast wave induced by the pulse energy deposition, a low-density core corresponding to the contact surface of the plasma is developed as the preceding shock wave expands and has a steep gradient at its surface. This may be a seed for the baroclinic vortex and consequently lead to the reduction of the wave drag through temporally suppressing the entropy production of the bow shock wave.

In our previous work, we performed the numerical simulations of the interaction between a blast wave generated by a pulse energy deposition and a bow shock developed in front of a sphere, in order to analyze the drag reduction by the energy deposition (Taguchi et al. 2007; Ogino et al. 2009). We focused on purely hydrodynamical effect on the drag reduction, i.e., the mechanism of

the drag reduction by pulse energy deposition in an ideal gas. As a result, we found out that the drag is more reduced while a vortex region that generated by the interaction is moving along the wall surface. In addition, we performed a parametric study for deposited energy, deposition location, and freestream Mach number in order to find their dependencies on reduced energy and to obtain a physical interpretation from the perspective of baroclinic vortex generation with a simple theoretical interpretation (Ogino et al. 2009).

In this paper, we present our multi-dimensional simulation results for above two issues which include the shock-dominated hydrodynamic instability. We expect that knowledge from them may help each other in not only numerical techniques for accurately capturing unsteady shock dynamics but also physics therein.

2. 3D SASI Simulation with Steady Initial Conditions

The numerical methods employed in the present paper are based on the code ZEUS-MP/2 (Hayes et al. 2006), which is a computational fluid dynamics code for the simulation of astrophysical phenomena, parallelized by the MPI (message-passing) library. The ZEUS-MP/2 code employs the Eulerian hydrodynamics algorithms based on the finite-difference method with a staggered mesh. In this study, we have modified the original code substantially according to the prescriptions in our preceding 2D simulations (Ohnishi et al. 2006, 2007).

In order to induce the non-spherical instability, we have added a radial velocity perturbation, $\delta v_r(r, \theta, \phi)$, to the steady spherically symmetric flow according to the following equation,

$$v_r(r, \theta, \phi) = v_r^{1D}(r) + \delta v_r(\theta, \phi), \qquad (1)$$

where $v_r^{1D}(r)$ is the unperturbed radial velocity. In this study, we consider two types of perturbations: an axisymmetric ($l = 1, m = 0$) single-mode perturbation,

$$\delta v_r(\theta, \phi) \propto \sqrt{\frac{3}{4\pi}} \cos\theta \cdot v_r^{1D}(r), \qquad (2)$$

and a random multimode perturbation,

$$\delta v_r(\theta, \phi) \propto \mathrm{rand} \cdot v_r^{1D}(r) \quad (0 \leq \mathrm{rand} < 1), \quad (3)$$

where "rand" is a pseudo-random number. The perturbation amplitude is set to be less than 1% of the unperturbed velocity.

The SASI is supposed to be an important ingredient not only for the pulsar's proper motions and spins but also for the explosion mechanism itself. So, we look into the neutrino heating in the non-axisymmetric SASI. In the early phase, the radiatively cooling region exists around the proto neutron star while the heating region extends over the cooling region up to the stalled shock wave. As the time passes and the SASI grows, a pocket of regions with positive but relatively low net heating rates appear. These regions correspond to the high entropy blobs (high entropy rings for the axisymmetric case), where the circulating flow exists observed. Since the neutrino emission in these regions is more efficient than the surroundings, the net heating rate is rather low.

Figure 1 shows net heating rate integrated over the whole simulation domain of 3D simulation for the case of (a) non-explosion model and (b) explosion model. Black lines indicate a result without any perturbations, i.e., spherical symmetric simulation and blue lines with $l = 1$, $m = 0$ axisymmetric mode. In the axisymmetric case, the perturbation amplitudes are larger than that with non-axisymmetric random perturbation. This strongly reflects the shock motion in the axisymmetric flow. The average value is, however, not so large relative to the non-axisymmetric one. Actually, since the critical luminosities must exist between $L_\nu = 6.0 \times 10^{52}$ and $L_\nu = 6.8 \times 10^{52}$ ergs s^{-1} for axisymmetric and non-axisymmetric case, the difference in the amplitudes does not affect on them.

Although the critical neutrino luminosties are not much different between the non-axisymmetric and axisymmetric cases, the spatial distributions of neutrino heating are different. In the axisymmetric case the shock wave oscillates up and down whereas it moves in all directions in the non-axisymmetric case. The oscillation amplitudes are larger in the former than in the latter in general as repeatedly mentioned. Reflecting this difference in the shock motions, the neutrino heating is enhanced in mainly in the polar regions in the axisymmetric case while in the non-axisymmetric case the heating rate is affected by SASI chiefly around the high entropy blobs.

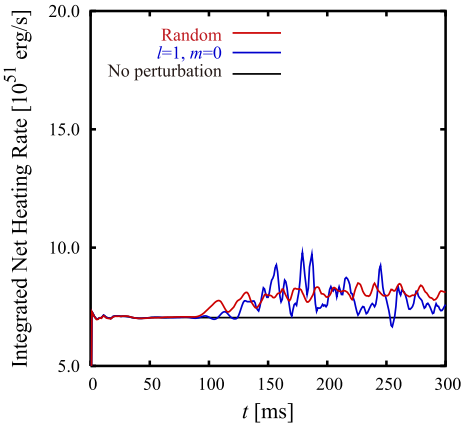

(a) non-explosion model ($L_\nu = 6.0 \times 10^{52}$ erg/s)

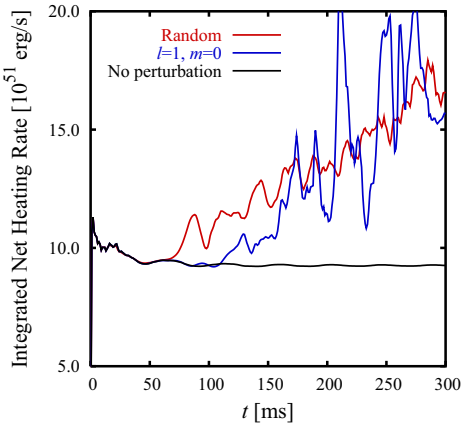

(b) explosion model ($L_\nu = 6.8 \times 10^{52}$ erg/s)

Fig. 1.— Net heating rate integrated over the simulation domain

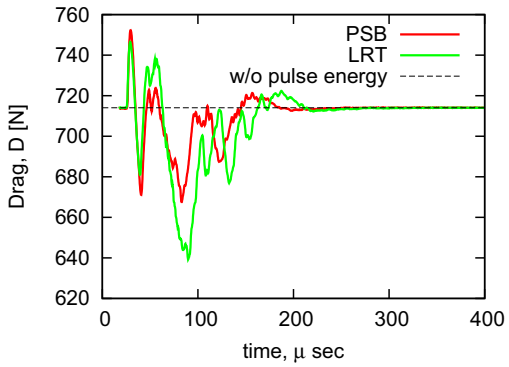

(a) Drag

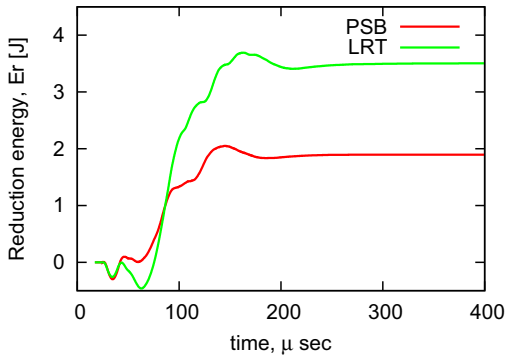

(b) Reduction energy

Fig. 2.— Time histories of drag and reduction energy (PSB: w/ point source blast wave, LRT: w/ blast wave obtained by laser ray-trace).

3. Wave drag reduction by laser energy deposition

In order to assess a wave drag reduction scheme for a supersonic blunt body by using laser energy deposition, we perform the numerical simulations of a blast wave generation and the subsequent interaction with a bow shock. We have developed a numerical code based on axisymmetric Navier-Stokes equations with eleven chemical species and twenty-one chemical reactions including some ionization reactions. Two-temperature model by Park (1989) is employed as thermochemical model in order to take thermochemical nonequilibrium into our simulations. Moreover, an amount of energy absorbed in flowfield is computed by ray-tracing method (Edwards & Fleck 1979). The developed code can reproduce the thermochemical nonequilibrium flow for the blast wave induced by pulse energy deposition and the vortex dissipation and the conductive heating in the bow shock in the front of a body.

A blunt body is assumed to be a hemisphere with diameter $d = 100$ mm and wall temperature of 1000 K. The number of grid points is 181×151 which covers not only the bow shock over a hemisphere but also the blast wave in the upstream. The initial flowfield of interaction is generated by superimposing the blast wave to a steady-state bow shock solution. In this case, the blast wave is superimposed so that the incident laser is focused at the distance of 50 mm from the sphere surface (stagnation point). The mainstream conditions are the same as the previous section.

The efficiency of the drag reduction is evaluated by E_r/Q, where E_r is the reduction energy (Taguchi et al. 2007) of the body defined by

$$E_r = u_\infty \int_0^\infty (D_0 - D(\tau))d\tau, \qquad (4)$$

and Q is the input laser energy. Here, u_∞ is the mainstream velocity, and D_0 and $D(\tau)$ are the computed drags at initial time (steady state) and $t = \tau$, respectively. Figure 2 shows time histories of drag and reduction energy. Green lines are the results with the blast wave by laser ray-trace while red lines are ones with a spherical blast wave by a point source whose energy is identical to the absorbed laser energy. The drag is significantly reduced by the interaction as shown in our inviscid computations (Taguchi et al. 2007; Ogino et al. 2009). The reduction energy converges to about 3.5 J which corresponds to 11.7 times as the input laser energy.

Note that this efficiency is estimated based on the input energy but the absorbed one though this value seems to be small as contrasted with the inviscid results. It is obvious that the absorption efficiency also becomes an important issue in this drag reduction scheme. Discrepancy between the realistic blast wave and the spherical one suggests that the blast wave shape also affects on the drag reduction mechanism. Although the present result indicates the advantage of the prolate blast wave rather than the spherical, further investigation is required for making any conclusions on this tendency.

The basic features of the interacting flowfield are similar to the inviscid results. The drag is reduced while the vortex region is moving along the wall surface as shown in Fig. 2 (a) and Fig. 3 (a). Then, it gradually recovers to the initial (steady state) value after the vortex region takes off from the wall surface as shown in Fig. 3 (c). The vortex advection is not so dissipated since the shock layer is almost inviscid in this condition. Moving along the wall surface for a long time may achieve more amount of drag reduction. For this reason, the blunt shape of the body can be another essential factor because it determines the vortex stay duration. Changing the body shape must be one of the candidates to obtain a large drag reduction (Sakai et al. 2008).

Increase of convective heating is also a critical

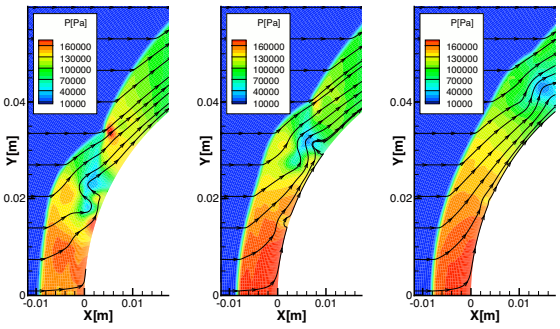

(a) $t = 140.0$ μs (b) $t = 160.0$ μs (c) $t = 180.0$ μs

Fig. 3.— Pressure contours in the bow shock layer.

issue for the practical application since any additional requirements to protect it should be avoidable. Figure 4 shows time histories of heating rate at stagnation point and surface integrated heating rate over the hemisphere. The heating rate is as $\sim$27 times higher than that of steady state value at stagnation point while the integrated value deviates within $\sim$2 times higher. Although this heating is momentary, a laser irradiation leading to such a point heating is not desirable. Depending on the thermal protection of the body, the laser should be focused with avoiding the stagnation point.

4. Conclusion

Three-dimensional simulations of standing accretion shock instability have been done with realistic EOS, neutrino heating, and steady initial conditions. Simulation results indicate that neutrino heating level is not increased from the two-dimensional case while the spiral modes are enhanced in a rotational flow. Three-dimensional computation with unstructured grid may be feasible for post-bounce simulation including proto-neutron star, and may be tested through the analysis of the bow shock instability.

As an application of hydrodynamic instability related to shock wave, we have investigated a wave drag reduction ahead of a blunt body by laser energy deposition using a computational code based on axisymmetric Navier-Stokes equations with thermochemical kinetics. A blast wave obtained by laser ray-trace method is not spherical depending on focusing condition, and weak vortex is created inside low-density core. Computations

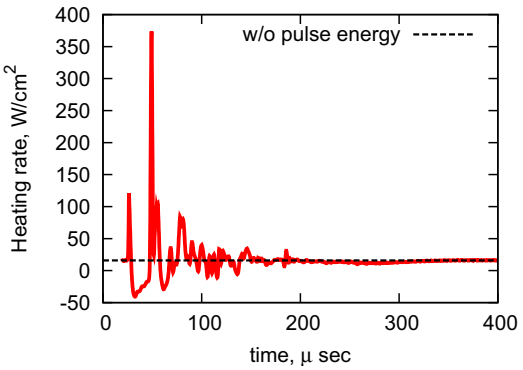

(a) Heating rate

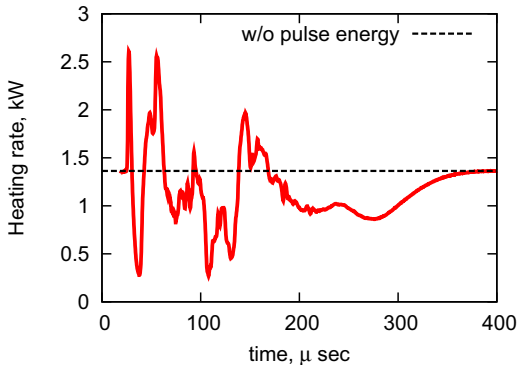

(b) Surface integrated heating rate

Fig. 4.— Time histories of heating rate at stagnation point and surface integrated heating rate.

of interacting flowfield were performed with a bow shock formed in Mach 5 flow. The result suggests that the shape of the blast wave affects on the resultant wave drag. A prorate blast wave may have an advantage to reduce the wave drag. Since the blast wave shape strongly depends on laser parameters, they should be taken into account for exploring the optimal condition of the proposed wave drag scheme.

This work was partially supported by the JSPS-CAS Core-University Program in the field of Laser Plasma and High Energy Density Physics.

REFERENCES

Adelgren, R. G., Elliott, G. S., Knight, D. D., Zheltovodov, A. A. & Beutner, T. J. 2001, AIAA Paper 2001-0885

Adelgren, R. G., Yan, H., Elliott, G. S., Knight, D. D., Beutner, T. J. & Zheltovodov, A. A. 2005, AIAA Journal, 43, 256

Blondin, J. M., Mezzacappa, A., & DeMarino, C. 2003, ApJ, 584, 971

Blondin, J. M. & Mezzacappa, A. 2006, ApJ, 642, 401

Blondin, J. M. & Mezzacappa, A. 2007, Nature, 445, 58

Blondin, J. M. & Shaw, S. 2007, ApJ, 656, 366

Bogdonoff, S. M. & Vas, I. E. 1959, Journal of Aerospace Science, 26, 65

Burrows, A., Hayes, J., & Fryxell, B. A. 1995, ApJ, 450, 830

Burrows, A., Livne, E., Dessart, L., Ott, C. D., & Murphy, J. 2006, ApJ, 640, 878

Bushnell, D. M. 1990, AIAA Paper 90-1596

Crawford, D. H. 1959, NASA TN D-118, Langley Research Center

Edwards, A. L. & Fleck, Jr., J. A. 1979, Journal of Applies Physics, 50, 4307

Foglizzo, T., Scheck, L., & Janka, H.-T. 2006, ApJ, 652, 1436

Georgievsky P. Y. & Levin V. A. 1993, Fluid Dynamics, 28, 568

Georgievsky, P. Y. & Levin V. A. 2004, AIAA Paper 2004-1019

Hayes, J. C., Norman, M. L., Fiedler, R. A., Bordner, J. O., Li, P. S., Clark, S. E., ud-Doula, A., & Mac Low, M.-M. 2006, ApJS, 165, 188

Herant, M., Benz, W., Hix, W. R., Fryer, C. L., & Colgate, S. A. 1994, ApJ, 435, 339

Janka, H.-T. & Mueller, E. 1996, A&A, 306, 167

Kandala, R. & Candler, G. V. 2004, AIAA Journal, 42, 2266

Kifonidis, K., Plewa, T., Scheck, L., Janka, H.-T., Müller, E. 2006, A&A, 453, 661

Kotake, K., Sato, K., & Takahashi, K. 2006, Reports of Progress in Physics, 69, 971

Maull, D. J. 1960, Journal of Fluid Mechanics, 8, 584

Myrabo, L. N. & Raizer, Y. P. 1994, AIAA Paper 94-2451

Ohnishi, N., Kotake, K., & Yamada, S. 2006, ApJ, 641, 1018

Ohnishi, N., Kotake, K., & Yamada, S. 2007, ApJ, 667, 375

Ogino, Y., Ohnishi, N., Taguchi, S. & Sawada, K. 2009, Physics of Fluids, 21, 066102

Park, C. 1989, Nonequilibrium Hypersonic Aerothermodynamics, John Wiley and Sons Inc., New York

Riggins, D. W., Nelson, H. F., & Johnson, E. 1999, AIAA Journal, 37, 460

Sakai, T., Sekiya, Y., Mori, K., & Sasoh, A. 2008, Journal of Aerospace Engineering, 222, 605

Scheck, L., Plewa, T., Janka, H.-T., Kifonidis, K., Müller, E. 2004, Physical Review Letters, 92, 011103

Taguchi, S., Ohnishi, N., Furudate, M. & Sawada, K. 2007, AIAA Paper 2007-1235

Takaki, R. 2002, Journal of the Japan Society for Aeronautical and Space Sciences, 50, 37

Wang, L., Wheeler, J. C., Li, Z., & Clocchiatti, A. 1996, ApJ, 467, 435

Wang, L., Howell, D. A., Höflich, P., & Wheeler, J. C. 2001, ApJ, 550, 1030

Wang, L., et al. 2002, ApJ, 579, 671

Woosley, S., & Janka, T. 2005, Nature Physics, 1, 147

Zheltovodov A. A., Pimonov E. A., & Knight D. D. 2007, AIAA Paper 2007-1230

HEDP2010 & CUP Daily Schedule

Wednesday (Oct. 13)	Thursday (Oct. 14)		Friday (Oct. 15)		Saturday (Oct. 16)	
13:00-18:00 Registration (Faculty Culb, SJTU)	08:30-08:45	**Opening remarks(CUP)**	08:30-08:45	**Opening remarks(HEDP)**		
	CUP Session 1	**Reviews (Chaired by Shaoping Zhu)**	**HEDP Session 1**	**Laser acceleration Chaired by Baohan Zhang**	**CUP Session 5**	**LPI Chaired by Xueqin Yan**
	08:45-09:00	H. Takabe	08:45-09:15	谷渝秋	09:00-09:30	Y. T. Li
	09:00-09:30	Jiamin Yang	09:15-09:45	Hongbin Zhuo	09:30-10:00	M. Hashida
	09:30-10:00	K. A. Tanaka	09:45-10:00	Yanyun Ma	10:00-10:30	Baifei Shen
	10:00-10:30	C. T. Zhou	10:00-10:15	Bin Liu		
	10:30-11:00 Group Photo & Coffee Break		**10:15-10:30 Coffee Break**		**10:30-10:45 Coffee Break**	
	CUP Session 2	**Laser astrophysics and acceleration (Chaired by Hitoshi Sakagami)**	**HEDP Session 2**	**Laser driven X-ray sources Chaired by Jianmin Yuan**	**CUP Session 6**	**Application Chaired by Kazuo Tanaka**
	11:00-11:30	H. Takabe	10:30-11:00	陈黎明	10:45-11:15	H. Yoneda
	11:30-12:00	X. Q. Yan	11:00-11:15	Jianqin Dong	11:15-11:45	Xiuguang Huang
	12:00-12:30	A. Sagisaka	11:15-11:30	Guang-yue Hu	11:45-12:15	N. Ohnishi
			11:30-11:45	王加祥		
			11:45-12:00	Cao Lei-Feng		
	Lunch 12:30-13:30		**Lunch 12:00-13:30**		**Lunch**	
	CUP Session 3	**IFE simulation Chaired by Cangtao Zhou**	**HEDP Session 3**	**Laboratory astrophysics and high energy density matters Chaired by Jie Liu**	**HEDP Session 5**	**Fast Ignition and high energy density matters Chaired by Yanyun Ma**
	13:30-14:00	A. Sunahara	13:30-14:00	Jianmin Yuan	14:00-14:30	A. L. Lei
	14:00-14:30	Jinghong Li	14:00-14:30	J. Y. Zhong	14:30-15:00	Xiaonong Zhu
	14:30-15:00	H. Sakagami	14:30-14:45	董全力	15:00-15:15	温贤伦
			14:45-15:00	Wei Yu	15:15-15:30	Lu Zhang
			15:00-15:15	L. F. Wang		

	Coffee Break **15:00-15:15**		**Coffee Break and Poster Session** **15:15-16:45**		**Coffee Break** **15:50-16:05**	
	CUP Session 4	**Diagnostic** **Chaired by Yutong Li**	**HEDP** **Session 4**	**Diagnostic of laser plasmas** **Chaired by Yuqiu Gu**	**HEDP** **Session 6**	**High energy density matters** **Chaired by Jian Zheng**
	15:15-15:45	H. Habara	16:45-17:00	赵宗清	15:45-16:15	Di-Fa Ye
	15:45-16:15	Jian Zheng	17:00-17:15	张红平	16:15-16:30	Jiayu Dai
	16:15-17:30	**Discussion toward next CUP** **(K. A. Tanaka)**	17:15-17:30	单连强	16:30-16:45	辛建婷
			17:30-17:45	滕建	16:45-17:00	Mu Li
			17:45-18:00	王首钧		
18:00 Reception (Faculty Club, SJTU)	**Dinner**		**Banquet 18:30 – 21:00** **(Faculty Club)**		**Dinner**	
Wednesday (Oct. 13)	**Tuesday (Oct. 14)**		**Friday (Oct. 15)**		**Saturday (Oct. 16)**	

* Conference site: No. 303 Auditorium, 3rd floor, Datong Plaza, Xuhui Campus, Shanghai Jiao Tong University (SJTU)

会议地点：上海交通大学上海高级金融学院 303 会议厅（上海交通大学徐汇校区达通广场 3 楼）

Program of China-Japan CUP Seminar on Laser Plasma Physics (CUP seminar)

Oct. 14-16, 2010, Shanghai Jiao Tong University, Xuhui Campus

October 13, 2010 (Wednesday)

13:00-18:00	Registration at SJTU Faculty Club
18:00	Reception, Faculty Club

October 14, 2010 (Thursday)

08:30-08:45	Opening remarks
Session 1: Review Chaired by Shaoping Zhu	
08:45-09:00	H. Takabe, CUP summary
09:00-09:30	Jiamin Yang, Experimental progress on laser-driven fusion and radiation-related studies in RCLF
09:30-10:00	K. A. Tanaka, Review of Relativistic Fast Electrons and Laser Light Relevant to Fast Ignition
10:00-10:30	C. T. Zhou, Recent status for high energy density plasma studies at IAPCM

Coffee break

Session 2: Laser astrophysics and acceleration Chaired by Hitoshi Sakagami	
11:00-11:30	H. Takabe, Grand Challenge Laser Astrophysics on Weibel Instability, meta- and micro-scale Magnetic Turbulence Resulting Nonlinear Structure Formation of High-Mach Collisionless Shock and Stochastic Cosmic Ray Accelaration
11:30-12:00	X. Q. Yan, Laser driven particle accelerator based on nanometer-scale targets
12:00-12:30	A. Sagisaka, Laser-driven proton generation with a thin-foil target

Lunch

Session 3: IFE simulation Chaired by Cangtao Zhou	
13:30-14:00	A. Sunahara, Numerical Simulation of Pre-formed Plasma Generated by Low Intensity Pre-Pulse Before Main Heating Laser in Fast-Ignition
14:00-14:30	Jinghong Li, Numerical Simulations of Inertial Confinement Fusion Hohlraum by Integrated-LARED Code
14:30-15:00	H. Sakagami, Collisional Effect on Fast Electron Generation and Transport in Fast Ignition

Coffee break

Session 4: Diagnostic Chaired by Yutong Li	
15:15-15:45	H. Habara, Angular resolved electron spectra relevant to core heating
15:45-16:15	Jian Zheng, Theoretical and experimental investigation of Thomson scattering from laser-produced plasmas

16:15-17:30	Discussion toward next CUP (K.A.Tanaka)

October 15, 2010 (Friday)

08:30-12:00	Oral session for Domestic HEDP Symposium

Lunch

13:30-17:30	Oral and poster sessions for Domestic HEDP Symposium

Banquet 18:30

October 16, 2010 (Saturday)

Session 5: LPI Chaired by Xueqin Yan	
09:00-09:30	Y. T. Li, Over μJ terahertz pulses from intense femtosecond laser-solid interactions
09:30-10:00	M. Hashida, Periodic grating structures self-formed on metal surfaces under femtosecond laser pulse irradiation
10:00-10:30	Baifei Shen, Single-cycle short-wavelength laser pulse twowards Schwinger Limit

Coffee break

Session 6: Application Chaired by Kazuo Tanaka	
10:45-11:15	H. Yoneda, Nonlinear optical phenomena in extreme ultra-violet region with high energy density conditions
11:15-11:45	Xiuguang Huang, Experimental study and application of laser-driven shock waves at SILP
11:45-12:15	N. Ohnishi, Computational Study of Shock Instability and Its Application

Lunch

13:30-17:00	Oral and poster session for Domestic HEDP Symposium

Program of the 2nd China National Symposium on High Energy Density Physics

Oct. 14-16, 2010, Shanghai Jiao Tong University, Xuhui Campus

October 13, 2010 (Wednesday)

13:00-18:00	Registration at Faculty Club of SJTU
18:00	Reception, Faculty Club

October 14, 2010 (Thursday)

9:00-17:00	Program of China-Japan CUP Seminar on Laser Plasma Physics

October 15, 2010 (Friday)

08:30-08:45	Opening remarks
HEDP Session 1: Laser Acceleration Chaired by Baohan Zhang	
08:45-09:15	谷渝秋，基于 SILEX-I 百太瓦飞秒激光的尾场电子加速研究进展 (invited)
09:15-09:45	Hongbin Zhuo, Quasimonoenergetic proton bunch generation by dual-peaked electrostatic-field acceleration in foils irradiated by intense linearly polarized lasers (invited)
09:45-10:00	Yanyun Ma, A new electron injection regime in laser wake field acceleration
10:00-10:15	Bin Liu, Ion jet generation in the ultra-intense laser interactions with rear-side concave target

Coffee break 10:15-10:30

HEDP Session 2: Laser driven X-ray sources Chaired by Jianmin Yuan	
10:30-11:00	陈黎明, 高对比度激光产生硬 X 射线研究 (invited)
11:00-11:15	Jiaqin Dong, 120ps, 4.75keV Ti Plasma X-ray Source and its application in HEDP experiments
11:15-11:30	Guang-yue Hu (胡广月), Multi-keV x-ray source generated by laser irradiated solid targets
11:30-11:45	王加祥, 自由电子在强激光场中的量子电动力学效应研究

11:45-12:00	Cao Lei-Feng (曹磊峰), Single order X-ray diffraction with photon sieves

Lunch 12:00-13:30

HEDP Session 3: Laboratory astrophysics and high energy density matters Chaired by Jie Liu	
13:30-14:00	Jianmin Yuan, The ordered structures from warm to hot dense matters: a description based on first principles molecular dynamics (invited)
14:00-14:30	J. Y. Zhong, Simulating magnetic reconnection phenomena in solar flares with intense lasers (invited)
14:30-14:45	董全力, 利用辐射流体力学程序与实验对比研究等离子体发射光谱
14:45-15:00	Wei Yu, 2D analytical model for the interaction of a short, intense laser pulse with solid target
15:00-15:15	L. F. Wang, Jetlike long spike in ablative Rayleigh-Taylor instability

Break and poster session 15:15-16:45

HEDP Session 4: Diagnostic of laser plasmas Chaired by Yuqiu Gu	
16:45-17:00	赵宗清, 超快微焦点 X 射线源照相实验研究
17:00-17:15	张红平, 准等熵压缩实验数据的反积分处理
17:15-17:30	单连强, 利用 X 射线背光照相提取锥壳靶预压缩面密度的时间演化
17:30-17:45	滕建, 时间分辨的啁啾质子照相
17:45-18:00	王首钧, 高能量激光产生的相向对流等离子体无碰撞冲击波的诊断

Banquet 18:30

October 16, 2010 (Saturday)

9:00-12:00	Program of China-Japan CUP Seminar on Laser Plasma Physics

HEDP Session 5: Fast Ignition and high energy density matters Chaired by Yanyun Ma	
14:00-14:30	A. L. Lei, Fast electron generation with micro-structured targets (invited)
14:30-15:00	Xiaonong Zhu, Characterization of Micro Air Plasma and Plume Dynamics Associated with Femtosecond Laser Ablation of Solid Targets (invited)
15:00-15:15	温贤伦, 不同极化态下超短超强激光产生超热电子发射研究
15:15-15:30	Lu Zhang, Study on optimal inertial-confinement-fusion hohlraum wall radial density and wall loss

Break and poster session 15:30-15:45

HEDP Session 6: High energy density matters Chaired by Jian Zheng	
15:45-16:15	Di-Fa Ye, Strong-field double ionization at the transition to below the recollision threshold (invited)
16:15-16:30	Jiayu Dai, Unified first principles description from warm dense matter to ideal ionized gas plasma: electron-ion collisions induced friction
16:30-16:45	辛建婷, 飞秒激光在铝膜中驱动冲击波的特性
16:45-17:00	Mu Li, Numerical Analysis of Laser-driven Reservoir Dynamics for Shockless Loading

Poster presentations

序号	作者	题目
1	L. G. Huang	Laser acceleration of quasi-monoenergetic protons from shaped targets irradiated by circularly polarized intense laser pulses
2	Lei Zhang	Astrophysics relevant dielectronic recombination process in laser-produced plasmas
3	J. Y. Mao	A transmission curved crystal spectrometer for high resolution hard x-ray spectroscopy
4	张璐	高通量 Ar 的 Ka 射线产生及其单发成像
5	Zhang Xiaoding	The X-ray Thomson scattering experiment for warm C foam and the spectrum fitting
6	王晓方	用于激光尾波场加速的气体靶模拟研究
7	邓邦林	类锂铜等离子体光谱模拟
8	Lu-Le Yu	Generation of tens of GeV quasi-monoenergetic proton beams from a moving double layer formed by ultraintense lasers at intensity 10^{21}-10^{23} W/ cm^{-2}
9	A.K. Li	The discrepancy between classical and quantum treatment of harmonic generation by relativistic electrons in strong laser fields
10	Na Ren	Electron-Positron Pair creation in time-dependent external fields
11	M. Jiang	Boson localization in the pair creation process
12	Hongjie LIU	空心锥靶中超热电子的产生和输运
13	W. Su	Numerical simulations of particle scattering off of a supercritical potential barrier under quantum field theory
14	Chun Li	Observation of strong terahertz wave generation by laser interacting with solid targets
15	Ya Bai	Terahertz radiation by two color fields and terahertz-wave-plasma characterization
16	焦春晔	基于 SILEX 的质子束特性及质子照相实验初探
17	Liu Dong-Xiao	The Calibration of GafChromic RadioChromic film HD-810 for proton dosimetry
18	董克攻	充气型放电毛细管的密度测量及磁流体模拟
19	吴玉迟	ILEX-I 装置上充气型放电毛细管电子加速实验初探
20	朱斌	基于充气型毛细管的超短激光波导实验研究
21	高宇林	基于光子筛的软 X 光谱仪
22	谭放	全光汤姆逊散射 X 光源数值模拟
23	巫殷忠	单脉冲太赫兹波的频谱测量
24	臧华平	Design,fabrication,and test of the zigzag diffraction grating for soft X region
25	余金清	同极化条件下激光-等离子体相互作用研究
26	辛国国	Dependence of the correlated-momentum patterns in double ionization on the carrier-envelope phase and intensity of a few-cycle laser pulse

List of participants

Hideali	Takabe	Osaka University
Masaki	Hashida	Kyoto University
Atsushi	Sunahara	Institute of Laser Technology
Naofumi	Ohnishi	Tohoku University
Hitoshi	Sakagami	National Institute for Fusion Science
Kazuo A.	Tanaka	Osaka University
Hideaki	Habara	Osaka University
Hitoki	Yoneda	University of Electro Communications
Akito	Sagisaka	Advanced Photon Research Center, JAEA
Zhengming	Sheng	Shanghai Jiao Tong University
Jie	Chen	Shanghai Jiao Tong University
Jun	Zheng	Shanghai Jiao Tong University
Jianqiu	Xu	Shanghai Jiao Tong University
Liejia	Qian	Shanghai Jiao Tong University
Feng	He	Shanghai Jiao Tong University
Jiaming	Li	Shanghai Jiao Tong University
Xiang	Gao	Shanghai Jiao Tong University
Baifei	Shen	Shanghai Institute of Optics and Fine Mechanics, CAS
Bear	Ya	Shanghai Institute of Optics and Fine Mechanics, CAS
Anle	Lei	Shanghai Institute of Optics and Fine Mechanics, CAS
Lingen	Huang	Shanghai Institute of Optics and Fine Mechanics, CAS
Xueqing	Yan	Peking University
Bicheng	Liu	Peking University
Jian	Zheng	University of Science and Technology of China
Chen	Zhang	University of Science and Technology of China
Liang	Guo	University of Science and Technology of China
Xiaoding	Zhang	University of Science and Technology of China
Xiaofang	Wang	University of Science and Technology of China
Guangyue	Hu	University of Science and Technology of China
Chen	Zhang	University of Science and Technology of China
Liang	Guo	University of Science and Technology of China
Yutong	Li	Institute of Physics, Chinese Academy of Sciences
Liming	Chen	Institute of Physics, Chinese Academy of Sciences
Lei	Zhang	Institute of Physics, Chinese Academy of Sciences
Jingyi	Mao	Institute of Physics, Chinese Academy of Sciences

Lu	Zhang	Institute of Physics, Chinese Academy of Sciences
Miao	Jiang	Institute of Physics, Chinese Academy of Sciences
Lule	Yu	Institute of Physics, Chinese Academy of Sciences
Shoujun	Wang	Institute of Physics, Chinese Academy of Sciences
Quanli	Dong	Institute of Physics, Chinese Academy of Sciences
Xiuguang	Huang	Shanghai Institute of Laser Plasma
Jiaqin	Dong	Shanghai Institute of Laser Plasma
Jianmin	Yuan	National University of Defense Technology
Hongbin	Zhuo	National University of Defense Technology
Hou	Yong	National University of Defense Technology
Jiayu	Dai	National University of Defense Technology
Yanyun	Ma	National University of Defense Technology
Jiayong	Zhong	National Astronomical Observatories, CAS
Huigang	Wei	National Astronomical Observatories, CAS
Banglin	Deng	Institution of Atomic and Molecular Phys., Sichuan University
Jiaxiang	Wang	East China Normal University
Ren	Na	East China Normal University
Ankang	Li	East China Normal University
Yingjun	Li	China University of Mining and Technology
Lifeng	Wang	China University of Mining and Technology
Wei	Su	China University of Mining and Technology
Xiaonong	Zhu	Institute of Modern Optics, Nankai University
X.T.	He	Institute of Applied Physics and Computational Mathematics
Shaoping	Zhu	Institute of Applied Physics and Computational Mathematics
Qingxue	Fang	Institute of Applied Physics and Computational Mathematics
Jinghong	Li	Institute of Applied Physics and Computational Mathematics
C.T.	Zhou	Institute of Applied Physics and Computational Mathematics
Hong-bo	Cai	Institute of Applied Physics and Computational Mathematics
Difa	Ye	Institute of Applied Physics and Computational Mathematics
Bin	Liu	Institute of Applied Physics and Computational Mathematics
Jie	Liu	Institute of Applied Physics and Computational Mathematics
C.S.	Liu	University of Maryland
Suyun	Zhou	Soochow University
Jian	Wang	Nei Jiang Normal College
Da-Feng	Cai	Nei Jiang Normal College
Jiaming	Yang	Laser Fusion Research Center, CAEP
Yuqiu	Gu	Laser Fusion Research Center, CAEP

Baohan	Zhang	Laser Fusion Research Center, CAEP
Weimin	Zhou	Laser Fusion Research Center, CAEP
Zongqing	Zhao	Laser Fusion Research Center, CAEP
Wei	Hong	Laser Fusion Research Center, CAEP
Lu	Zhang	Laser Fusion Research Center, CAEP
Dongxiao	Liu	Laser Fusion Research Center, CAEP
Chunhua	Jiao	Laser Fusion Research Center, CAEP
Yuchi	Wu	Laser Fusion Research Center, CAEP
Hongjie	Liu	Laser Fusion Research Center, CAEP
Xianlun	Weng	Laser Fusion Research Center, CAEP
LeiFeng	Cao	Laser Fusion Research Center, CAEP
Jianting	Xin	Laser Fusion Research Center, CAEP
Lianqiang	Shan	Laser Fusion Research Center, CAEP
Huaping	Zang	Laser Fusion Research Center, CAEP
Fang	Tan	Laser Fusion Research Center, CAEP
Yulin	Gao	Laser Fusion Research Center, CAEP
Jian	Teng	Laser Fusion Research Center, CAEP
Bin	Zhu	Laser Fusion Research Center, CAEP
Kegong	Dong	Laser Fusion Research Center, CAEP
Tiezhen	Xu	Laser Fusion Research Center, CAEP